

A TRANSFORMERLESS HIGH STEP-UP DC-DC CONVERTER FOR DC
INTERCONNECTS

by

Theodore Soong

A thesis submitted in conformity with the requirements
for the degree of Master of Applied Science
Graduate Department of Electrical and Computer Engineering
University of Toronto

Copyright © 2012 by Theodore Soong

Abstract

A Transformerless High Step-Up DC-DC Converter for DC Interconnects

Theodore Soong

Master of Applied Science

Graduate Department of Electrical and Computer Engineering

University of Toronto

2012

The proliferation of distributed energy resources (DER)s has prompted interest in the expansion of DC power systems. The technological limitations that hinder the expansion of DC power systems are the absence of DC circuit breakers and high step-up/high step-down DC converters for interconnecting DC systems.

This thesis presents a transformerless high step-up DC-DC converter intended for use as an interconnect between DC systems. The converter is required to operate at medium to high voltage ($>1\text{kV}$) and provide high voltage gain (>5).

This work details the steady state operation and dynamic model of the proposed converter. The component ratings are identified and converter design limitations are investigated. A 100V:1kV/4kW prototype is produced to verify the analytic steady state model and measure efficiency. An experimental efficiency of 90% was achieved at a step-up ratio of 1:10, however efficiency at low power is limited due to the need to circulate power.

Acknowledgements

First, and foremost, I'd like to thank my family for their unconditional love and support in whatever path I choose. I would also like to thank my teacher, Khinbu, for all the wisdom he has imparted to me over our brief meetings.

I would like to express my gratitude to my supervisor, Professor Peter Lehn, for his guidance, patience, and insight, without which this thesis would not be possible. In addition, I would like to thank him for allowing me the opportunity to continue my studies. I would also like express my appreciation to Professor Aleksander Prodić for encouraging me to start this journey into graduate studies.

Furthermore, I would like to thank everyone in the lab group, especially Damien Frost, Gregor Simeonov, and John Zong, for their advice, and company.

Contents

1	Introduction and Background	1
1.1	Background	1
1.2	Literature Overview	2
1.3	Objective and Scope of Thesis	6
2	Transformerless High Step-Up DC-DC Converter	7
2.1	Converter Topology and Overview	7
2.2	Steady State Analysis	12
2.2.1	Assumptions	12
2.2.2	Initial Conditions	12
2.2.3	Steady State Operation of Proposed Converter	13
2.2.4	State Equation Verification	20
2.3	Deadtime Requirement and Soft Switching Characteristics	21
2.4	Energy Balance	22
2.4.1	Control Variable	22
2.4.2	Energy Balance Calculation	23
2.4.3	Verification of \bar{I}_{in}	24
2.5	Maximum Switching Frequency Limitation	25
3	Converter Dynamics and Control	28
3.1	Converter Dynamics	28

3.2 Current Compensator	36
4 Converter Design	42
4.1 Refinement in \bar{I}_{in}	42
4.1.1 Verification of the Refinement to \bar{I}_{in}	45
4.2 Switch Requirements and Ratings	47
4.2.1 Switch Currents	48
4.2.2 Switch Ratings	49
4.3 Passive Component Ratings	53
4.4 Theoretical Efficiency	55
4.5 Design Considerations and Component Sizing	57
5 Experimental Results	59
5.1 Experiment Setup	60
5.1.1 Prototype Parameters	61
5.2 Switching Scheme	61
5.3 Experiment Results	62
5.3.1 Waveform Verification	65
5.3.2 Efficiency	69
5.4 Summary and Comparison	75
5.4.1 Boost Comparison	75
5.4.2 Voltage-Based Resonant Converter Comparison	77
5.4.3 Limitations	79
6 Conclusion	81
6.1 Future Work	82
Appendices	84
A Compensator and Current Filter Design	84

B Magnetic Loss Measurement	86
C Rectifying Diode Loss	89
D Boost & Current-Based Resonant Converter Efficiency	91
D.1 Current-Based Resonant Converter	92
D.2 Boost Converter	93
E Current-Based Resonant Converter: Voltage Sharing	95

List of Tables

2.1	List of Initial Conditions for Each State	13
2.2	Simulated Converter Properties	20
2.3	Simulated Converter values for Initial Conditions and State Durations for a switching frequency of 2kHz	20
2.4	Simulated Converter Properties	24
2.5	Simulated Verification of \bar{I}_{in} with different values of L_{in} , and f_{sw}	25
2.6	Simulated Verification of f_{max}	27
3.1	Simulated Converter Properties	32
3.2	Converter Properties for Current Compensator Simulation	39
4.1	Simulated Converter Properties	46
4.2	Simulated Verification of the refined version of \bar{I}_{in} . Rated \bar{I}_{in} is 19.9A . .	47
4.3	Converter Properties used to verify current ratings	50
4.4	Verification of Switch Ratings	53
4.5	Verification of Passive Component Ratings	55
5.1	Experimental Specifications	60
5.2	Experimental Component Values	61
5.3	Switching Components used in Experiment	62
5.4	Comparison of measured and theoretical durations of each state.	66

5.5	Comparison of measured and theoretical initial conditions for $i_{Lv}(t)$ and $v_{Cv}(t)$	68
5.6	Converter operating point used to investigate efficiency.	71
5.7	Breakdown of Power for Operating Point indicated in Figure 5.15 for P_{in} of 2632.0 W.	74
5.8	Converter Specifications from [1]	77
5.9	Current-Based Resonant Converter Component Values and Operating Point for Comparison to [1]	77
B.1	Inductor Specifications	86
B.2	Temperature of various points on both inductors.	86
C.1	Converter operating point used to investigate efficiency.	90
D.1	Switching components used in comparison of Boost and Current-Based Resonant Converter.	91
D.2	Experimental Component Properties	92
D.3	Current-Based Resonant Converter Component Properties and Operating Point	92
D.4	Switching losses for switches used in comparison.	93
D.5	Boost Converter Component Properties and Operating Point	94
E.1	Components of the two module Current-Based Resonant Converter . . .	97

List of Figures

1.1	Converter presented in [2]	4
1.2	Converter presented in [1]	5
2.1	Proposed Transformerless High Step-Up DC-DC Converter	8
2.2	Converter presented in [1]	9
2.3	Two module version of the converter presented in [1]	10
2.4	Proposed Converter topology and important waveforms over a single period.	14
2.5	Current paths of State 1. Arrows on the branches indicate current direction.	15
2.6	The rectifying current, $i_{Direct}(t)$, and the currents that it is composed of $i_{Lv}(t)$ and \bar{I}_{in}	17
2.7	Current paths of State 2. The current direction during the state is indicated by the arrows. The current of L_v changes polarity during this state, thus a bidirectional arrow is used.	17
2.8	Current paths of State 3. The current direction during the state is indicated by the arrows.	18
2.9	Current paths of States 4. Arrows on the branches indicate current direction.	19
2.10	Soft switching instances are shown on the waveforms of $i_{Lv}(t)$, $v_{Cv}(t)$, and $i_{in}(t)$. Gating signals to S1 and S2 are also depicted with negative deadtime.	22
2.11	Waveforms of $i_{Lv}(t)$, $v_{Cv}(t)$, and $i_{in}(t)$ with ripple added to $i_{in}(t)$.	26

3.1	Step Response of $i_{in}(t)$ due to a step in switching frequency from 4kHz to 1kHz	33
3.2	Step Response of $v_{out}(t)$ due to a step in switching frequency from 4kHz to 1kHz	33
3.3	Step Response of $i_{in}(t)$ due to a step in $v_{in}(t)$ from 100V to 200V	34
3.4	Step Response of $v_{out}(t)$ due to a step in $v_{in}(t)$ from 100V to 200V	34
3.5	Step Response of $i_{in}(t)$ due to a step in switching frequency from 4kHz to 1kHz with L_{in} of 50mH	35
3.6	Step Response of $v_{out}(t)$ due to a step in switching frequency from 4kHz to 1kHz with L_{in} of 50mH	35
3.7	Complete Control Loop	38
3.8	Analytic Model	39
3.9	Simulation response comparing $i_{in}(t)$ of the Analytic model and PSCAD simulations when a step in reference input current from 10A to 50A is applied.	40
3.10	Simulation response comparing $i_{in}(t)$ of the Analytic model and PSCAD simulations when a step in input voltage from 100V to 110V is applied. .	40
3.11	Simulation response comparing $i_{in}(t)$ of the Analytic model and PSCAD simulations when a step in output voltage from 1kV to 1.1kV is applied. .	41
4.1	Waveforms of $i_{Lv}(t)$, $v_{Cv}(t)$, and $i_{in}(t)$ with ripple added to $i_{in}(t)$	43
4.2	Comparison of original and refined average input current to the simulated average input current.	46
4.3	Current paths of States 4. Arrows on the branches indicate current direction. .	47
4.4	Switch currents for S1 and D2.	48
4.5	Inductor Currents and Resonant Capacitor Voltage using parameters from Table 4.3	50

4.6	The rectifying current, $i_{Direct}(t)$, and the currents that it is composed of $i_{Lv}(t)$ and \bar{I}_{in}	52
4.7	Current waveforms for all passive components.	54
5.1	Experimental Lab Setup	59
5.2	Schematic for Experimental Setup	61
5.3	Waveforms of $i_{Lv}(t)$, $v_{Cv}(t)$, and $i_{in}(t)$ with Regular PWM Scheme. $v_{Cv}(t)$ is shown in Ch1. $i_{in}(t)$ is shown in Ch3. $i_{Lv}(t)$ is shown in Ch4.	63
5.4	Waveforms of $i_{Lv}(t)$, $v_{Cv}(t)$, and $i_{in}(t)$ with Alternate PWM Scheme. $v_{Cv}(t)$ is shown in Ch1. $i_{in}(t)$ is shown in Ch3. $i_{Lv}(t)$ is shown in Ch4.	63
5.5	Switch current waveform when oscillations occur.	64
5.6	Alternative Switching Waveform	64
5.7	Efficiency Curve comparing the two PWM Schemes while the converter is operating with a $V_{in}:V_{out}$ of 120V:1200V	65
5.8	Waveforms of $i_{Lv}(t)$, $v_{Cv}(t)$, and $i_{in}(t)$ shown over multiple switching periods. Ch1, Ch2, and Ch4 are $v_{Cv}(t)$, $i_{Lv}(t)$ and $i_{in}(t)$ respectively.	66
5.9	Waveforms of $i_{Lv}(t)$, $v_{Cv}(t)$, and $i_{in}(t)$ over a single switching period, but the second charging state, State 8, is omitted. Ch1, Ch2, and Ch3 are $v_{Cv}(t)$, $i_{Lv}(t)$ and $i_{in}(t)$ respectively.	67
5.10	Close up of States 1 to 3. Ch1(Bottom), Ch2(Middle), and Ch3(Top) are $v_{Cv}(t)$, $i_{Lv}(t)$ and $i_{in}(t)$ respectively.	67
5.11	Efficiency curves for step-up ratios of 5, 8.3 and 10 plotted against input current.	70
5.12	Efficiency curves for step-up ratios of 5, 8.3 and 10 plotted against output current.	70
5.13	Theoretical and Actual Efficiency Curves at a step-up ratio of 10:1.	72
5.14	These curves compare the two different efficiencies achieved with a C_v of 25nF and 100nF	73

5.15 Theoretical and Actual Efficiency Curves for $C_v = 100\text{nF}$ with a step-up ratio of 1:10.	73
5.16 Comparison of Theoretical Efficiency between Boost Converter and Current-Based Resonant Converter	76
5.17 Comparison of Theoretical Efficiency between Voltage-Based and Current-Based Resonant Converter	78
A.1 Bode Plot of Loop	85
B.1 The different temperature measurement locations for the inductors are indicated here.	87
C.1 Voltage across the rectifying diode with the assumed current in the diode.	90
E.1 Two module version of the Current-Based Resonant Converter	96
E.2 Voltage sharing between modules of Two Module Current-Based Resonant Converter with mismatch between L_v components.	97
E.3 Voltage sharing between modules of Two Module Current-Based Resonant Converter. The following non-idealities have been added: mismatch between L_v components, delay in gating signals, and parasitic capacitance.	98

List of Abbreviations

BTB	Back to Back
CCM	Continuous Conduction Mode
DCM	Discontinuous Conduction Mode
DER	Distributed Energy Resource
ESR	Equivalent Series Resistance
HVDC	High Voltage Direct Current
IGBT	Insulated Gate Bipolar Transistor
LVDC	Low Voltage Direct Current
MVDC	Medium Voltage Direct Current
PI	Proportional Integral Controller
PTP	Point to Point
PWM	Pulse Width Modulation
ZCS	Zero Current Switching
ZVS	Zero Voltage Switching

Notation

$x(t)$	time dependent quantity
\bar{X}	DC Component of $x(t)$
\hat{x}	Small signal quantity
$X(s)$	Continuous time transfer function
$\langle x(t) \rangle_{\tau_{sw}}$	Time-averaged value of $v(t)$ over a period τ_{sw}

Symbols

L_{in}	Input Inductor
L_v	Resonant Inductor
C_v	Resonant Capacitor
i_{in}	Input Current
\bar{I}_{in}	Average Input Current
$\Delta i_{in_{pk-pk}}$	Input Ripple Current from peak to peak
$\Delta i_{in_{avg-pk}}$	Input Ripple Current average to peak
i_{Lv}	Resonant Inductor Current
v_{Cv}	Resonant Capacitor Voltage
V_{out}	Output Voltage
V_{in}	Input Voltage
t_x	Time t_x
τ_x	Duration of State x
I_{Lt_x}	Resonant Inductor Current at time t_x
SX	Switch 'X' of the Converter
DX	Freewheeling Diode of Switch 'X' of the Converter
D_{rect}	Rectifying Diode
V_{Ftyp}	Typical Forward Voltage Drop of Switch
R_{sw}	Switch "ON" State Resistance
R_{Lin}	Parasitic Resistance of the Input Inductor
R_{Lv}	Parasitic Resistance of the Resonant Inductor
R_{Cesr}	Parasitic Resistance of the Resonant Capacitor
E_{out}	Energy delivered to the output over one switching period.
E_{in}	Input energy over one switching period.

t_{sw}	Switching Period
f_{sw}	Switching frequency of Converter
f_{res}	Resonant Frequency
f_{max}	Maximum Switching Frequency of Converter
I_{res}	Resonant Current as defined in Equation 4.2.2

Chapter 1

Introduction and Background

This chapter introduces the main topic of this work, a transformerless high step-up DC-DC converter for interconnecting DC systems. The focus of this work is to develop a converter adapted from [1]. The modification results in better utilization of IGBT technology while maintaining soft switching characteristics.

1.1 Background

Current DC networks are primarily two terminal High Voltage DC (HVDC) systems or distribution systems limited to specific applications like shipboard power systems [3], and telecommunications [4]. The two terminal HVDC systems are used for Point To Point (PTP), or Back To Back (BTB) applications. The former is used to transfer power over long distances, where HVDC lines will outperform AC transmission lines at distances above 450km [5]. The latter has both converter stations at the same location, and generally acts as an interconnect between two AC grids of different frequencies [5].

Motivation for expanding the use of DC power systems to DC distribution networks has recently been spurred by the increasing penetration of Distributed Energy Resources (DER)s such as photovoltaic (PV) arrays, fuel cells, wind turbines, and battery energy storage systems (BESS). Resources like PV arrays, and fuel cells are inherently DC, but

have a wide output voltage range. These could be connected to an AC grid with a single DC/AC converter, but it is common to have a DC/DC stage to provide a regulated voltage for a DC/AC stage to use in connecting to the grid. Connecting these resources directly to a DC grid would save an additional conversion stage [6], [7]. Application of DC networks is not only limited to DERs, both [6] and [7] envision an expansion of DC networks to Medium Voltage DC (MVDC) collector networks that interconnect LVDC networks and wind farms.

Development and expansion of DC networks have been hindered by DC circuit breakers limitations and a lack of efficient high gain high voltage DC-DC converters, as identified in [8], [9]. DC circuit breakers are used to protect a DC system from faults or unit failures, and the high gain DC-DC converters are used to interconnect DC networks of different voltages. The high gain converters would be used to either connect new resources to existing HVDC lines where the additional power from the resources would not require changes to the transmission line [10] or used in MV/HV DC systems to interconnect two DC grids as studied by [8], [9]. The absence of efficient high gain high voltage DC-DC converters is the focus of this work.

1.2 Literature Overview

High gain converters can be classified into four major groups defined by two characteristics. The first characteristic is contingent on whether the converter topology utilizes a transformer / coupled inductor. The second characteristic depends on the converter's ability to provide soft switching to its devices at turn "on" or turn "off".

Transformer and coupled inductor based converters can enable high conversion ratios with common topologies adapting boost converters. However, the leakage inductance of transformers often cause voltage spikes during switching events, which can become

more severe as the operating voltage rises. Many topologies exist to mitigate the effect of leakage inductance, and examples of these topologies are given in [11], [12], and [13]. All three topologies attempt to use the leakage inductance of the transformer. The topology presented in [11] uses the leakage inductance of a coupled inductor to control diode reverse recovery losses of the output diode. Reference [12] employs a transformer to combine a flyback and boost topology, and is able to mitigate leakage inductance by allowing the energy to be transferred to the output, and [13] mitigates leakage inductances of a transformer by using active voltage clamps.

In high power and high voltage applications, magnetics are typically the largest components. To reduce the size of the magnetics, the transformer is operated at medium frequencies (500Hz to 3kHz). However, for high voltage applications, insulation requirements hinder the size reduction of the magnetics [15]. Another issue is the parasitic inductance and capacitance of the transformer. Parasitic inductance increases with the number of windings, and the number of windings must increase with operating voltage to prevent saturation. In addition, high step-up applications may require high turn ratios between different legs of the transformer, thus contributing to the parasitic inductance, and results in larger voltage spikes. Parasitic capacitance can be a large source of loss in a transformer, and material selection can be difficult because good dielectric materials must be chosen to minimize losses in the parasitic capacitance [16]. While use of transformers can facilitate high conversion ratios, if galvanic isolation is not necessary then a transformerless converter should be considered to avoid the difficulties of high voltage transformers.

Soft switching topologies achieve zero voltage switching (ZVS) and/or zero current switching (ZCS) to reduce switching losses when compared to hard switched converters. Converters that achieve soft switching are important for high voltage applications because IGBTs have switching times that are several times longer than MOSFETs [17]. Thus, switching losses are the primary limitation to the switching frequency of the IGBT. Soft

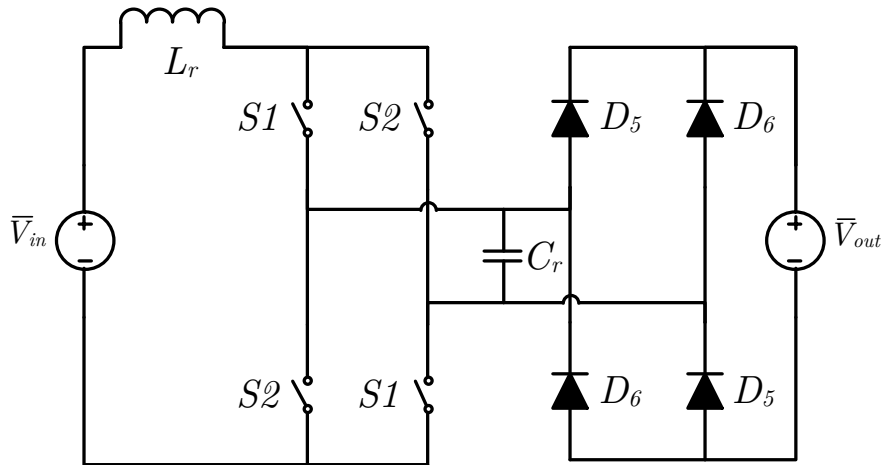


Figure 1.1: Converter presented in [2]

switching of diodes are also important because of reverse recovery losses and EMI issues that increase with operating voltage.

Soft switching topologies reduce switching losses with the use of L-C networks in exchange for larger conduction losses due to higher peak currents. Examples of transformerless soft switching topologies are [2] and [1]. These two topologies are shown in Figure 1.1 and 1.2 respectively.

Reference [2] presents a high voltage step-up converter that uses a resonant capacitor connected to an H-bridge and a rectifier. The resonant capacitor stores energy from cycle to cycle to aid in the step-up process, and operates by “rotating” the resonant capacitor’s polarity with the H-bridge to incite current flow in the resonant inductor. The converter presented in [1] operates with a similar method, but is able to achieve a modular structure. Modularity in high voltage converters is important because the voltage rating of switches is extended by placing devices in series. During operation, voltage balance between the series devices must be maintained by using passive snubbers, voltage clamps, or active gate control, which all result in loss [18]. The topology of [1] is able to increase voltage blocking capabilities by using additional modules and was able to show voltage balance during a switching period.

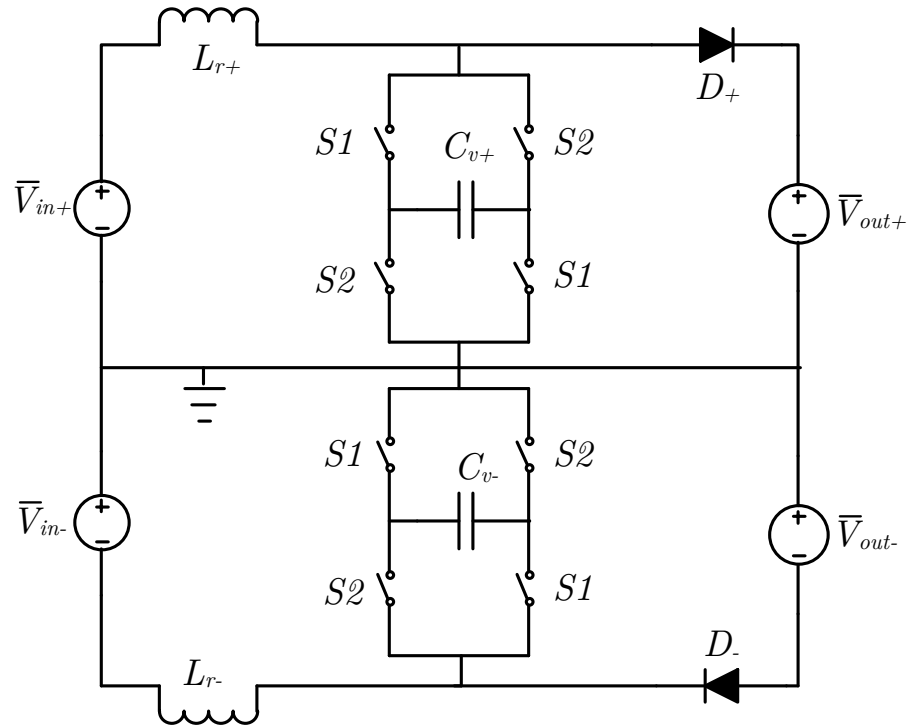


Figure 1.2: Converter presented in [1]

Through resonance, both [2] and [1] are both transformerless and provide soft switching opportunities for their switches. However, they utilize thyristor technology, which is able to provide low conduction losses, but limits the maximum frequency of operation due to the thyristor turn “off” time. This results in increased component size and cost. Two other main types of active switches are MOSFETs, and IGBTs, and both are able to switch at higher frequencies in comparison to thyristors. MOSFETs can be switched at the highest frequency and have lower switching losses compared to IGBTs, but their voltage blocking and current carrying capabilities are comparatively low to thyristors and IGBTs. In addition, to create an equivalent IGBT from MOSFETs would require the MOSFETs to be placed in series and parallel. Snubbers would be required to ensure voltage balance across the series connected MOSFETs, which increases complexity, cost, and reduces reliability. Thus, IGBTs are preferred because they have a higher maximum switching frequency compared to thyristors, reducing resonant component size, and they

have higher voltage and current ratings in comparison to MOSFETs. For high voltage and high power applications, the converter topology should be transformerless and soft-switching while utilizing the V-I characteristics of IGBTs.

1.3 Objective and Scope of Thesis

The purpose of this thesis is to develop a transformerless high step-up DC-DC converter to facilitate interconnection between DC networks. The converter is required to provide high gain, and operate at medium to high voltage ($>1\text{kV}$). High gain is defined as gains greater than that of a typical boost converter (>5). Galvanic isolation and bidirectional power transfer is not posed as a requirement since it is not required of all applications [9].

This work studies a single module converter derived from the converter presented in [1], and completes the following objectives:

1. Derive the proposed converter from the converter presented in [1] to exploit V-I characteristics of IGBT devices.
2. Develop steady state relations and verify by experiment.
3. Produce dynamic model and current controller and verify with PSCAD / EMTDC.
4. Identify component ratings and converter limitations.
5. Measure and scrutinize experimental converter efficiency.

Chapter 2

Transformerless High Step-Up DC-DC Converter

This chapter introduces the proposed converter, and is separated into four sections. The first section outlines the relation between the family of converters presented by [1] and the proposed converter. The second section develops steady state equations for the proposed converter. The third section applies energy balance to develop the power equation of the converter, and the final section highlights the frequency limitation of the proposed converter.

2.1 Converter Topology and Overview

The converter studied in this work utilizes a resonant capacitor and inductor, C_v and L_v , to achieve high step-up operation, and is shown in Figure 2.1. This topology is a modification of the step-up converter presented in [1], which was chosen for its modular structure. The switch type used in [1] is limited to thyristors or IGBTs with a series diode. As mentioned in Section 1.2, use of IGBT technology is preferred to allow for higher frequency operation with smaller components, and the modification made to [1] presented in this work would allow for the use of IGBTs without a series diode.

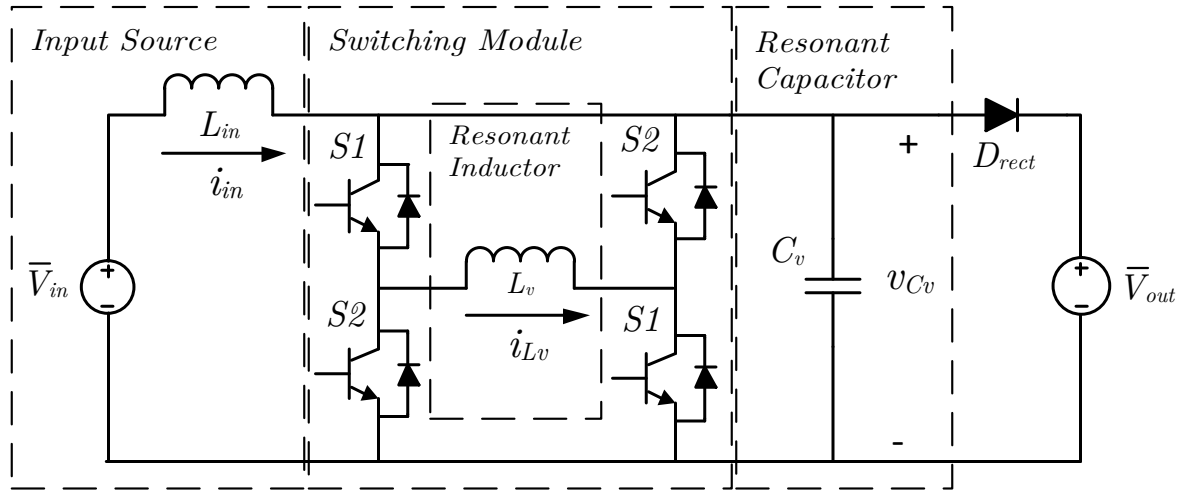


Figure 2.1: Proposed Transformerless High Step-Up DC-DC Converter

For comparison purposes, a single module step-up version of [1] is shown in Figure 2.2. For the remainder of this work, the converter in Figure 2.2 will be referred to as the voltage-based resonant converter, and the proposed converter will be referred to as the current-based resonant converter. The two active switches labelled S1 in Figure 2.1 are referred to as a single switch S1 because they operate in unison. The active switches labelled S2 in the same figure are referred to as the switch S2. A similar nomenclature is applied Figure 2.2 to the switches labelled SA and SB. The term resonant network is used to refer to the combination of the switching module and resonant capacitor of Figure 2.1.

The voltage-based resonant converter, shown in Figure 2.2, utilizes a switching module that consist of an H-bridge with a capacitor between the two half bridges. Switch SA or SB can be turned “on” to “rotate” the capacitor’s polarity. The operation of this converter is limited to discontinuous conduction mode (DCM) to accomplish ZCS turn “off” of diode D1 and ZCS turn “on” for switches SA and SB. The turn “off” transition of SA and SB is classified as ZVS for this topology .

The theory of operation for the voltage-based resonant converter is to use the switching module to aid in the turn “on” and “off” of the rectifying diode. At the end of

the each period, in steady state, the resonant capacitor , C_{res} , sustains a voltage equal to the negative of the output voltage, $-\bar{V}_{out}$. No current conducts through the resonant inductor, L_{res} , and all switches are disabled. Assuming the switch SB was used in the previous cycle, SA is activated to initiate the next period.

The switch type used in the voltage-based resonant converter requires unidirectional current conduction, and bidirectional voltage blocking. This limits switching technology to thyristors or IGBTs with series diodes. If thyristors are utilized, a minimum turn “off” time is required. This limits the minimum size of the resonant components. Smaller component sizes can be realized by using IGBTs with a series diode, but this results in twice the conduction losses.

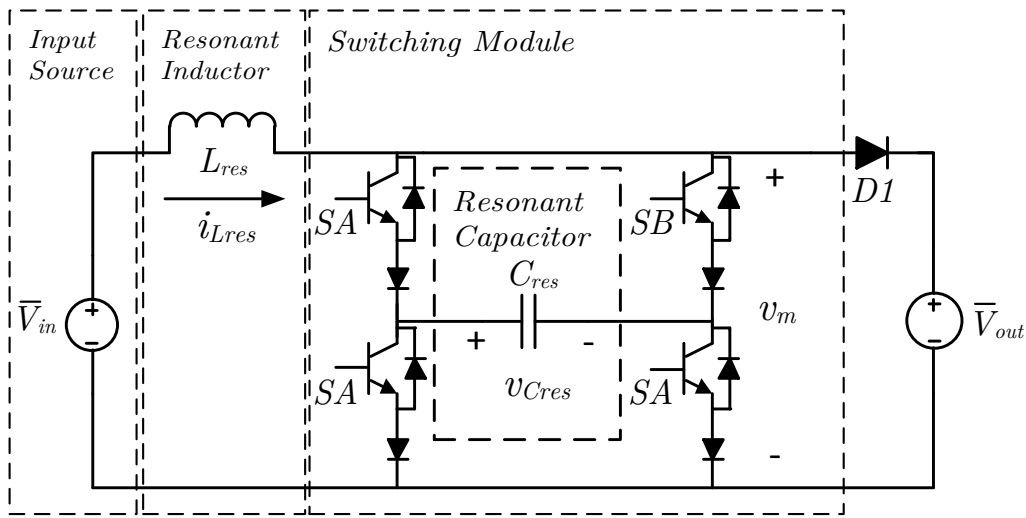


Figure 2.2: Converter presented in [1]

When SA is turned “on” at the beginning of the period, the capacitor is “rotated”, and the voltage across the switching module, $v_m(t)$, is equal to $-\bar{V}_{out}$. At the same time, positive voltage is applied to the resonant inductor and causes it to charge the resonant capacitor from $-\bar{V}_{out}$ to \bar{V}_{out} . When the resonant capacitor reaches \bar{V}_{out} , the rectifying diode, D1, becomes forward biased after which the current of the resonant inductor, I_{Lres} is transferred to the output. This ceases when the resonant inductor no longer contains any energy, and SA is subsequently turned “off”. This completes the first half

of a switching period for the voltage-based resonant converter. The second half of the period is identical, except the capacitor's voltage is \bar{V}_{out} instead of $-\bar{V}_{out}$, and switch SB is used instead of SA .

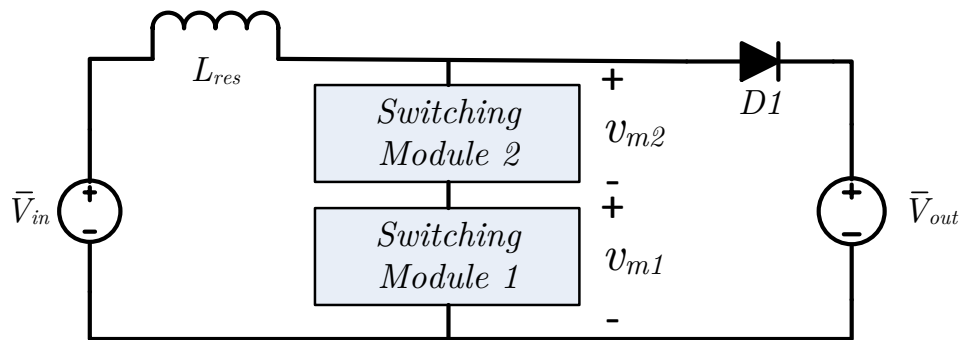


Figure 2.3: Two module version of the converter presented in [1]

The voltage-based resonant converter is able to extend its output voltage by adding additional switching modules in series with the first, a two module version is depicted in Figure 2.3. Reference [1] experimentally showed voltage sharing during a switching period, but the switch voltage stresses may be larger than expected during the time period where the switching devices are turning “on”. This can be illustrated with Figure 2.3. Before the period begins, all switches are off, and L_{res} is not conducting current. At the beginning of the period, identical gate signals are sent to both switching modules. If there is a delay in gate signals between the two modules then one module would turn “on” before the other. If switching module 1 begins “rotating” before module 2 then the voltage rating across module 2 is momentarily $\bar{V}_{in} + \bar{V}_{out}$. In this case, the module may have enough voltage blocking capabilities, but placing additional modules in series would exacerbate the situation, and the voltage rating of switches would be exceeded.

Transforming the voltage-based resonant converter to the current-based resonant converter results in Figure 2.1. By comparing Figure 2.1 and Figure 2.2, each equivalent

component can be seen. The input source becomes a current source that is realized by a large input inductor, L_{in} , in series with the input voltage source. The switching module “rotates” the resonant inductor, L_v , instead of the resonant capacitor, C_{res} , and effectively changes the current direction of the switching module instead of its voltage polarity. The resonant inductor, L_{res} , of Figure 2.2 is replaced with the resonant capacitor, C_v .

The theory of operation for the current-based resonant converter is similar to the voltage-based resonant topology. The switching modules of both converters are meant to control the turn “on” and “off” process of the rectifying diode. At the end of each period the resonant inductor current, $i_{Lv}(t)$ is non-zero. The resonant capacitor voltage, $v_{Cv}(t)$, is at 0V, and Switch S2 is “on”. The start of each period begins when S1 turns “on” and S2 turns “off”.

$i_{Lv}(t)$ will “reverse” direction, and charge the resonant capacitor, C_v , in conjunction with the input current, $i_{in}(t)$. When the resonant capacitor voltage reaches the output voltage, \bar{V}_{out} , the rectifying diode D_{rect} is enabled, and both $i_{in}(t)$ and $i_{Lv}(t)$ are transferred to the output. The process that determines the end of the rectifying stage. Eventually, energy is no longer delivered to the output, and the resonant inductor, L_v , discharges C_v to 0V. This ends the first half of the switching period. The second half of the period is identical except that switch S1 is used and the resonant inductor’s polarity is changed.

As a parallel to the voltage-based resonant converter, the current-based resonant converter operates in continuous conduction mode (CCM), and utilize IGBTs. Instead of storing energy in the resonant capacitor the current-based resonant converter stores the energy from period to period in the resonant inductor.

2.2 Steady State Analysis

The results of the steady state analysis are presented in this section. However, assumptions and unknowns are outlined before detailing the operation of the converter.

2.2.1 Assumptions

Several assumptions are made to simplify steady state analysis of this proposed converter.

The assumptions are:

1. All components are ideal.
2. All sources are constant over a period.
3. The ratio between the input inductor, L_{in} , and resonant inductor, L_v , should be much greater than 1, $\frac{L_{in}}{L_v} \gg 1$, such that the input inductor can be assumed to be a constant current source.

The first and second assumptions are standard assumptions for preliminary converter analysis. The third assumption ensures that L_{in} is sufficiently large to be approximated as a current source. A $\frac{L_{in}}{L_v}$ ratio of 10 is sufficient to maintain the third assumption.

2.2.2 Initial Conditions

Due to the third assumption, input current, $i_{in}(t)$, is assumed to be a constant value denoted as, \bar{I}_{in} . This reduces the number of state variables to the resonant inductor current, $i_{Lv}(t)$, and resonant capacitor voltage, $v_{Cv}(t)$. The waveforms for these two passive components of the converter are shown in Figure 2.4. From Figure 2.4, it should be noted that analysis is only required for States 1 to 4 of the converter, because States 5 to 8 are identical except that the direction of $i_{Lv}(t)$ is inverted.

For each state of the converter, some of the initial conditions for the resonant inductor, L_v and resonant capacitor, C_v can be inferred from Figure 2.4. $i_{Lv}(t)$ is equal to \bar{I}_{in} at

State	Initial Condition	
	V_{Cv}	I_{Lv}
1	0	Unknown
2	\bar{V}_{out}	Unknown
3	\bar{V}_{out}	\bar{I}_{in}
4	0	Unknown

Table 2.1: List of Initial Conditions for Each State

the beginning of State 3, and the initial conditions of $v_{Cv}(t)$ for all states is either the output voltage, \bar{V}_{out} , or 0V. Table 2.1 lists the initial conditions and their values based on Figure 2.4.

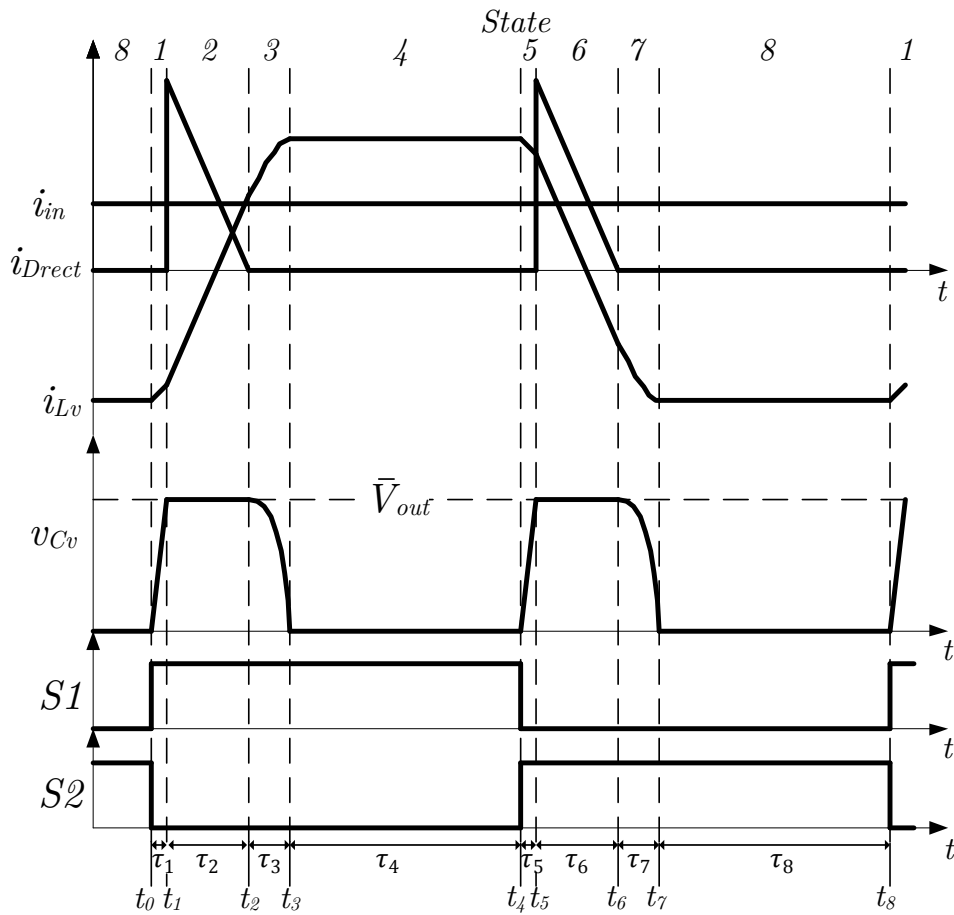
2.2.3 Steady State Operation of Proposed Converter

With the assumptions and initial conditions identified, the operation of the converter in steady state can be discussed. A single switching period for the current-based resonant converter can be divided into eight distinct states of the converter. Figure 2.4 shows the ideal waveforms of the resonant network, and indicates each state of the switching period. The duration of the states are also labelled on the waveforms and are denoted by τ_1 to τ_8 for State 1 to State 8 respectively.

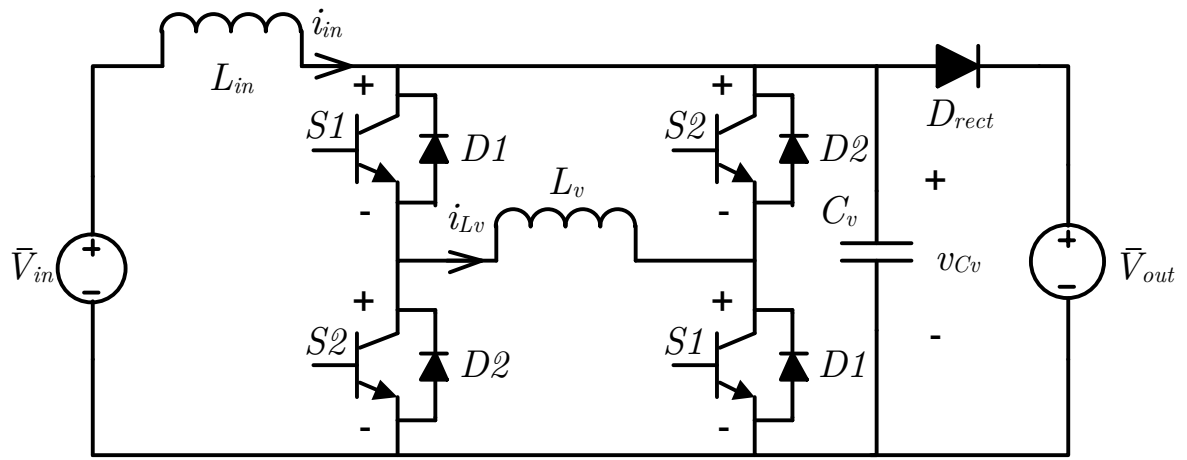
State 1 [t_0, t_1]

A switching period for the converter begins with State 1, and the associated current paths are shown in Figure 2.5. The previous switching period ended with a non-zero value for $i_{Lv}(t)$, switch S2 turned “on”, and $v_{Cv}(t)$ equal to 0V. At the beginning of State 1, switch S2 is turned “off” and S1 is turned “on”. $i_{Lv}(t)$ is now redirected into C_v , and both \bar{I}_{in} and $i_{Lv}(t)$ charge C_v from 0V to \bar{V}_{out} . When $v_{Cv}(t)$ reaches \bar{V}_{out} , State 1 transitions to State 2.

The $v_{Cv}(t)$ rises according to the resonant frequency, ω_{res} , of the resonant components.



(a) Waveforms of $i_{Lv}(t)$, $i_{Direct}(t)$, $v_{Cv}(t)$, and \bar{I}_{in} . Switching signals and converter states are also shown.



(b) Transformerless High Step-Up DC-DC Converter

Figure 2.4: Proposed Converter topology and important waveforms over a single period.

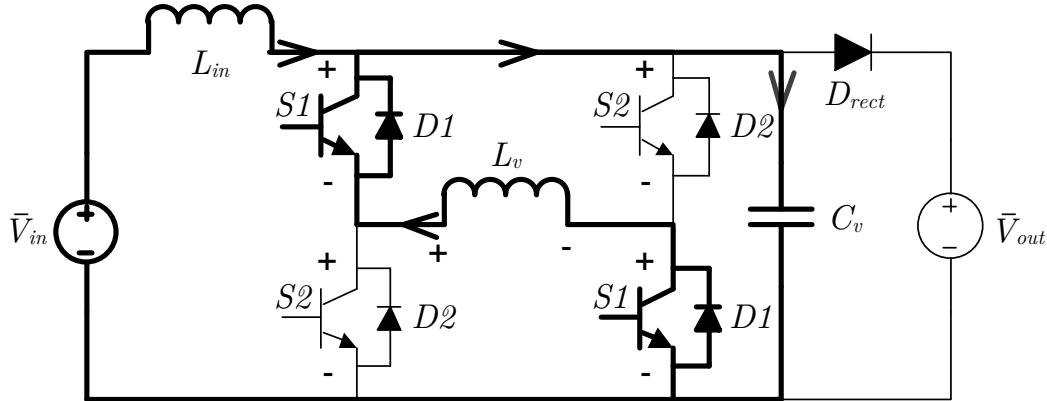


Figure 2.5: Current paths of State 1. Arrows on the branches indicate current direction.

Equations (2.2.1) and (2.2.2) describe $v_{Cv}(t)$ and $i_{Lv}(t)$ respectively, during this state.

$$v_{Cv}(t) = (\bar{I}_{in} - I_{Lt_0}) \sqrt{\frac{L_v}{C_v}} \sin(\omega_{res}(t - t_0)) \quad (2.2.1)$$

$$i_{Lv}(t) = \bar{I}_{in} - (\bar{I}_{in} - I_{Lt_0}) \cos(\omega_{res}(t - t_0)) \quad (2.2.2)$$

where ω_{res} is the resonant frequency and I_{Lt_0} is the initial condition of L_v for State 1.

These quantities are defined as

$$\omega_{res} = \frac{1}{\sqrt{L_v C_v}} \quad (2.2.3)$$

$$I_{Lt_0} = - \left(\bar{I}_{in} + \sqrt{\frac{C_v}{L_v}} \bar{V}_{out} \right) \quad (2.2.4)$$

Based on initial and final conditions of $v_{Cv}(t)$ for State 1, the duration of the state, τ_1 , can be determined.

$$\tau_1 = t_1 - t_0 \quad (2.2.5)$$

$$= \frac{1}{\omega_{res}} \sin^{-1} \left(\frac{\bar{V}_{out} \sqrt{\frac{C_v}{L_v}}}{2\bar{I}_{in} + \bar{V}_{out} \sqrt{\frac{C_v}{L_v}}} \right) \quad (2.2.6)$$

State 2 [$t_1, t_2]$

State 2 begins when $v_{Cv}(t)$ reaches \bar{V}_{out} , and the rectifying diode, D_{rect} , is forward biased. Both \bar{I}_{in} and $i_{Lv}(t)$ then conduct through the rectifying diode to the output. The resulting current directions for State 2 are depicted in Figure 2.7. For the duration of this state, \bar{V}_{out} is applied across the resonant inductor, L_v . Thus, $i_{Lv}(t)$ is changing at a constant rate. Figure 2.6 shows how the diode current is comprised of $i_{Lv}(t)$ and \bar{I}_{in} . As $i_{Lv}(t)$ changes, it passes the zero crossing and starts to divert \bar{I}_{in} from the rectifying diode. When $i_{Lv}(t)$ equates to the input current, power is no longer delivered to the output, and the rectifying diode subsequently turns “off”, thus ending State 2.

The time domain equations for $i_{Lv}(t)$ and $v_{Cv}(t)$ during this state are:

$$v_{Cv}(t) = \bar{V}_{out} \quad (2.2.7)$$

$$i_{Lv}(t) = \frac{\bar{V}_{out}}{L_v}(t - t_1) + I_{Lt_1} \quad (2.2.8)$$

where I_{Lt_1} is the resonant inductor’s current at the beginning of State 2.

$$I_{Lt_1} = \bar{I}_{in} - \sqrt{4(\bar{I}_{in}^2 + \bar{I}_{in}\sqrt{\frac{C_v}{L_v}\bar{V}_{out}})} \quad (2.2.9)$$

The output pulse length, τ_2 , can be determined with the initial and end conditions of $i_{Lv}(t)$ for State 2, and results in Equation (2.2.11).

$$\tau_2 = t_2 - t_1 \quad (2.2.10)$$

$$= \frac{2L_v}{\bar{V}_{out}} \sqrt{\bar{I}_{in}^2 + \bar{I}_{in}\sqrt{\frac{C_v}{L_v}\bar{V}_{out}}} \quad (2.2.11)$$

State 3 [$t_2, t_3]$

As previously mentioned, the rectifying diode is no longer conducting at the beginning of State 3, but C_v is still charged at \bar{V}_{out} . This applies a voltage across L_v causing its current

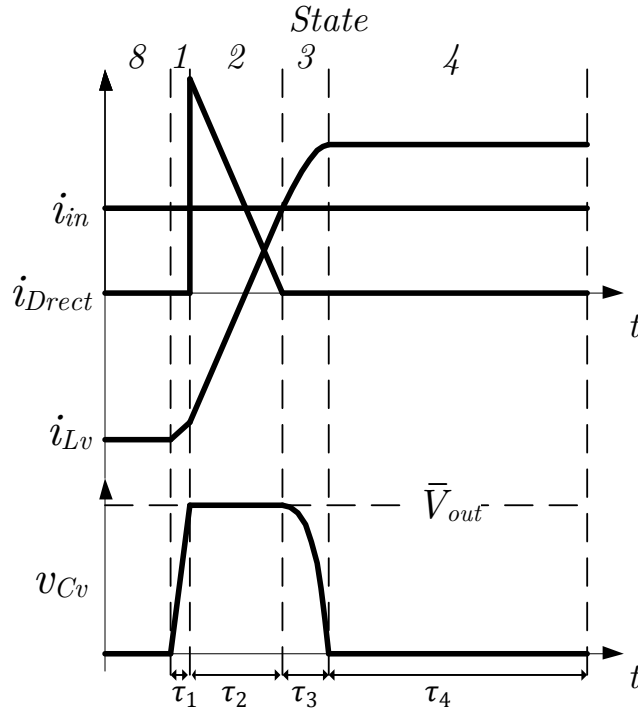


Figure 2.6: The rectifying current, $i_{Drect}(t)$, and the currents that it is composed of $i_{Lv}(t)$ and \bar{i}_{in}

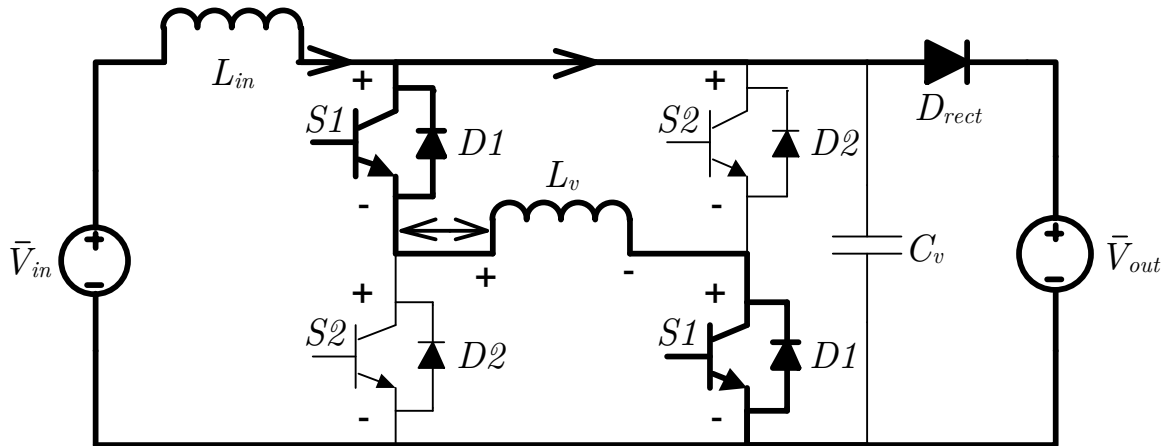


Figure 2.7: Current paths of State 2. The current direction during the state is indicated by the arrows. The current of L_v changes polarity during this state, thus a bidirectional arrow is used.

to increase while discharging C_v . When C_v reaches 0V, voltage is no longer applied to L_v , and $i_{Lv}(t)$ stays constant. When $v_{Cv}(t)$ reaches 0V, it signifies the beginning of State

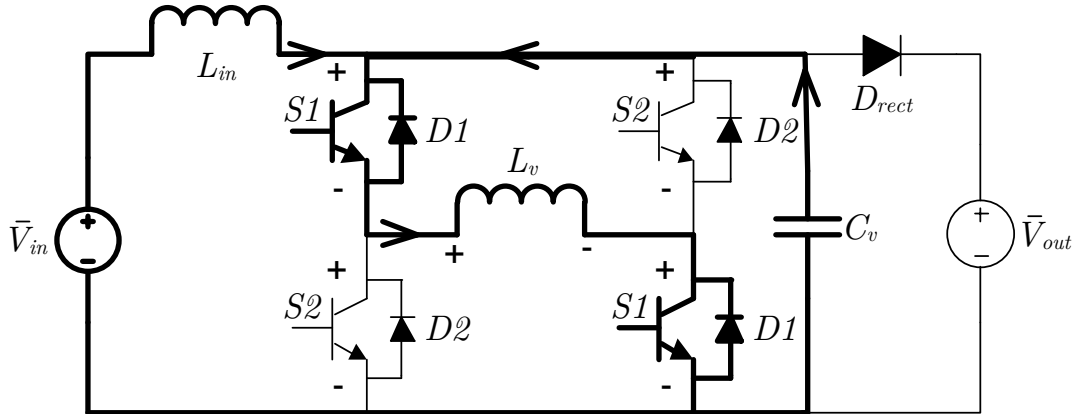


Figure 2.8: Current paths of State 3. The current direction during the state is indicated by the arrows.

4. The schematic for State 3 is identical to State 1, except that the current direction of the resonant components is reversed as shown in Figure 2.8.

The resulting equations for $i_{Lv}(t)$ and $v_{Cv}(t)$ for the duration of this state are:

$$v_{Cv}(t) = \bar{V}_{out} \cos(\omega_{res}(t - t_2)) \quad (2.2.12)$$

$$i_{Lv}(t) = \bar{I}_{in} + \sqrt{\frac{C}{L_v}} \bar{V}_{out} \sin(\omega_{res}(t - t_2)) \quad (2.2.13)$$

As discussed in Section 2.2.2, the initial condition for the resonant inductor for State 3, I_{Lt_2} , is equal to \bar{I}_{in} , and has been incorporated into Equation (2.2.12) and (2.2.13).

The duration of State 3 can be found by using the initial and final condition of $v_{Cv}(t)$ for this state, and results in:

$$\tau_3 = t_3 - t_2 \quad (2.2.14)$$

$$= \frac{\pi}{2} \frac{1}{\omega_{res}} \quad (2.2.15)$$

State 4 [t_3, t_4]

State 4 begins when $v_{Cv}(t)$ reaches 0V. Since, no voltage is applied across L_v , $v_{Cv}(t)$ remains at 0V, and $i_{Lv}(t)$ remains constant during this state. This state can be viewed

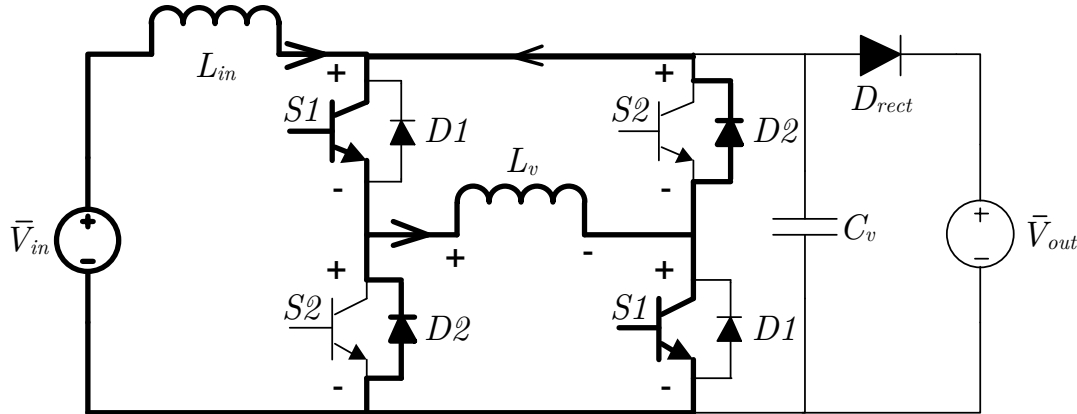


Figure 2.9: Current paths of States 4. Arrows on the branches indicate current direction.

as a hold state because the state of the resonant components are unchanging. Figure 2.9 depicts the current flow in the circuit during State 4. $i_{Lv}(t)$ is shown to flow through all switches, and the reason is discussed later in Section 4.2.1. Therefore, the state equations are

$$v_{Cv}(t) = 0 \quad (2.2.16)$$

$$i_{Lv}(t) = I_{Lt_3} \quad (2.2.17)$$

for the duration of this state. I_{Lt_3} is the initial condition of the resonant inductor current defined in Equation (2.2.18).

$$I_{Lt_3} = \bar{I}_{in} + \sqrt{\frac{C_v}{L_v}} \bar{V}_{out} \quad (2.2.18)$$

The duration of State 4, τ_4 , is left as a variable used to control the power delivered to the output.

State 5 to State 8

State 5 begins by turning switches S1 “off”, and S2 “on”. This starts the process of charging C_v with \bar{I}_{in} and $i_{Lv}(t)$. States 5 to 8 maintain the same order of events as State

1 to 4, but $i_{Lv}(t)$ conducts through the opposite half of the H-bridge. This causes $i_{Lv}(t)$ to be inverted, as shown in Figure 2.4.

2.2.4 State Equation Verification

State equations were verified with simulation in PSCAD/EMTDC. In this simulation, an ideal current source was used, and the system parameters that were used are shown in Table 2.2.

Converter Property	Value
L_v	500 μH
C_v	0.025 μF
f_{sw}	2kHz
V_{out}	1kV
\bar{I}_{in}	50A

Table 2.2: Simulated Converter Properties

The analytic expressions were verified by comparing the simulated and calculated values for the initial conditions and durations of the States 1 to 4. The simulated and calculated values are presented in Table 2.2. With a simulation time step of $0.01\mu\text{s}$, the analytic equations all match simulation.

Unknown	Simulated	Calculated
τ_1	$2.41\mu\text{s}$	$2.34\mu\text{s}$
τ_2	$53.40\mu\text{s}$	$53.42\mu\text{s}$
τ_3	$5.46\mu\text{s}$	$5.55\mu\text{s}$
τ_4	$189.75\mu\text{s}$	$188.69 \mu\text{s}$
I_{Lt_0}	-57.06A	-57.07A
I_{Lt_1}	-56.82A	-56.84A
I_{Lt_2}	49.98A	50.00A
I_{Lt_3}	57.07A	57.07A

Table 2.3: Simulated Converter values for Initial Conditions and State Durations for a switching frequency of 2kHz

2.3 Deadtime Requirement and Soft Switching Characteristics

In the presented analysis, the converter operates the switch S1 with a 50% duty cycle, and the inverted signal is applied to S2. This allows the switches to maintain a current path for the resonant inductor current, $i_{Lv}(t)$, during the switching period. To ensure a current path for $i_{Lv}(t)$ during the switch transitions from S1 to S2 or S2 to S1, a negative deadtime is required. A short circuit is avoided because switch transitions occur while 0V is applied across the switches as can be seen in Figure 2.10.

With the negative deadtime, the proposed converter is capable of providing soft switching opportunities to its switching devices, as identified in Figure 2.10. The active switches, S1 and S2, achieve ZVS at their turn “on” and turn “off”. Using S1 as an example, during State 8, the resonant capacitor voltage, $v_{Cv}(t)$, is 0V, and ZVS turn “on” is guaranteed by the negative deadtime. At the end of State 4, S1 is turned “off” while $v_{Cv}(t)$ is still 0V; this achieves ZVS.

For the rectifying diode, D_{rect} , it has a ZVS turn “off”, but the turn “on” process is a hard turn “on”. Turn “off” for the rectifying diode occurs at the end of State 2 when $i_{Lv}(t)$ has diverted the average input current, \bar{I}_{in} , from the rectifying diode and current is no longer transferred to the output. During State 3, the resonant inductor, L_v , discharges the resonant capacitor, C_v , causing $i_{Lv}(t)$ to increase and $v_{Cv}(t)$ to decrease to 0V. The rectifying diode is gradually reverse biased during the transition from State 2 to State 3, and ZVS is achieved because L_v provides a current path to extract the reverse recovery charge, Q_{rr} , from the rectifying diode before discharging C_v during State 3.

The rectifying diode is turned “on” at the end of State 1 and beginning of State 2, and is required to conduct $i_{Lv}(t)$ and \bar{I}_{in} at turn “on”. The forward recovery of the diode causes $i_{Lv}(t)$ and \bar{I}_{in} to continue charging C_v , thus causing overshoot and turn “on” losses. The overshoot can be minimized with a larger C_v .

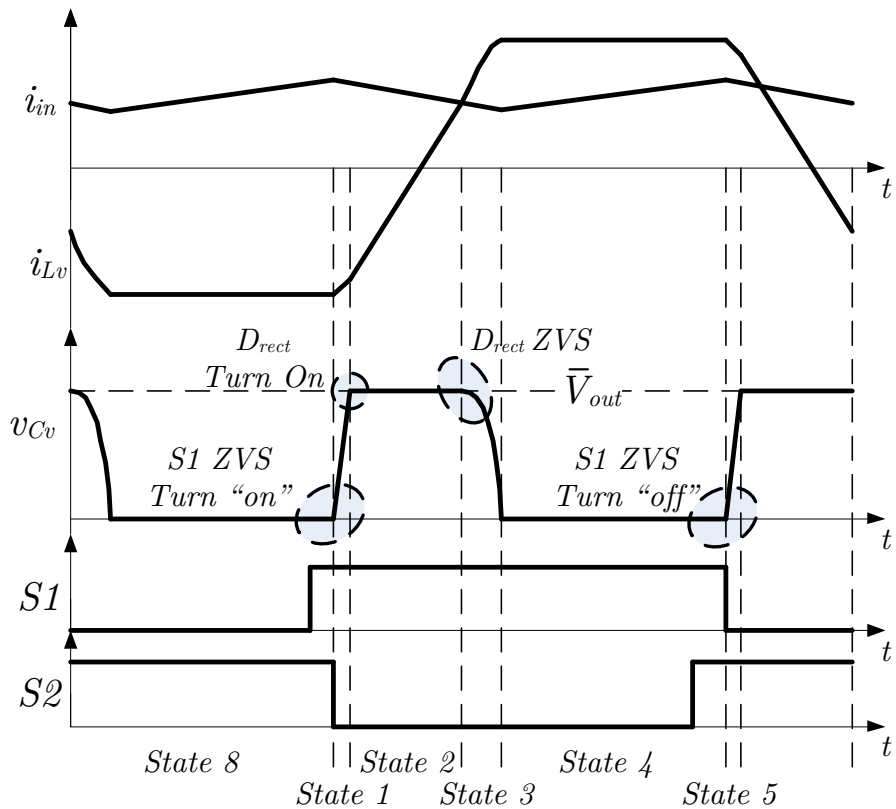


Figure 2.10: Soft switching instances are shown on the waveforms of $i_{Lv}(t)$, $v_{Cv}(t)$, and $i_{in}(t)$. Gating signals to S1 and S2 are also depicted with negative deadtime.

2.4 Energy Balance

Using the state equations, energy balance can be applied across the input inductor to relate the output power to the control variable, the switching frequency. Energy balance results in a solution for the average input current given that the application will specify the input and output voltage.

2.4.1 Control Variable

As previously mentioned, the switching frequency, f_{sw} , is used as a control variable to control power delivery to the output. In most converters, increasing this hold state implies that power delivered to the output is less frequent. However, this converter's hold states,

State 4 and State 8, are used to maintain the volt-sec balance for the input inductor, L_{in} . A lower f_{sw} implies a longer State 4 and State 8, which increases the average input current, \bar{I}_{in} , and an increase in the power delivered during the next period. By varying f_{sw} , the volt-second balance can be adjusted to attain a specific \bar{I}_{in} . Therefore, this state should be referred to as the input inductor charging state instead of a holding state, and the remainder of this thesis refers to State 4 and 8 as the input inductor charging states.

2.4.2 Energy Balance Calculation

To relate the output power to the control variable, the energy delivered to the output per period, E_{out} is derived and equated to the input energy per period, E_{in} . First solving for E_{out} , the only states that deliver energy to the output are State 2 and 6. These are the rectifying states in a single switching period. Calculating the energy delivered by one of rectifying states only describes half the energy delivered from a single period. Based on the circuit diagram of State 2 in Figure 2.6, the energy delivered to the output from a single rectification state is:

$$\frac{E_{out}}{2} = \int_0^{\tau_2} \bar{V}_{out}(\bar{I}_{in} - i_{Lv}(t))dt \quad (2.4.1)$$

Substituting Equations (2.2.8), (2.2.9), and (2.2.11) from State 2, E_{out} becomes

$$E_{out} = 4L_v \left(\bar{I}_{in}^2 + \bar{I}_{in} \sqrt{\frac{C_v}{L_v}} \bar{V}_{out} \right) \quad (2.4.2)$$

To solve for the input energy per period, the input voltage source, \bar{V}_{in} is observed. Since, \bar{V}_{in} is always connected to the input inductor, L_{in} , then E_{in} results in

$$E_{in} = \frac{\bar{V}_{in} \bar{I}_{in}}{f_{sw}} \quad (2.4.3)$$

where f_{sw} is the switching frequency of the converter, and is defined as follows

$$f_{sw} = \frac{1}{\tau_{sw}} = \frac{1}{2(\tau_1 + \tau_2 + \tau_3 + \tau_4)} \quad (2.4.4)$$

Since the converter is assumed ideal, E_{in} can be equated to E_{out} , and this results in:

$$E_{in} = E_{out} \quad (2.4.5)$$

$$\frac{\bar{V}_{in}}{f_{sw}} = 4L_v \bar{I}_{in} + 2\sqrt{C_v L_v} \bar{V}_{out} \quad (2.4.6)$$

Solving for \bar{I}_{in} gives:

$$\bar{I}_{in} = \frac{\bar{V}_{in}}{4L_v f_{sw}} - \sqrt{\frac{C_v}{L_v}} \bar{V}_{out} \quad (2.4.7)$$

With Equation (2.4.7), \bar{I}_{in} , $i_{Lv}(t)$, and $v_{Cv}(t)$ are determined during a switching period in steady state.

2.4.3 Verification of \bar{I}_{in}

In Section 2.2.4, simulations were performed with an ideal current source. However, in the actual system, an input inductor, L_{in} , is used to approximate a current source. Therefore, the calculated average input current should be verified against the simulated input current value. The converter components used for the simulations are shown in Table 2.4, the input inductor and switching frequency are used as variables.

Converter Property	Value
L_v	500 μH
C_v	0.025 μH
\bar{V}_{in}	100V
\bar{V}_{out}	1kV

Table 2.4: Simulated Converter Properties

It is shown that as the ratio between L_{in} and resonant inductor, L_v , increases, L_{in} better approximates a current source and converges upon the original solution to the average input current, \bar{I}_{in} . Table 2.5 shows a comparison of \bar{I}_{in} to the simulated \bar{I}_{in} , as the ratio between L_{in} and L_v is increased. As expected, the simulated average input current matches the analytic solution as the ratio $\frac{L_{in}}{L_v}$ is increased.

Switching Frequency	Calculated \bar{I}_{in}	Simulated \bar{I}_{in}		
		$\frac{L_{in}}{L_v} : 10$	$\frac{L_{in}}{L_v} : 100$	$\frac{L_{in}}{L_v} : 1000$
4 kHz	5.43A	6.26A	5.52A	5.45A
2 kHz	17.92A	19.9A	18.13A	17.96A

Table 2.5: Simulated Verification of \bar{I}_{in} with different values of L_{in} , and f_{sw}

For lower values of $\frac{L_{in}}{L_v}$, the ripple of the input inductor causes an offset in the solution of the average input current. This situation is presented in Figure 2.11, and shows that the solution to the average input current would always underestimate the true average input current.

2.5 Maximum Switching Frequency Limitation

The operation of the proposed converter is limited by a maximum switching frequency, which occurs when the resonant capacitor voltage, $v_{Cv}(t)$, reaches a maximum of \bar{V}_{out} in State 1, and immediately transitions to State 3. To determine the frequency limit, volt second balance is applied to the input inductor, L_{in} , over States 1 to 4, and results in Equation (2.5.1)

$$\int_{t_0}^{\frac{T_{sw}}{2}} \bar{V}_{in} dt = \int_{t_0}^{t_1} v_{Cv}(t) dt + \int_{t_1}^{t_2} v_{Cv}(t) dt + \int_{t_2}^{t_3} v_{Cv}(t) dt + \int_{t_3}^{t_4} v_{Cv}(t) dt \quad (2.5.1)$$

As previously mentioned, the converter immediately transfers from State 1 to State 3 when $v_{Cv}(t)$ reaches the output voltage, \bar{V}_{out} . Thus, State 2 does not exist in the case of

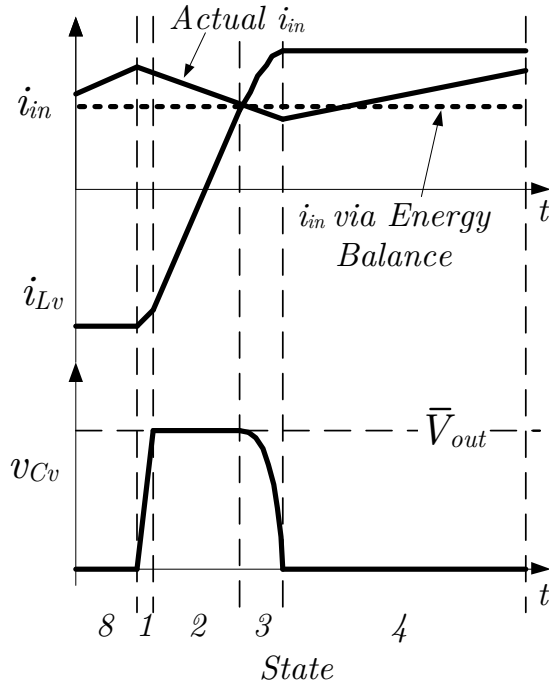


Figure 2.11: Waveforms of $i_{Lv}(t)$, $v_{Cv}(t)$, and $i_{in}(t)$ with ripple added to $i_{in}(t)$.

the maximum frequency limit, and does not need to be considered in Equation (2.5.1). In addition, $v_{Cv}(t)$ is 0V for the duration of State 4, and its integral equates to 0. Using these facts, Equation (2.5.1) becomes

$$\int_{t_0}^{\frac{\tau_{sw}}{2}} \bar{V}_{in} dt = \int_{t_0}^{t_1} v_{Cv}(t) dt + \int_{t_1}^{t_2} v_{Cv}(t) dt \quad (2.5.2)$$

Substituting the state equations for $v_{Cv}(t)$ into Equation (2.5.2) would result in

$$\begin{aligned} \int_{t_0}^{\frac{\tau_{sw}}{2}} \bar{V}_{in} dt &= \int_{t_0}^{t_1} (2\bar{I}_{in}\sqrt{\frac{L_v}{C_v}} + \bar{V}_{out}) \sin(\omega_{res}(t - t_0)) dt \\ &\quad + \int_{t_2}^{t_3} \bar{V}_{out} \cos(\omega_{res}(t - t_2)) dt \end{aligned} \quad (2.5.3)$$

During the maximum frequency limit, power is not delivered to the output and the system is in steady state. Therefore, the average input current, \bar{I}_{in} is 0A. This simplifies

Equation (2.5.3) to Equation (2.5.4)

$$\int_{t_0}^{\frac{\tau_{sw}}{2}} \bar{V}_{in} dt = \int_{t_0}^{t_1} \bar{V}_{out} \sin(\omega_{res}(t - t_0)) dt + \int_{t_2}^{t_3} \bar{V}_{out} \cos(\omega_{res}(t - t_2)) dt \quad (2.5.4)$$

To evaluate the integrals, the end conditions for each state must be revisited. State 1 ends when $v_{Cv}(t)$ equals \bar{V}_{out} , and State 3 ends when $v_{Cv}(t)$ reaches 0V. Using these facts to evaluate the integral, and solving for the inverse of the switching period results in

$$\frac{1}{\tau_{sw}} = f_{max} = \frac{\bar{V}_{in}}{\bar{V}_{out}} \frac{\pi}{2} f_{res} \quad (2.5.5)$$

where

$$f_{res} = \frac{1}{2\pi\sqrt{L_v C_v}} \quad (2.5.6)$$

and f_{max} is the maximum switching frequency

Verification of f_{max} was accomplished through simulation with two different ratios of the input inductor to the resonant inductor, $\frac{L_{in}}{L_v}$. Using the same converter components as Table 2.4, results of the simulation are presented in Table 2.6.

f_{max} with Current Source	f_{max} with $\frac{L_{in}}{L_v} = 10$	f_{max} with $\frac{L_{in}}{L_v} = 100$
7.07 kHz	7.40kHz	7.09kHz

Table 2.6: Simulated Verification of f_{max}

Chapter 3

Converter Dynamics and Control

This chapter expands upon the analysis of the proposed converter by developing a dynamic model. A controller is then developed to regulate input current. Verification of both the model and controller is accomplished by comparing the analytic model to PSCAD simulation.

3.1 Converter Dynamics

Resonant converter dynamics cannot be directly obtained with standard state-space averaging methods [19]. The state-space averaging method assumes the following:

1. The switching frequency is much higher than the natural frequency of the converter.
2. All inputs are constant for the duration of the switching period.

Both assumptions do not apply to the proposed converter. The first assumption does not apply because of the maximum allowable switching frequency, f_{max} , is below the resonant frequency of the converter. This is seen from Equation (2.5.5) and is repeated as Equation (3.1.1) for convenience.

$$f_{max} = \frac{\bar{V}_{in}}{\bar{V}_{out}} \frac{\pi}{2} f_{res} \quad (3.1.1)$$

The second assumption is invalid because the resonant component states are inputs to the system, which are not constant, but vary at the resonant frequency.

Instead, the dynamic model of the current-based resonant converter is obtained by applying time-averaging to the input inductor and output filter capacitor. This method assumes the dynamics of the resonant network, L_v and C_v , can be ignored for two reasons. The first reason is a consequence of assuming the input voltage, output voltage, and input current are constant for steady state analysis. The filter components required to realize the assumption are large enough that the energy delivered to the filters in a single period have negligible effect on their average values. This is a similar assumption to that made in [20]. The second reason is a result of f_{max} given by Equation (3.1.1). For high step-up ratios, Equation (3.1.1) guarantees that the switching frequency is slower than the resonant frequency of the resonant inductor and capacitor. Thus, the dynamics caused by the resonant components can be ignored.

The assumptions for the dynamic model are identical to the assumptions used for steady state analysis with the addition that the internal dynamics can be ignored. These assumptions are:

1. All components are ideal.
2. The ratio between the input inductor, L_{in} , and resonant inductor, L_v , should be much greater than 1, $\frac{L_{in}}{L_v} \gg 1$, such that the input inductor can be assumed to be a constant current source.
3. All sources are constant over a switching period.
4. Energy balance is maintained between the input and output of the converter.
5. Internal dynamics of the resonant tank are much faster than the switching period and can be ignored or, equivalently, the energy stored in the tank elements is much smaller than that stored in the input inductor, L_{in} .

The dynamics included in the model are the input inductor, L_{in} , and output capacitor C_{out} . The dynamic equation for the input inductor is derived by averaging the voltage applied across it over one switching period, τ_{sw} . Similarly, the dynamic equation for the output capacitor is produced by averaging the current flow into the output capacitor over a switching period.

Referring to Figure 2.4, time averaging is applied across the input inductor would result in the dynamic equation for L_{in} , Equation (3.1.2).

$$L_{in} \frac{d\langle i_{in}(t) \rangle_{\tau_{sw}}}{dt} = \langle v_{in}(t) \rangle_{\tau_{sw}} - \langle v_{Cv}(t) \rangle_{\tau_{sw}} \quad (3.1.2)$$

where the following notation is employed

$$\langle x(t) \rangle_{\tau_{sw}} = \frac{1}{\tau_{sw}} \int_0^{\tau_{sw}} x(t) dt \quad (3.1.3)$$

Assuming that the input sources are constant over a switching period implies that the dynamic waveforms for the resonant capacitor and inductor do not differ much from the steady state waveforms. Thus, the steady state equations for the resonant capacitor voltage developed in Chapter 2 can be used to express the averaged resonant capacitor voltage in terms of system quantities and state variables, and results in Equation (3.1.4)

$$L_{in} \frac{d\langle i_{in}(t) \rangle_{\tau_{sw}}}{dt} = \langle v_{in}(t) \rangle_{\tau_{sw}} - 4L_v f_{sw} \left[\langle i_{in}(t) \rangle_{\tau_{sw}} + \sqrt{\frac{C_v}{L_v}} \langle v_{out}(t) \rangle_{\tau_{sw}} \right] \quad (3.1.4)$$

Averaging the current into the output capacitor can be described as

$$C_{out} \frac{d\langle v_{out}(t) \rangle_{\tau_{sw}}}{dt} = \frac{P_{out}}{\langle v_{out}(t) \rangle_{\tau_{sw}}} - \frac{\langle v_{out}(t) \rangle_{\tau_{sw}}}{R_{Load}} \quad (3.1.5)$$

where P_{out} is the energy delivered to the output over a switching period. P_{out} is found by using Equation (2.4.2), which is the energy delivered to the output over half a switching

period, E_{out} . The output power delivered during a switching period would be

$$P_{out} = f_{sw}E_{out} \quad (3.1.6)$$

Substituting E_{out} into P_{out} and using that result in the dynamic equation of the output capacitor produces

$$\begin{aligned} C_{out} \frac{d\langle v_{out}(t) \rangle_{\tau_{sw}}}{dt} &= \frac{4L_v f_{sw}}{\langle v_{out}(t) \rangle_{\tau_{sw}}} \left(\langle i_{in}(t) \rangle_{\tau_{sw}}^2 + \sqrt{\frac{C_v}{L_v}} \langle v_{out}(t) \rangle_{\tau_{sw}} \langle i_{in}(t) \rangle_{\tau_{sw}} \right) \\ &\quad - \frac{\langle v_{out}(t) \rangle_{\tau_{sw}}}{R_{Load}} \end{aligned} \quad (3.1.7)$$

It should be noted that the dynamic equation assumes an ideal current source. However, as discussed in Section 2.4.3, when an input inductor is used instead of an ideal current source, the solution for the average input current is offset due to the input current ripple. Thus, it is expected that the dynamic equations would produce an input current lower than that of the simulated converter. The predicted output voltage from the analytic equations would also be lower due to the lower input current.

To verify the accuracy of the dynamic equations, a step-response was performed with the analytic model, and compared to the PSCAD simulation. A step in the input voltage, $v_{in}(t)$, and the switching frequency, f_{sw} , was provided to the dynamic equations, which are the input variables of Equation (3.1.4) and (3.1.7). Both step responses start with an input voltage of 100V and a switching frequency of 4kHz.

The step response for the input voltage provides a step input from 100V to 200V, and a separate step response changes the switching frequency from 4kHz to 1kHz. The converter properties for simulation are listed in Table 3.1 and the step responses are shown in Figure 3.1 to 3.4

Converter Property	Value
C_{out}	$500\mu F$
L_{in}	5 mH
L_v	$500 \mu H$
C_v	$0.025\mu F$
R_{Load}	1800Ω

Table 3.1: Simulated Converter Properties

Both step responses show the analytic model and PSCAD simulations are similar, but the analytic model is offset from the averaged value of the PSCAD simulation. Similar to the steady state analysis, the analytic model under estimates the value of both the input current and output voltage. For comparison, Figure 3.5 and 3.6 use a input inductor to resonant inductor ratio, $\frac{L_{in}}{L_v}$, of 100 instead of 10 to better approximate an ideal current source. The figures show the simulation and analytic model converging and implies that the dynamic equations can be used for control.

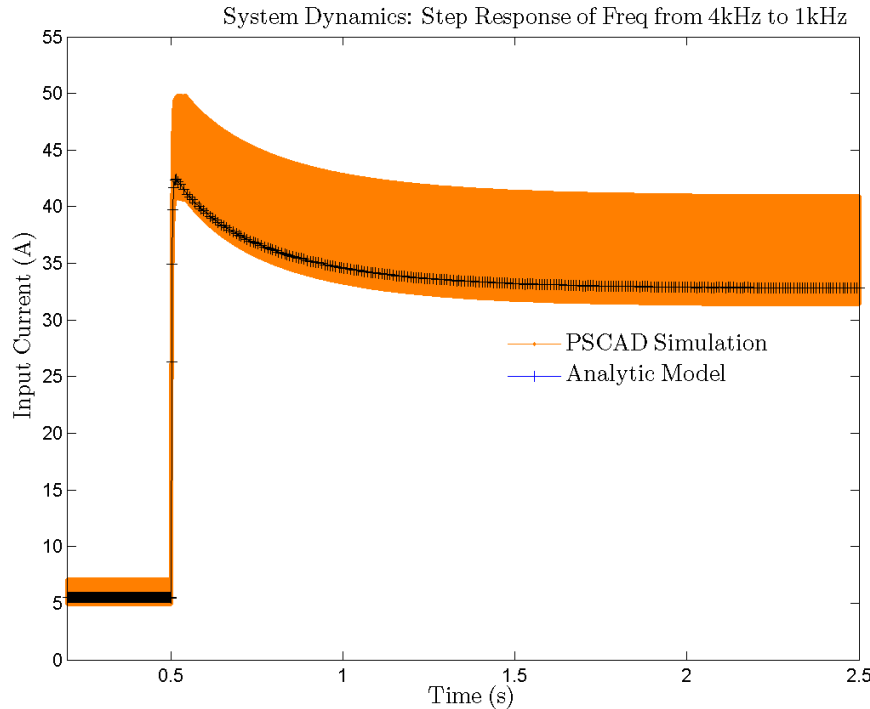


Figure 3.1: Step Response of $i_{in}(t)$ due to a step in switching frequency from 4kHz to 1kHz

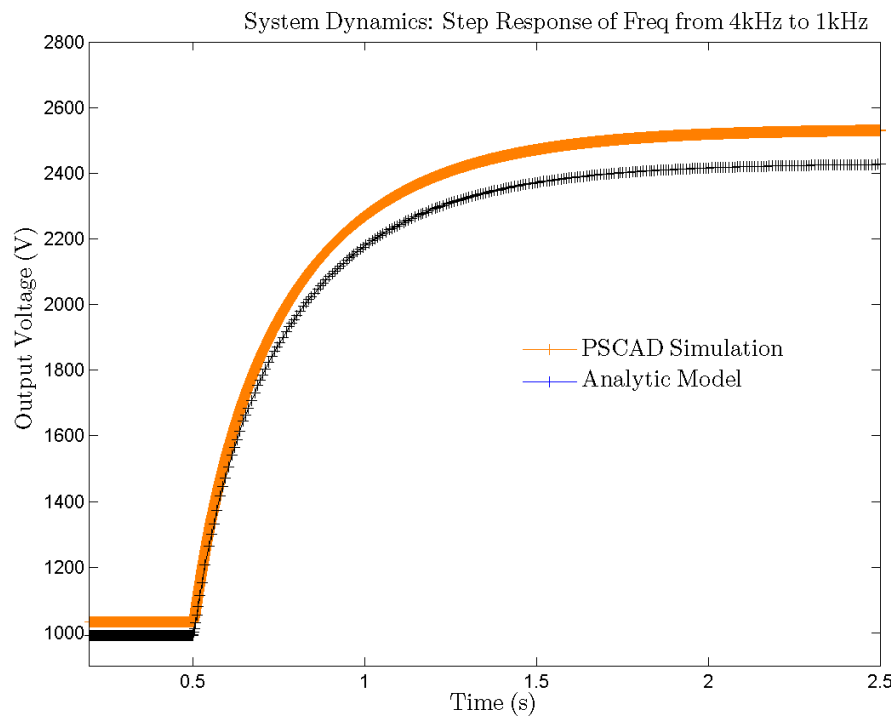


Figure 3.2: Step Response of $v_{out}(t)$ due to a step in switching frequency from 4kHz to 1kHz

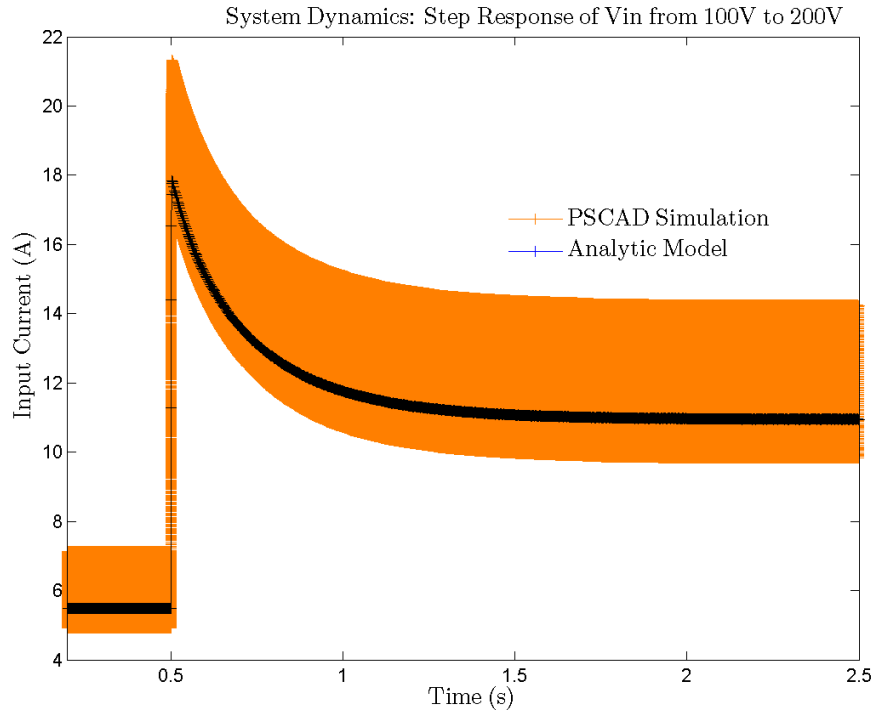


Figure 3.3: Step Response of $i_{in}(t)$ due to a step in $v_{in}(t)$ from 100V to 200V

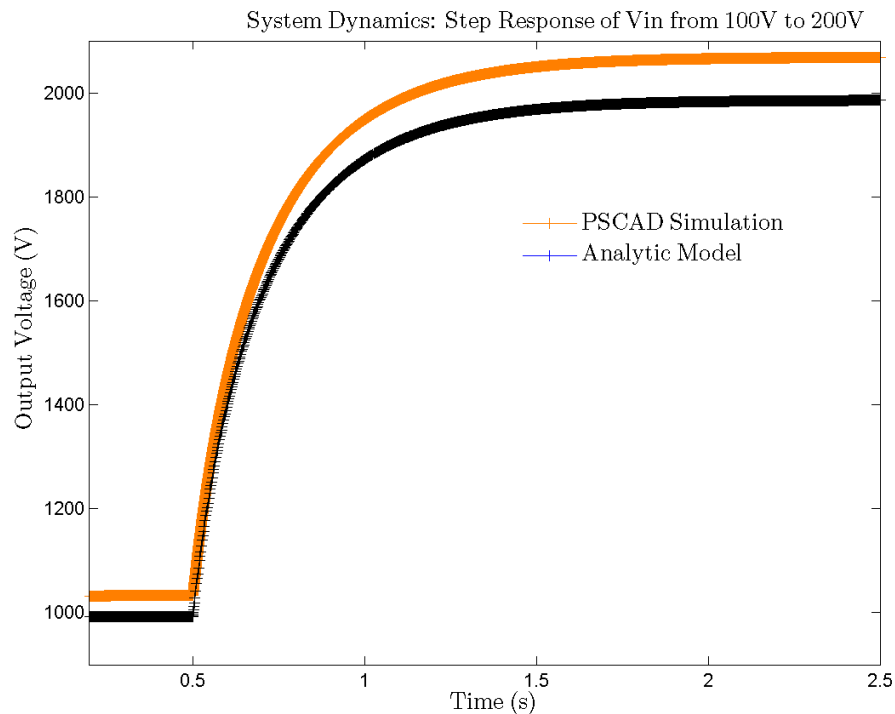


Figure 3.4: Step Response of $v_{out}(t)$ due to a step in $v_{in}(t)$ from 100V to 200V

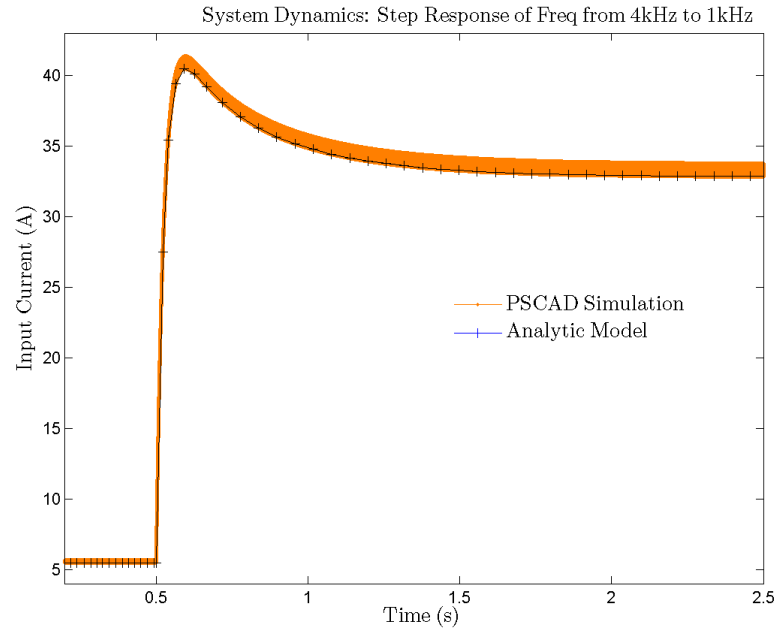


Figure 3.5: Step Response of $i_{in}(t)$ due to a step in switching frequency from 4kHz to 1kHz with L_{in} of 50mH

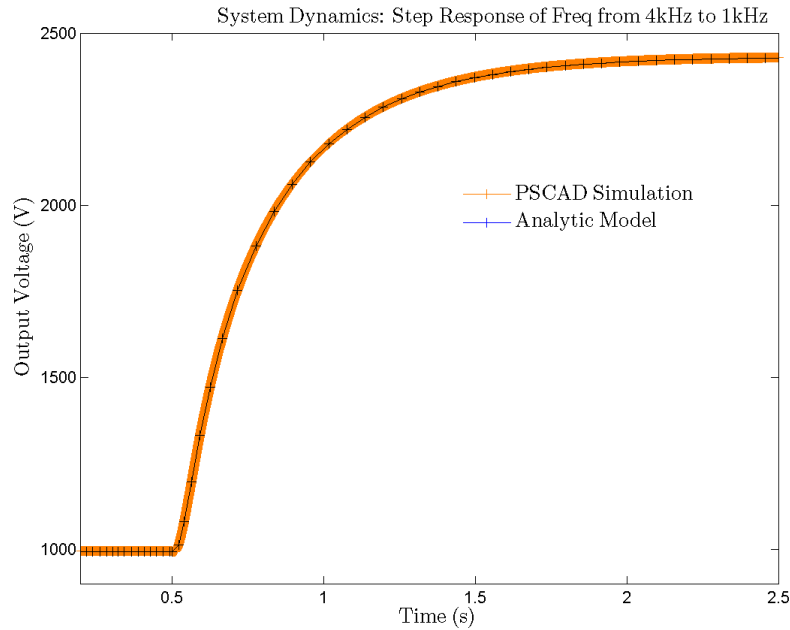


Figure 3.6: Step Response of $v_{out}(t)$ due to a step in switching frequency from 4kHz to 1kHz with L_{in} of 50mH

3.2 Current Compensator

This section develops a method of control for the input current while the input and output voltage are assumed constant. The purpose of this section is to determine a method to manage the nonlinear aspects of the dynamic equations.

The first option is to apply perturbation and linearization to the plant. The input current and switching frequency are perturbed while the input and output voltage are held constant. Small signal AC quantities of the perturbation are represented by \hat{x} .

$$L_{in} \frac{d}{dt} (\bar{I}_{in} + \hat{i}_{in}) = \bar{V}_{in} - 4L_v(\bar{f}_{sw} + \hat{f}_{sw}) \left[(\bar{I}_{in} + \hat{i}_{in}) + \sqrt{\frac{C_v}{L_v}} \bar{V}_{out} \right] \quad (3.2.1)$$

Separating the DC and AC terms of Equation (3.2.1) would result in the following equations

$$L_{in} \frac{d}{dt} \bar{I}_{in} = 0 = V_{in} - 4L_v \bar{f}_{sw} \left[\bar{I}_{in} + \sqrt{\frac{C_v}{L_v}} \bar{V}_{out} \right] \quad (3.2.2)$$

$$L_{in} \frac{d}{dt} \hat{i}_{in} = 4L_v(\bar{f}_{sw} \hat{i}_{in} + \hat{f}_{sw} \bar{I}_{in} + \hat{f}_{sw} \hat{i}_{in}) - 4L_v \sqrt{\frac{C_v}{L_v}} \bar{V}_{out} \hat{f}_{sw} \quad (3.2.3)$$

From Equation (3.2.3), a small signal plant can be found by linearizing and rearranging terms to solve the small signal input current in terms of the small signal switching frequency. The resulting plant equation is

$$\hat{i}_{in} = G_p \frac{1}{\frac{s}{\omega_p} + 1} \hat{f}_{sw} \quad (3.2.4)$$

with coefficients of

$$G_p = -\frac{\bar{V}_{in}}{4L_v \bar{f}_{sw}^2} \quad (3.2.5)$$

$$\omega_p = 4 \frac{L_v}{L_b} \bar{f}_{sw} \quad (3.2.6)$$

The operating point can be substituted into the plant to highlight the dependence on the state variable $i_{in}(t)$. This resulting equation for G_p is

$$G_p = \frac{\left(\bar{I}_{in} + \sqrt{\frac{C_v}{L_v}}\right)^2 4L_v}{\bar{V}_{in}} \quad (3.2.7)$$

The gain, G_p , is shown to be dependent upon the linearized operating point. The plant may be compensated assuming the highest possible value of G_p . However, in this case the system would display excessively slow dynamics over a large portion of the operating range. This is not acceptable because the response of the compensated converter should be independent of its operating point.

Another approach is used to mitigate the nonlinear aspect of the dynamic equation, (3.1.4). In Equation (3.1.4), the switching frequency, which is the control variable, is multiplied by the state, the input current. To mitigate the nonlinearity, an input variable u is created, and is defined as

$$u = 4L_v f_{sw} \left[\langle i_{in}(t) \rangle_{\tau_{sw}} + \sqrt{\frac{C_v}{L_v}} \bar{V}_{out} \right] \quad (3.2.8)$$

The resulting dynamic equation becomes

$$L_{in} \frac{d\langle i_{in}(t) \rangle_{\tau_{sw}}}{dt} = \bar{V}_{in} - u \quad (3.2.9)$$

By transforming the system into the Laplace domain, the plant becomes

$$I_{in}(s) = \frac{1}{L_{in}s} [\bar{V}_{in} - u] \quad (3.2.10)$$

In Equation (3.2.10), the modified system is simply an integrator with the input voltage as a disturbance.

The complete control model is shown in Figure 3.7. The output of the system is

$I_{in}(s)$, which is filtered and used for feedback into a PI compensator to produce the input variable u . The filtered input current, $I_{in\ fil}(s)$ is simultaneously used to create a nonlinear gain, which is needed to extract the control variable, f_{sw} , from u . The control variable is then used to operate the converter. The nonlinear gain is found by solving Equation (3.2.8) for the switching frequency, which results in

$$f_{sw} = \frac{u}{4L_v \left[\langle i_{in}(t) \rangle_{\tau_{sw}} + \sqrt{\frac{C_v}{L_v}} \bar{V}_{out} \right]} \quad (3.2.11)$$

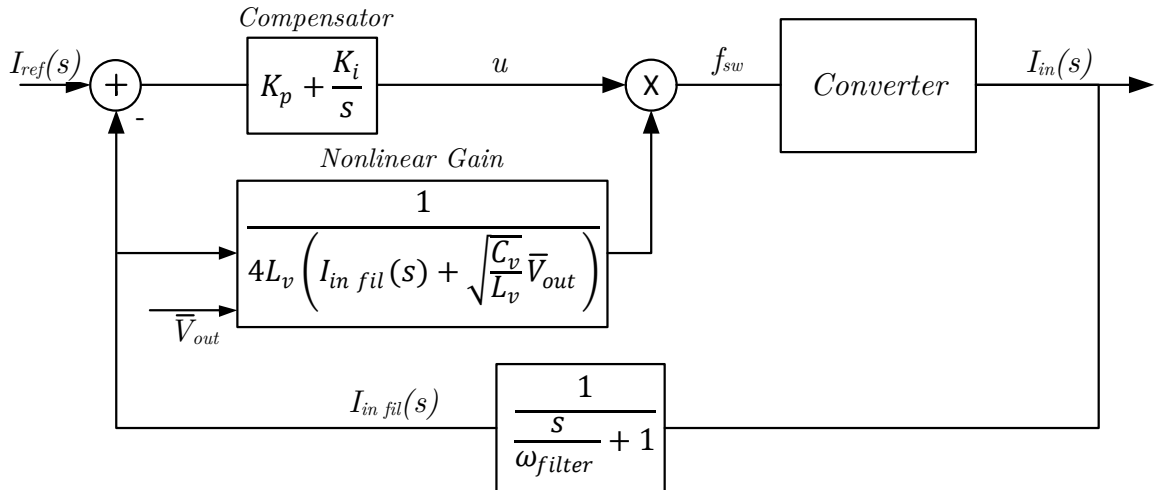


Figure 3.7: Complete Control Loop

To verify the proposed control method, the complete control model was implemented in PSCAD and compared to the analytic model given by Equation (3.2.10). Figure 3.8 shows the resulting control loop employed for compensator design.

Based on the analytical model, a compensator was designed for a system with the quantities listed in Table 3.2. Details of the compensator design are given in Appendix A. In addition, details of the current filter required for the feedback loop are also discussed in Appendix A.

Applying the compensator and current filter, the resulting closed loop response to

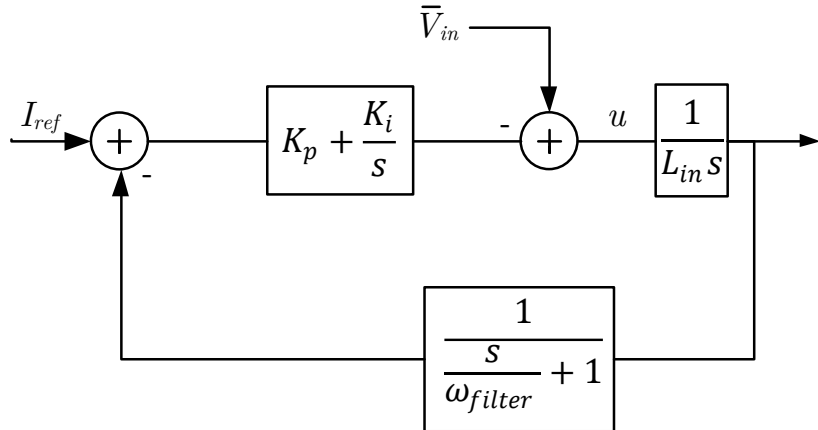


Figure 3.8: Analytic Model

Converter Property	Value
L_{in}	5mH
L_v	500 μ H
C_v	0.025 μ H
\bar{V}_{in}	100V
\bar{V}_{out}	1kV

Table 3.2: Converter Properties for Current Compensator Simulation

disturbances and a step in the input current reference is shown in Figure 3.9 to Figure 3.11. All three responses show good matching between the analytic model and simulation. The unfiltered response of the input current for both the analytic model and simulation are plotted against each other for all three figures. Figure 3.9 shows a step response of the input current set point from 10A to 50A. Figure 3.10 shows the response of the system due to a disturbance of the input voltage, which was changed from 100V to 110V. The last figure, Figure 3.11, shows the response of the system due to a disturbance on the output voltage for a change of 1kV to 1.1kV. The analytic model does not contain a dependence on the output voltage, and simulation shows that the output voltage does have little effect on the input current.

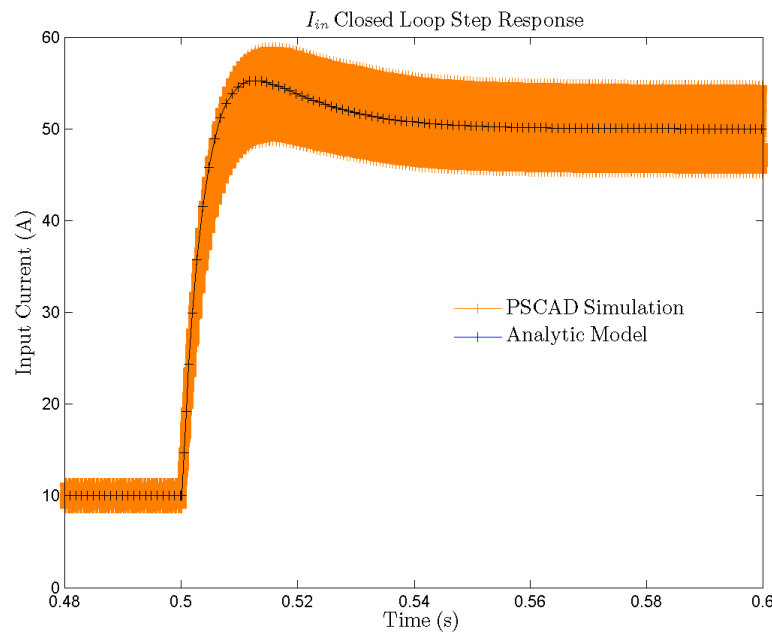


Figure 3.9: Simulation response comparing $i_{in}(t)$ of the Analytic model and PSCAD simulations when a step in reference input from 10A to 50A is applied.

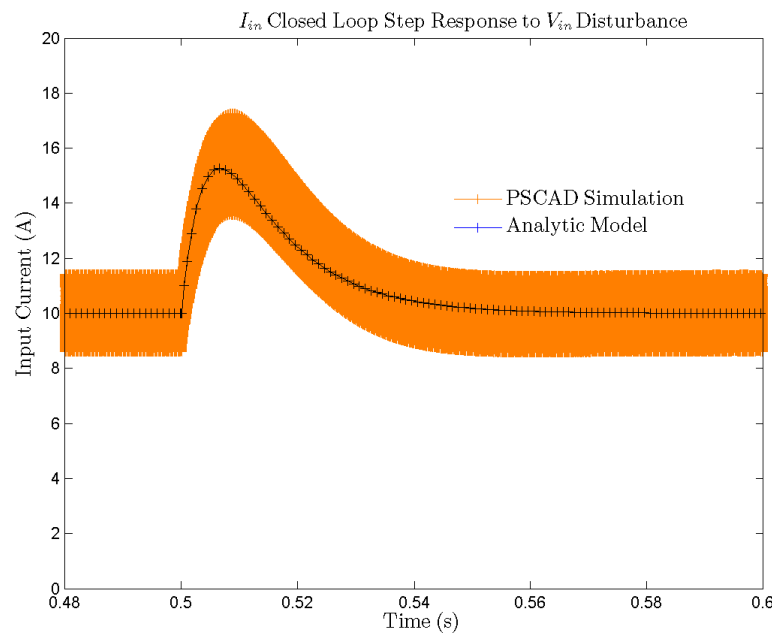


Figure 3.10: Simulation response comparing $i_{in}(t)$ of the Analytic model and PSCAD simulations when a step in input voltage from 100V to 110V is applied.

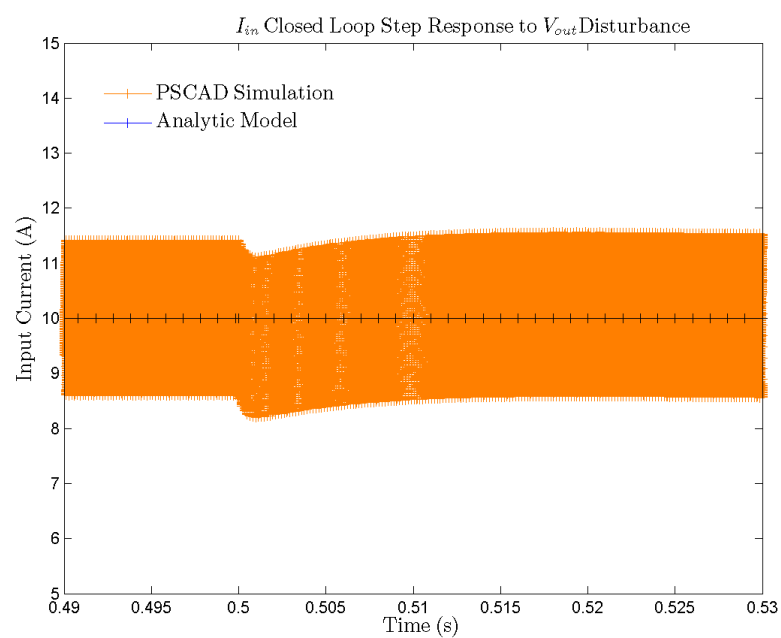


Figure 3.11: Simulation response comparing $i_{in}(t)$ of the Analytic model and PSCAD simulations when a step in output voltage from 1kV to 1.1kV is applied.

Chapter 4

Converter Design

This chapter develops the component ratings, theoretical efficiency, and design procedure by using the state equations developed in Chapter 2. However, a refinement to the average input inductor current is first introduced to improve the accuracy of the component ratings and theoretical efficiency. These topics are discussed in five sections. The first section introduces a refinement to the solution of the average input inductor current. The second section examines the waveforms of the switches, and develops switch characteristics and requirements. The third section develops the passive component ratings. The fourth section uses the information from the previous sections to estimate the efficiency of the converter, and the final section details the design methodology for choosing each component.

4.1 Refinement in \bar{I}_{in}

In the analysis from Chapter 2, the input inductor was assumed large enough to mimic a constant current source, as such the ripple of the input current has been omitted from analysis. This results in an offset in the estimated average value of the input current. Once again using Figure 2.11, and repeating it as Figure 4.1, it is shown how the original average input current found through energy balance would differ from the actual input

current. For reference, the original equation for the average input current, Equation (2.4.7), is repeated as Equation (4.1.1)

$$\bar{I}_{in} = \frac{\bar{V}_{in}}{4L_v f_{sw}} - \sqrt{\frac{C_v}{L_v}} \bar{V}_{out} \quad (4.1.1)$$

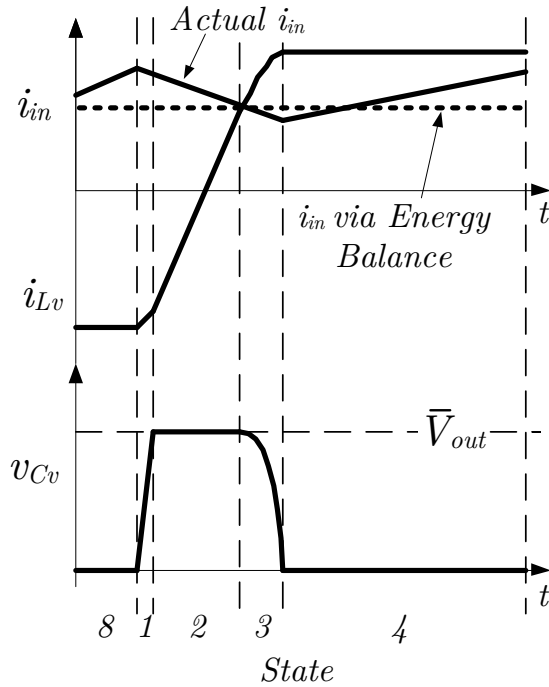


Figure 4.1: Waveforms of $i_{Lv}(t)$, $v_{Cv}(t)$, and $i_{in}(t)$ with ripple added to $i_{in}(t)$.

By inspecting Figure 4.1, a refinement to the estimated average input current can be made by utilizing the ripple of the input current. The original averaged input current, \bar{I}_{in} , was solved by assuming the input current, $i_{in}(t)$ and resonant inductor current, $i_{Lv}(t)$, intersected at \bar{I}_{in} . Instead, it can be assumed that energy balance solved for the resonant inductor's initial current at State 3 instead of \bar{I}_{in} , as depicted in Figure 4.1, and the initial current at State 3 is assumed to be offset from the average input current by half the peak to peak input current. From these assumptions, Equation (4.1.1) becomes Equation (4.1.2).

$$\bar{I}_{in} - \frac{1}{2}\Delta i_{in_{pk-pk}} = \frac{\bar{V}_{in}}{4L_v f_{sw}} - \sqrt{\frac{C_v}{L_v}}\bar{V}_{out} \quad (4.1.2)$$

Before solving for the refined average input current, an assumption was made about the input current ripple. Since voltage balance across the input inductor, L_{in} depends on the resonant capacitor voltage, $v_{Cv}(t)$ and input voltage, \bar{V}_{in} . A simple approximation of the ripple is to only use the states with constant voltage applied across L_{in} to estimate the ripple.

This approximation is justified because the switching module's purpose is to aid in the turn "on" and turn "off" process of the rectifying diode, D_{rect} . State 2 is the rectifying state where energy is transferred to the output, and State 4 is the input inductor charging state required to maintain volt-sec balance across L_{in} . State 1 and State 3 can be viewed as transition states where the module aids in turning D_{rect} "on" and "off", and can be assumed to be short in duration. Thus, the ripple can be calculated through State 2 or State 4. State 2 is chosen to calculate the ripple because the duration of State 4 is dependent on the duration of States 1 to 3. Therefore, using State 4 would not yield a simpler expression for the input current ripple.

The peak to peak input ripple current can be approximated by

$$\Delta i_{in_{pk-pk}} \approx \frac{\bar{V}_{in} - \bar{V}_{out}}{L_{in}}\tau_2 \quad (4.1.3)$$

Using Equation (2.2.11) to replace τ_2 results in the full expression as follows

$$\Delta i_{in_{pk-pk}} \approx 2\frac{L_v}{L_{in}} \left(\frac{\bar{V}_{in}}{\bar{V}_{out}} - 1 \right) \sqrt{\bar{I}_{in}^2 + \bar{I}_{in}\sqrt{\frac{C_v}{L_v}}\bar{V}_{out}} \quad (4.1.4)$$

By substituting Equation (4.1.4) into Equation(4.1.2) results in

$$\bar{I}_{in} - \frac{L_v}{L_{in}} \left(\frac{\bar{V}_{in}}{\bar{V}_{out}} - 1 \right) \sqrt{\bar{I}_{in}^2 + \bar{I}_{in} \sqrt{\frac{C_v}{L_v} \bar{V}_{out}}} = \frac{\bar{V}_{in}}{4L_v f_{sw}} - \sqrt{\frac{C_v}{L_v} \bar{V}_{out}} \quad (4.1.5)$$

Rearranging the terms into quadratic form.

$$a\bar{I}_{in}^2 + b\bar{I}_{in} + c = 0 \quad (4.1.6)$$

where

$$a = \left[1 - \left(\left(\frac{\bar{V}_{in}}{\bar{V}_{out}} - 1 \right) \frac{L_v}{L_{in}} \right)^2 \right] \quad (4.1.7)$$

$$b = - \left[2 \left(\frac{\bar{V}_{in}}{4L_v f_{sw}} - \sqrt{\frac{C_v}{L_v} \bar{V}_{out}} \right) + \left(\left(\frac{\bar{V}_{in}}{\bar{V}_{out}} - 1 \right) \frac{L_v}{L_{in}} \right)^2 \sqrt{\frac{C_v}{L_v} \bar{V}_{out}} \right] \quad (4.1.8)$$

$$c = \left(\frac{\bar{V}_{in}}{4L_v f_{sw}} - \sqrt{\frac{C_v}{L_v} \bar{V}_{out}} \right)^2 \quad (4.1.9)$$

The final solution for the refined \bar{I}_{in} is the larger solution of the quadratic equation. The refinement to \bar{I}_{in} is based on the assumption that State 2 is much longer than States 1 and 3. Since State 2 is also the rectifying state then the refined \bar{I}_{in} should only be considered valid near maximum power transfer to maintain this assumption.

4.1.1 Verification of the Refinement to \bar{I}_{in}

The original \bar{I}_{in} and the refined \bar{I}_{in} are verified against the simulated input current. The converter components used for the simulations are shown in Table 4.1. Figure 4.2 plots the original and refined \bar{I}_{in} against the simulated values, and Table 4.2 shows the error between the calculated \bar{I}_{in} and simulated.

The refined version of \bar{I}_{in} is not exact due to the omission of State 1 and 3, but is a better approximation to the simulated values than the original solution for \bar{I}_{in} . The original

Converter Property	Value
L_{in}	5mH
L_v	500 μ H
C_v	0.025 μ H
\bar{V}_{in}	100V
\bar{V}_{out}	1kV

Table 4.1: Simulated Converter Properties

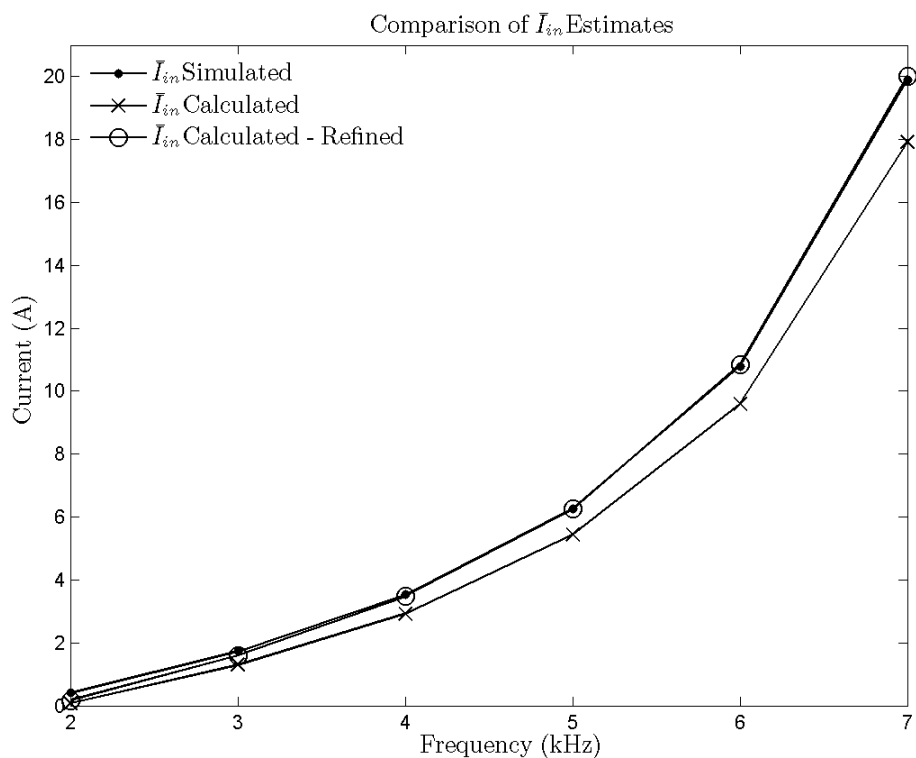


Figure 4.2: Comparison of original and refined average input current to the simulated average input current.

solution yields simpler equations and provides more insight into the relationship between converter components and operating specifications while the refined version should be used in calculating component ratings.

Switching Frequency	Error in %		Error in % of Rated \bar{I}_{in}	
	Original \bar{I}_{in} (%)	Refined \bar{I}_{in} (%)	Original \bar{I}_{in} (%)	Refined \bar{I}_{in} (%)
7 kHz	82.93	58.54	1.71	1.21
6 kHz	24.42	6.98	2.11	0.60
5 kHz	17.00	1.42	3.02	0.25
4 kHz	13.26	0.16	4.17	0.05
3 kHz	11.11	0.46	6.03	0.25
2 kHz	9.95	0.60	9.95	0.60

Table 4.2: Simulated Verification of the refined version of \bar{I}_{in} . Rated \bar{I}_{in} is 19.9A

4.2 Switch Requirements and Ratings

This section specifies the switch ratings required by the switches in the proposed converter. The following discussion on switch requirements and ratings is heavily dependent on State 4 and 8, and the current that conducts through the resonant inductor during these states. The circuit diagram of State 4, and the resonant inductor current equation during State 4 are repeated here for convenience, as they will be referred to in the following sub-sections.

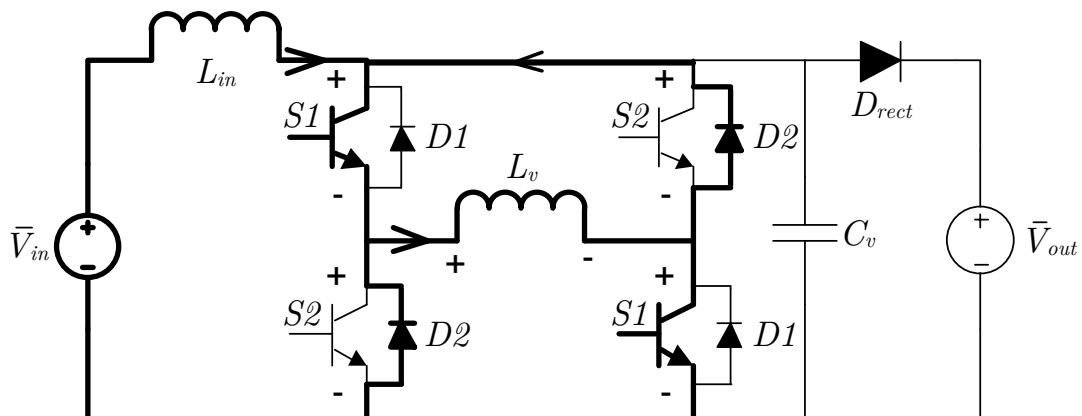


Figure 4.3: Current paths of States 4. Arrows on the branches indicate current direction.

$$i_{Lv}(t) = \bar{I}_{in} + \sqrt{\frac{C_v}{L_v}} \bar{V}_{out} \quad t = [t_3, t_4] \quad (4.2.1)$$

4.2.1 Switch Currents

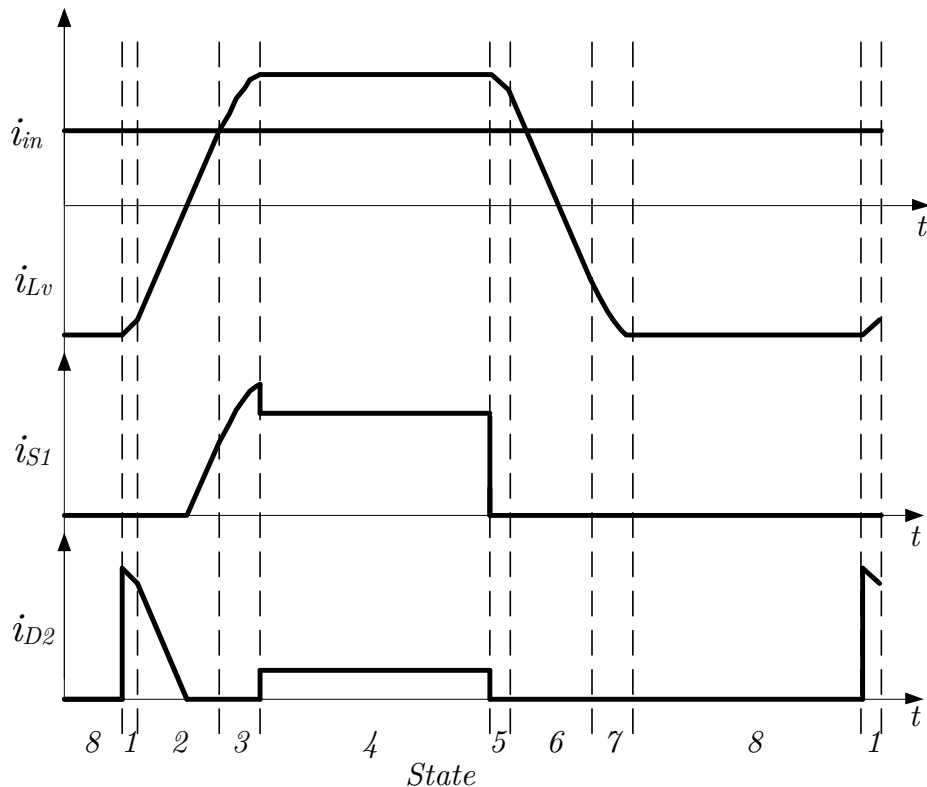


Figure 4.4: Switch currents for S1 and D2.

The purpose of this section is to detail the switch currents for use in determining their ratings. The current conducted by switches S1 and D2 in the switching module are shown in Figure 4.4. The waveforms of S2 and D1 are identical, but conduct during States 5 to 8 instead.

During States 1 to 3, the resonant inductor current, $i_{Lv}(t)$, is either conducting through S1 or D2, as shown in Figure 4.4. This deviates during State 4 when both S1 and D2 conduct $i_{Lv}(t)$. The division of current can be described using $i_{Lv}(t)$ of State

4, Equation (4.2.1), and Figure 4.3.

State 4 is the input inductor charging period. The resonant capacitor voltage, $v_{Cv}(t)$, is 0V for the duration of the state, and $i_{Lv}(t)$ is constant. $i_{Lv}(t)$ during this state, Equation (4.2.1), can be decoupled into two components. The average input current, \bar{I}_{in} , and a second component. The second component is the current required to charge the resonant capacitor, C_v , from 0V to \bar{V}_{out} . This current is referred to as the resonant current, I_{res} , and is defined as:

$$I_{res} = \sqrt{\frac{C_v}{L_v}} \bar{V}_{out} \quad (4.2.2)$$

By using Figure 4.3 the paths of the different currents can be highlighted. \bar{I}_{in} must conduct through switch S1 and the resonant inductor, L_v . However, L_v must also conduct I_{res} . Since the switches are assumed ideal, I_{res} flows through the high-side S1 and D2 and low-side S1 and D2 equally. Therefore, the current flowing through S1 in State 4 is

$$I_{S1} = \bar{I}_{in} + \frac{1}{2} \sqrt{\frac{C_v}{L_v}} \bar{V}_{out} \quad t = [t_3, t_4] \quad (4.2.3)$$

and the current in D2 during State 4 is

$$I_{D2} = \frac{1}{2} \sqrt{\frac{C_v}{L_v}} \bar{V}_{out} \quad t = [t_3, t_4] \quad (4.2.4)$$

4.2.2 Switch Ratings

This section develops the voltage and current ratings of all the switches in this converter. The current ratings for switches S1, and S2 can be defined with Figure 4.4. The peak switch current occurs at the end of State 3 and is equal in magnitude to Equation (4.2.1). The RMS current could be directly integrated, but an approximation can be made in

the switch waveform to simplify the expression and gain insight into the loss sources. The approximation utilizes the fact that at high step up ratios, the duration of State 4 is much greater than States 1 to 3. This is depicted in Figure 4.5, which shows the simulated inductor currents and resonant capacitor voltage using the parameters in Table 4.3. Thus, the RMS and average current rating of S1 and S2 is dominated by the switch current during State 4 given by Equation (4.2.3), and by association the losses are also dominated by State 4.

Converter Property	Value
L_{in}	5mH
L_v	500 μ H
C_v	0.025 μ H
\bar{V}_{in}	100V
\bar{V}_{out}	1kV
f_{sw}	2kHz

Table 4.3: Converter Properties used to verify current ratings

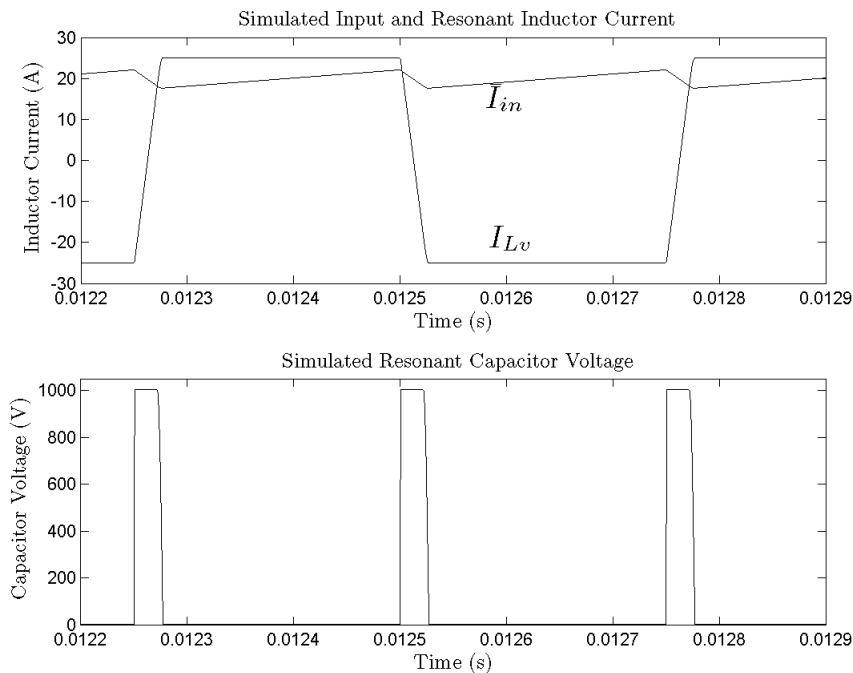


Figure 4.5: Inductor Currents and Resonant Capacitor Voltage using parameters from Table 4.3

Utilizing the approximation, it is assumed that S1 and S2 each conduct the current given by Equation (4.2.3) for half the duration of the switching period. The resulting RMS current rating for S1 and S2 is

$$I_{swRMS} = \frac{1}{\sqrt{2}} \left(\bar{I}_{in} + \sqrt{\frac{C_v}{L_v} \frac{\bar{V}_{out}}{2}} \right) \quad (4.2.5)$$

As a consequence, the average current is

$$I_{swAVG} = \frac{1}{2} \left(\bar{I}_{in} + \sqrt{\frac{C_v}{L_v} \frac{\bar{V}_{out}}{2}} \right) \quad (4.2.6)$$

The average and RMS current of D1 and D2 is also dominated by the current conducted during State 4. This results in

$$I_{swdRMS} = \frac{1}{\sqrt{2}} \left(\sqrt{\frac{C_v}{L_v} \frac{\bar{V}_{out}}{2}} \right) \quad (4.2.7)$$

$$I_{swdAVG} = \frac{1}{2} \left(\sqrt{\frac{C_v}{L_v} \frac{\bar{V}_{out}}{2}} \right) \quad (4.2.8)$$

The switch rating of the rectifying diode, D_{rect} , depends upon State 2 and 5. From Figure 4.6, which is a repeat of Figure 2.6, the peak and average current can be inferred. The peak current is the combination of \bar{I}_{in} and $i_{Lv}(t)$ at the beginning of State 2 or 5, and is given in Equation (4.2.9). The diode current decreases linearly over the rectifying state, and a direct integration results in the average and RMS current presented in Equation (4.2.10), and Equation (4.2.11) respectively.

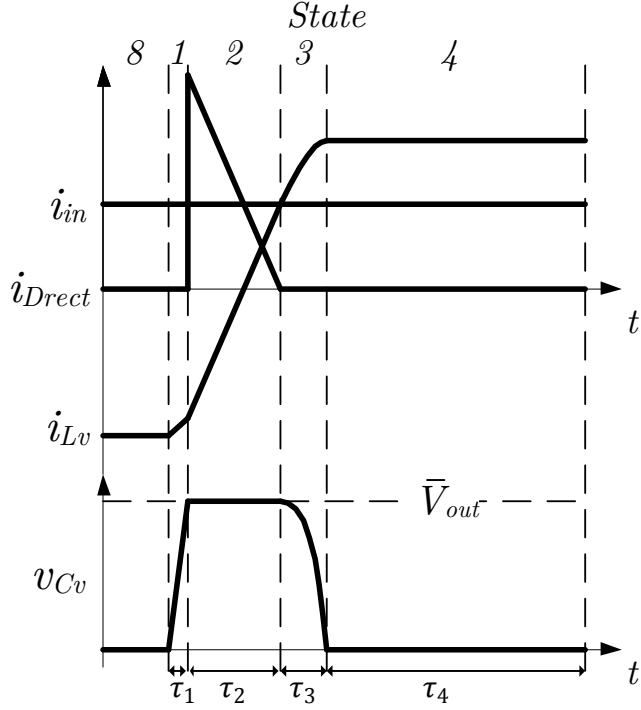


Figure 4.6: The rectifying current, $i_{Drect}(t)$, and the currents that it is composed of $i_{Lv}(t)$ and \bar{I}_{in}

$$I_{dpeak} = 2\sqrt{\bar{I}_{in}^2 + \bar{I}_{in}\sqrt{\frac{C_v}{L_v}}\bar{V}_{out}} \quad (4.2.9)$$

$$I_{davg} = 4f\frac{L_v}{\bar{V}_{out}} \left(\bar{I}_{in}^2 + \bar{I}_{in}\sqrt{\frac{C_v}{L_v}}\bar{V}_{out} \right) \quad (4.2.10)$$

$$I_{drms} = \sqrt{\frac{16}{3}f_{sw}\frac{L_v}{\bar{V}_{out}} \left(\bar{I}_{in}^2 + \bar{I}_{in}\sqrt{\frac{C_v}{L_v}}\bar{V}_{out} \right)} \quad (4.2.11)$$

The voltage rating of D_{rect} , S1, S2, D1, and D2 all depend on the resonant capacitor voltage, $v_{Cv}(t)$. From Figure 4.6, it can be seen that $v_{Cv}(t)$ varies from 0V to \bar{V}_{out} , thus all switches must be rated for \bar{V}_{out} . Since the peak rectifying current is approximately twice that of the average input current, overshoot should be expected. Thus, a safety margin of 50% of \bar{V}_{out} is used.

The switch ratings were verified with simulation and the results of comparison can be found in Table 4.4. The values were calculated using components listed in Table 4.3. Since all quantities are in terms of \bar{I}_{in} , the original and refined versions of \bar{I}_{in} were used for comparison. Due to the approximation that State 4 and State 8 dominate the current rating of the switches, the ratings which use the refined \bar{I}_{in} tend to over estimate the simulated values, but still shows closer agreement to the simulated values.

Switch Rating			
Switch	Original \bar{I}_{in}	Refined \bar{I}_{in}	Simulated
S1/S2	15.18 A_{rms}	16.64 A_{rms}	15.2 A_{rms}
	10.37 A_{avg}	10.74 A_{avg}	11.77 A_{avg}
D1/D2	2.5 A_{rms}	2.5 A_{rms}	2.92 A_{rms}
	1.77 A_{avg}	1.77 A_{avg}	1.45 A_{avg}
D_{rect}	42.34 A_{pk}	46.54 A_{pk}	45.56 A_{pk}
	1.79 A_{avg}	2.17 A_{avg}	1.96 A_{avg}
	7.10 A_{rms}	8.20 A_{rms}	7.78 A_{rms}

Table 4.4: Verification of Switch Ratings

4.3 Passive Component Ratings

This section will discuss the ratings for the input inductor, resonant inductor and resonant capacitor. Similar to the switch voltage ratings, the voltage rating of the resonant inductor is dependent on the resonant capacitor voltage, $v_{Cv}(t)$, thus both the resonant inductor and capacitor should be rated at \bar{V}_{out} with the same safety margin as the switches. The voltage rating for the input inductor is dependent on the difference between \bar{V}_{in} and $v_{Cv}(t)$. Therefore the voltage rating of the input inductor is equal to $\bar{V}_{out} - \bar{V}_{in}$ with a safety margin.

The current ratings for the passive components can be explained with the aid of Figure 4.7. For the input inductor, \bar{I}_{in} is defined by system requirements. However, the ripple component of the input current, $\Delta i_{in_{pk-pk}}$, has previously been discussed in the refinement of \bar{I}_{in} and is given in Equation (4.1.4).

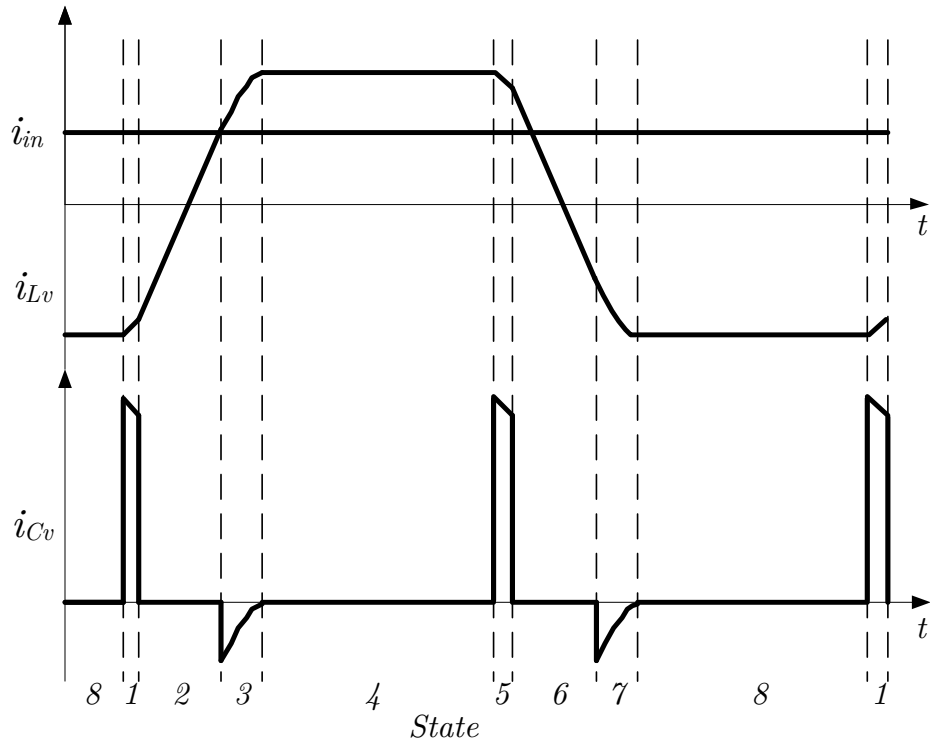


Figure 4.7: Current waveforms for all passive components.

For the resonant inductor, L_v , the peak current is the current that conducts through L_v during the input inductor charging states, States 4 and 8, and is given by Equation (4.2.1). In addition, it is assumed that the current ratings are dominated by State 4 and State 8 for the same reasons used in determining the switch ratings. As a result, the RMS and average current of L_v is equal to the peak current.

The current requirements of the resonant capacitor, C_v , are determined by State 1 and 3. These are the only two states that charge is delivered or removed from the capacitor as depicted in Figure 4.7. In State 1, $i_{L_v}(t)$ and \bar{I}_{in} are directed into C_v , and both are at their peak values. Therefore, the peak current for the capacitor is at the beginning of State 1, and is shown in Equation (4.3.2). There are no simplifying methods to determine the RMS current of the capacitor, and the RMS current is computed and presented in

Equation (4.3.1).

$$I_{Crms} = \sqrt{\frac{f_{sw}}{2\pi f_{res}}} \times \sqrt{\left[(2\bar{I}_{in} + I_{res})^2 \sin^{-1} \left(\frac{I_{res}}{2\bar{I}_{in} + I_{res}} \right) + 2I_{res}\sqrt{\bar{I}_{in} + I_{res}} + \frac{\pi}{2}(I_{res})^2 \right]} \quad (4.3.1)$$

$$I_{Cmax} = 2\bar{I}_{in} + \sqrt{\frac{C_v}{L_v} \bar{V}_{out}} \quad (4.3.2)$$

Selecting C_v is not restricted by the RMS current specification of the part, but the $\frac{dv}{dt}$ rating. Current only flows through the capacitor in State 1 and 3, which has been assumed to be negligible in length for most of the analysis, thus the RMS current rating is low. This can be beneficial since high voltage film capacitors with high RMS ratings may be difficult to procure. In exchange, the peak current is high, hence the $\frac{dv}{dt}$ rating is the limiting factor. The values were calculated using components listed in Table 4.3 and is presented in Table 4.4. Once again, the original and refined versions of \bar{I}_{in} were used for comparison.

Switch	Predicted with I_{in}	Predicted with refined I_{in}	Simulated
C_v	$42.93 A_{pk}$	$47.07 A_{pk}$	$47.04 A_{pk}$
	$1.79 A_{rms}$	$1.86 A_{rms}$	$2.42 A_{rms}$
L_v	$25 A_{rms}$	$27.07 A_{rms}$	$24.1 A_{rms}$

Table 4.5: Verification of Passive Component Ratings

4.4 Theoretical Efficiency

To calculate the theoretical efficiency of the current-based resonant converter, it is assumed that the main loss mechanism is conduction loss since the resonant network provides ZVS for all switching instances except for the turn “on” of the rectifying diode.

Core loss is also assumed to be negligible. Before dividing the losses into the different components, the output power is derived. From energy balance, it is known that the energy delivered to the output over a switching period, E_{out} , is given in Equation (2.4.2). Dividing E_{out} by the switching period results in P_{out} as follows

$$P_{out} = 4L_v f_{sw} \left(\bar{I}_{in}^2 + \bar{I}_{in} \sqrt{\frac{C_v}{L_v}} \bar{V}_{out} \right) \quad (4.4.1)$$

For the efficiency calculation, the following conduction losses are included:

1. Resonant Inductor and Input Inductor Winding Resistance
2. Equivalent series resistance (ESR) of the resonant capacitor
3. Switch conduction losses

IGBTs are used as the active switch, and “on” state conduction is modelled by a constant voltage drop with a resistance in series. The “on” state of the rectifying diode, and free-wheeling diodes of the IGBTs are modelled in the same manner as a constant voltage drop with series resistor. The losses of the converter can be summarized as follows

$$P_{IGBTLoss} = 2V_{dropIGBT}(I_{swAVG}) + 2R_{onIGBT}(I_{swRMS})^2 \quad (4.4.2)$$

$$P_{IGBTDiodeLoss} = 2V_{dropIGBTdiode}I_{swdAVG} + 2R_{onIGBTdiode}(I_{swdRMS})^2 \quad (4.4.3)$$

$$P_{DrectLoss} = V_{dropDrect}I_{davg} + R_{onDrect}I_{drms} \quad (4.4.4)$$

$$P_{componentloss} = R_{Lv}I_{Lrms}^2 + R_{Lin}\bar{I}_{in}^2 + R_{Cesr}i_{Crms}^2 \quad (4.4.5)$$

Of the listed losses, it is expected that the IGBT, and inductor losses will dominate, and that the ESR of C_v will have negligible effect.

4.5 Design Considerations and Component Sizing

For the proposed converter, three components require sizing, the input inductor, resonant inductor, and resonant capacitor. The sizing of the resonant inductor, L_v and the resonant capacitor, C_v , should be used to minimize conduction losses by reducing the currents during the input inductor charging state (State 4 and 8).

During State 4 and 8, the resonant inductor current is constant, and conducts a current of magnitude equal to Equation (4.2.1), which is composed of the average input current, \bar{I}_{in} , and the resonant current, I_{res} . The input current cannot be changed, but I_{res} can be minimized by reducing the resonant capacitor, C_v , and increasing the resonant inductor, L_v . Minimizing I_{res} only constrains the ratio between C_v and L_v .

A constraint can be placed on L_v by examining \bar{I}_{in} . From Equation (4.1.1), the size of L_v directly affects the switching frequency, f_{sw} , assuming V_{in} and V_{out} are predetermined. Therefore, the size of L_v can either limit I_{res} , or be used to determine the full load switching frequency.

Several considerations must also be taken into account when choosing the resonant inductor and capacitor. For the resonant capacitor, C_v , the $\frac{dv}{dt}$ rating will be the limiting factor for C_v as opposed to the RMS current rating, as discussed in Section 4.3. Although L_v conducts a constant current during the longest states, State 4 and 8, the transition states contain high frequencies components. This can be seen in Figure 4.5, thus the inductor must still be a high frequency inductor to minimize losses.

The size of the input inductor, L_{in} , is determined by the ripple requirement of $i_{in}(t)$. The motivation for the sizing is from Equation (4.1.4) where the ripple component of $i_{in}(t)$ is shown to be proportional to the ratio of L_v to L_{in} . However, L_{in} must be large enough to maintain the constant current source assumption of $i_{in}(t)$. Thus, L_{in} is restricted to be at least 10x larger than L_v .

Finding the optimal component size is outside the scope of this thesis, but several relationships are developed in this discussion. To summarize the relations,

1. The ratio of the resonant inductor, L_v , to the input inductor, L_{in} , is used to satisfy input ripple constraint and maintain the constant input current assumption.
2. The ratio of the resonant capacitor to the resonant inductor is used to minimize conduction loss by reducing the resonant inductor current during State 4 and State 8.
3. The size of L_v is used to either set the frequency of operation or to minimize the resonant inductor current, I_{res} .
4. No minimum size restriction exists for the resonant capacitor, C_v . However, it should be larger than the parasitic capacitance of the switching module.

Chapter 5

Experimental Results



Figure 5.1: Experimental Lab Setup

A prototype of the current-based resonant converter was designed and implemented to validate the analysis and investigate the losses. This chapter provides details of the experiment system and results. The first chapter section details the components used for the converter, and the experimental equipment. The second section discusses an improvement made to the switching scheme of the converter. The third section covers experimental results, which includes verifying waveforms and presenting efficiency results. Improvement to the converter are also suggested and validated in the results section.

The chapter concludes with a summary and comparison of the current-based resonant converter to the boost converter and voltage-based resonant converter.

5.1 Experiment Setup

A 4kW prototype of the current-based resonant converter was developed and operated based on open loop control of the converter switching frequency. A circuit diagram of the experimental setup is given in Figure 5.2, and operating ranges are given in Table 5.1. The prototype's operation was tested at multiple input voltages with a fixed output voltage of 1kV. The input voltage for the converter was provided by a DC generator when V_{in} was below 130V. For voltages above 130V, the filtered output of a 3-phase rectifier was used. The rectifier was fed by a transformer connected to the AC grid. Both input and output voltages were supported by a capacitor bank, both sized at 4.8mF. As a safety precaution, the output capacitor was over-sized to ensure that a dump of energy from the inductor at full load would only cause the output voltage to rise by 100V.

Efficiency measurements were performed with four Tektronix TX1 high precision multimeters. Input voltage and output current were measured directly with the multimeters, while the multimeters measured the input current through a shunt resistor, and the output voltage through a calibrated resistor divider.

Converter Specifications	Value
V_{in}	100 - 200 V
V_{out}	1 kV
f_{sw}	12 - 1 kHz
$P_{out_{rated}}$	4 kW

Table 5.1: Experimental Specifications

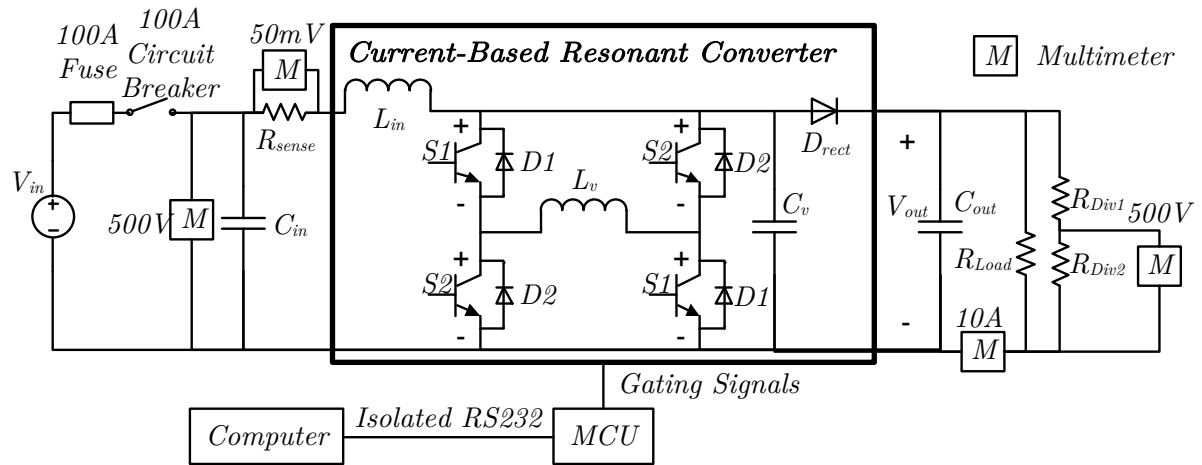


Figure 5.2: Schematic for Experimental Setup

5.1.1 Prototype Parameters

The components chosen for this prototype can be found in Tables 5.2 and 5.3. The tables detail the passive components and switching components respectively, and includes their loss mechanics. The loss mechanics were either measured or found from the datasheets. The rectifying diode, D_{rect} , only specified a forward voltage drop, and no series resistance value could be extrapolated from the datasheet. R_{Lin} also includes the wiring and contact

Converter Component	Value	Properties
L_v	$500 \mu\text{H}$	$R_{Lv} = 13.37\text{m}\Omega$, $I_{max} = 182\text{A}$
C_v	$0.025 \mu\text{F}$	$R_{Cesr} = 37.6\text{m}\Omega$, $C_{\frac{di}{dt}} = 160\text{A}$
L_{in}	5mH	$R_{Lin} = 18.6\text{m}\Omega$, $I_{max} = 75\text{A}$

Table 5.2: Experimental Component Values

resistance from the input inductor to D_{rect} .

5.2 Switching Scheme

During preliminary operation of the converter, an oscillation in the resonant capacitor voltage during zero voltage States 4 and 8 was encountered, as shown in Figure 5.3.

Switch	Manufacturer Number	Voltage Rating	Current Rating	Properties
D_{rect}	DSDI 60-16A	1600V	$63A_{avg}$	$V_{Ftyp} = 2.6V$
S1 / S2	FS100R17KE3	1700V	$100A_{avg}$	$V_{Ftyp} = 0.94V, R_{sw} = 15m\Omega$
D1 / D2	FS100R17KE3	1700V	$100A_{avg}$	$V_{Ftyp} = 1.1V, R_{sw} = 11.6m\Omega$

Table 5.3: Switching Components used in Experiment

This phenomenon occurred while a switching scheme with a 50% duty cycle and negative deadtime was utilized, as detailed in Section 2.3.

The resonant inductor current, $i_{Lv}(t)$ and input inductor current, $i_{in}(t)$, in State 4 are analyzed to understand the reason for the oscillations. Figure 5.5 depicts the currents in this situation. During States 4, $i_{Lv}(t)$, is circulating through the switches and slowly dissipating. Meanwhile, $i_{in}(t)$, is increasing at a constant rate, storing energy for the next period. At higher power, State 4 increase in duration, and the two currents eventually coincide. When this occurs, D2 turns “off” and the reverse recovery charge of D2 creates the oscillations as shown in Figure 5.3.

The oscillations can be removed by activating all four IGBTs during State 4, leading to alternative switching signals shown in Figure 5.6. The result of the alternative switching signals on converter operation is shown in Figure 5.4. With the alternative switching scheme, when $i_{in}(t)$ exceeds $i_{Lv}(t)$, the difference between $i_{in}(t)$ and $i_{Lv}(t)$ has an alternative conduction path through S2, and D2 has a source to provide the reverse recovery charge. The alternative PWM scheme also leads to an improvement in converter efficiency. Figure 5.7 compares efficiency curves of the two different switching schemes.

5.3 Experiment Results

This section examines the measured waveforms and compares them to the expected waveforms used in analysis. Efficiency curves are presented in this section, but show a discrepancy between theoretical and experimental curves. This difference is examined

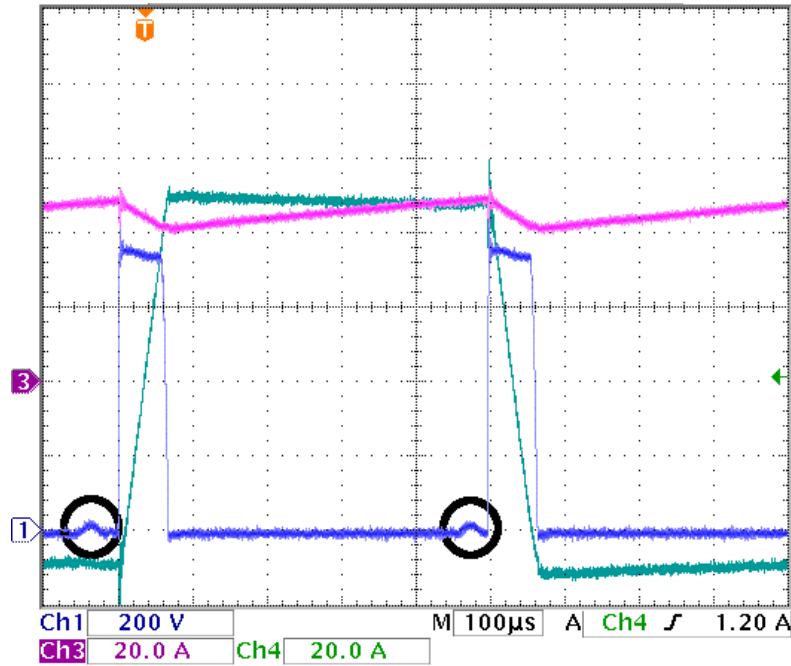


Figure 5.3: Waveforms of $i_{Lv}(t)$, $v_{Cv}(t)$, and $i_{in}(t)$ with Regular PWM Scheme. $v_{Cv}(t)$ is shown in Ch1. $i_{in}(t)$ is shown in Ch3. $i_{Lv}(t)$ is shown in Ch4.

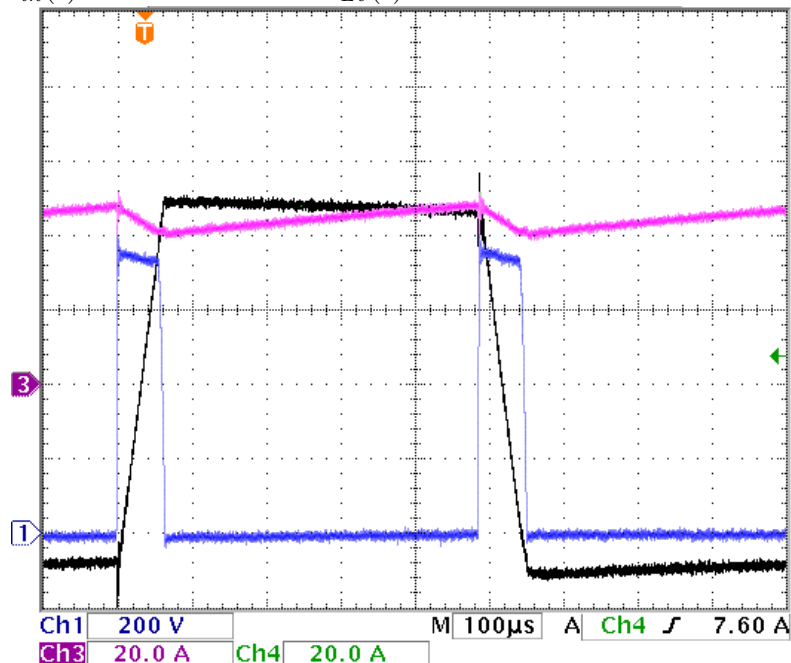


Figure 5.4: Waveforms of $i_{Lv}(t)$, $v_{Cv}(t)$, and $i_{in}(t)$ with Alternate PWM Scheme. $v_{Cv}(t)$ is shown in Ch1. $i_{in}(t)$ is shown in Ch3. $i_{Lv}(t)$ is shown in Ch4.

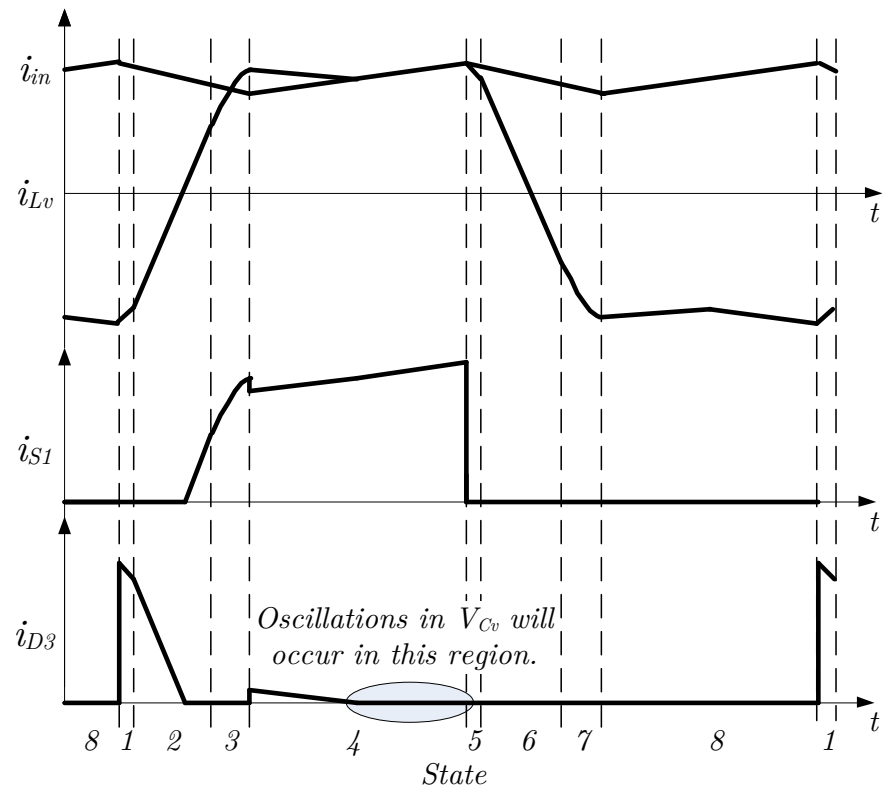


Figure 5.5: Switch current waveform when oscillations occur.

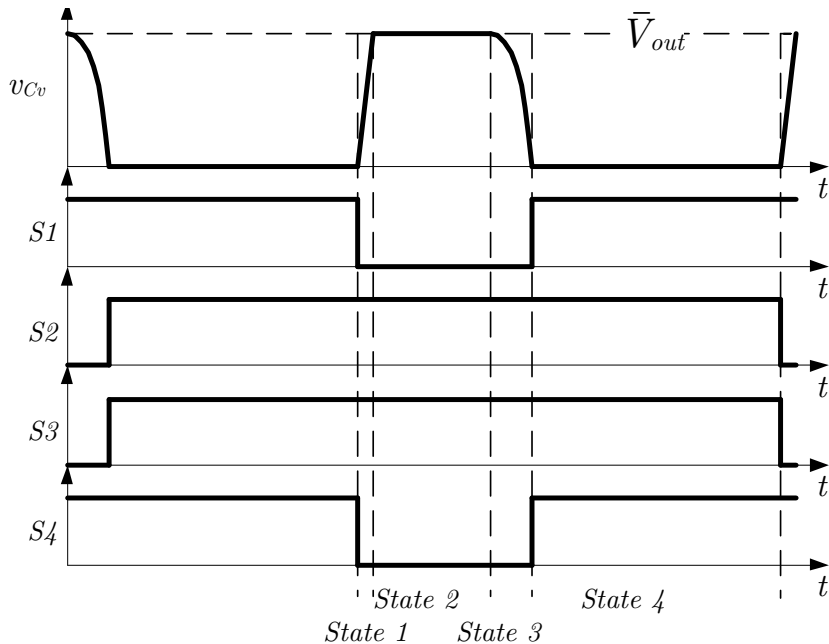


Figure 5.6: Alternative Switching Waveform

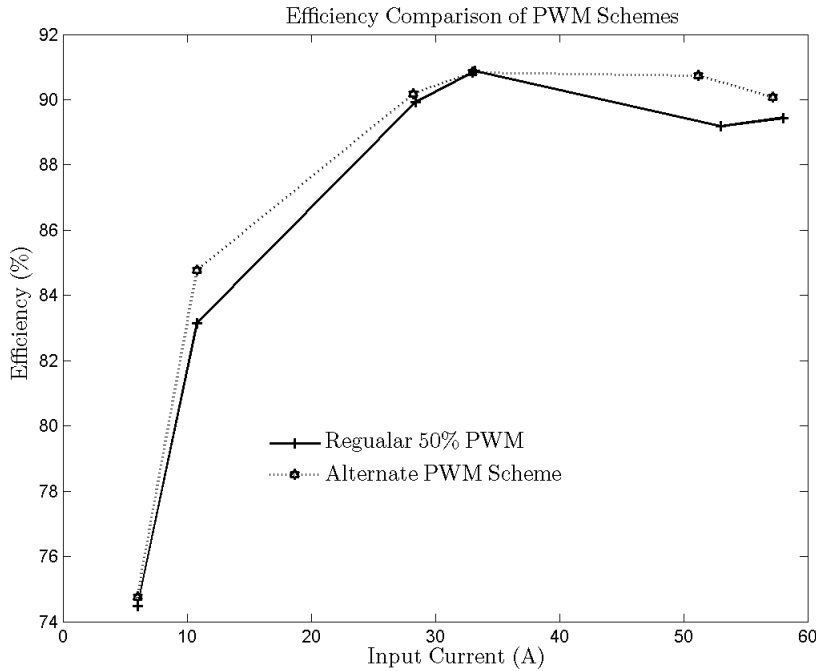


Figure 5.7: Efficiency Curve comparing the two PWM Schemes while the converter is operating with a $V_{in}:V_{out}$ of 120V:1200V

and improvements are suggested and validated.

5.3.1 Waveform Verification

Analysis of the converter's experimental operation was performed while it operated with a \bar{V}_{in} of 96.8V and \bar{V}_{out} of 968V, and delivered 2.14kW.

Waveform Analysis

A comparison of the ideal and actual waveforms found in the experimental setup can be performed. Experimental waveforms are shown in Figures 5.8, 5.9, and 5.10. The first figure shows the waveforms of the input inductor current, resonant inductor current, and resonant capacitor voltage over multiple periods. Figure 5.9 shows a single period and Figure 5.10 is a close up of States 1 to 3. The resonant inductor current, $i_{Lv}(t)$, and resonant capacitor voltage, $v_{Cv}(t)$ is measured at the beginning of each state and

compared to their theoretical value in Table 5.5 while the duration of each state is measured and presented in Table 5.4.

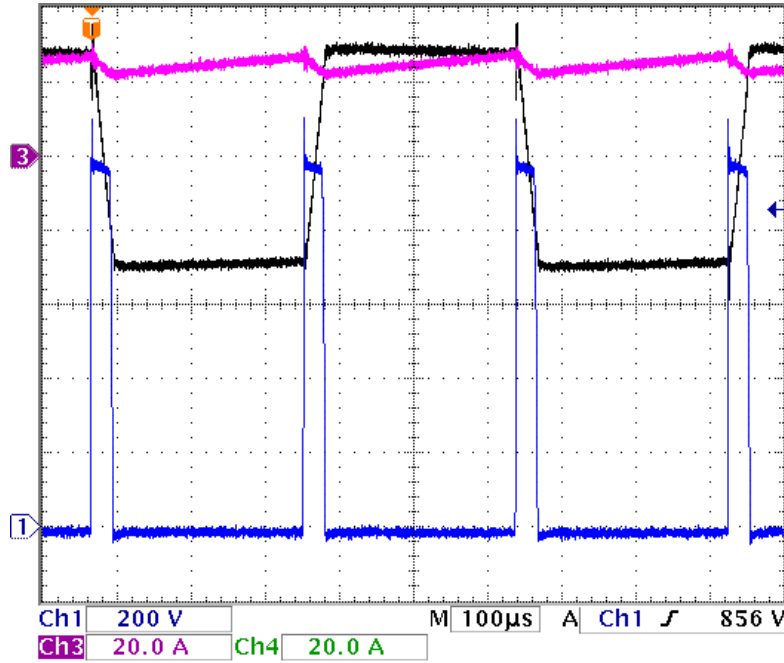


Figure 5.8: Waveforms of $i_{Lv}(t)$, $v_{Cv}(t)$, and $i_{in}(t)$ shown over multiple switching periods. Ch1, Ch2, and Ch4 are $v_{Cv}(t)$, $i_{Lv}(t)$ and $i_{in}(t)$ respectively.

State Duration	Analytic Value	Experimental Value
τ_1	$0.42\mu s$	$1.1\mu s$
τ_2	$28.9 \mu s$	$24.5\mu s$
τ_3	$5.6 \mu s$	$5.0\mu s$
τ_4	$541.2 \mu s$	$566.8\mu s$

Table 5.4: Comparison of measured and theoretical durations of each state.

Examining the presented figures, and tables, these waveforms generally match with the theoretical values. However, there are several notable differences between the expected and the actual waveforms that need to be addressed.

1. Measured and Theoretical values for the resonant inductor current, $i_{Lv}(t)$, at the beginning of State 3 differ, as shown in Table 5.5

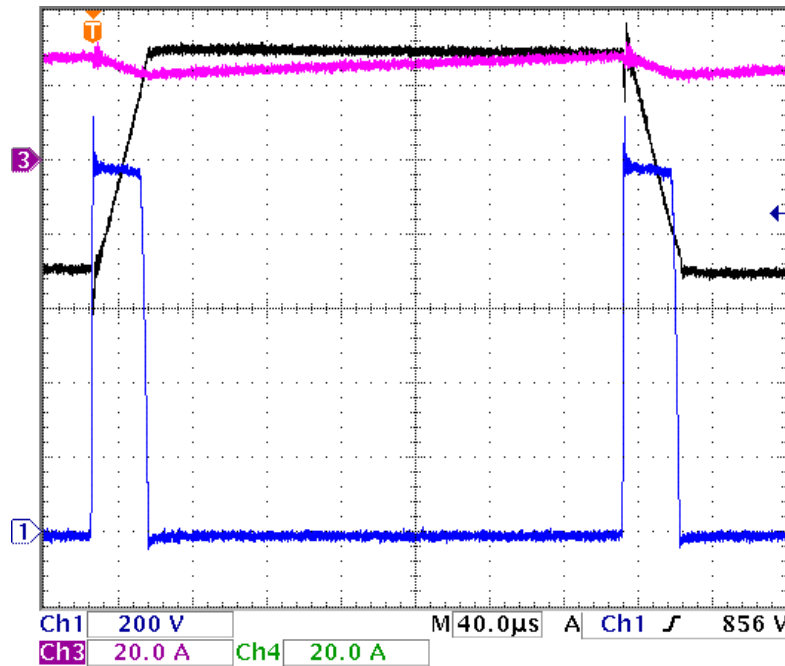


Figure 5.9: Waveforms of $i_{Lv}(t)$, $v_{Cv}(t)$, and $i_{in}(t)$ over a single switching period, but the second charging state, State 8, is omitted. Ch1, Ch2, and Ch3 are $v_{Cv}(t)$, $i_{Lv}(t)$ and $i_{in}(t)$ respectively.

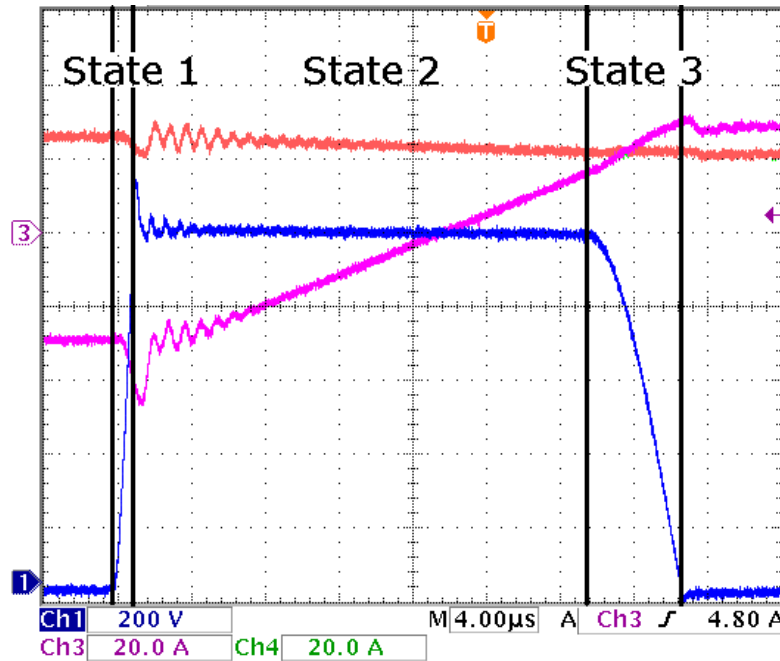


Figure 5.10: Close up of States 1 to 3. Ch1(Bottom), Ch2(Middle), and Ch3(Top) are $v_{Cv}(t)$, $i_{Lv}(t)$ and $i_{in}(t)$ respectively.

Start of	I_{Lv}		I_{in}		V_{Cv}	
	Expected	Measured	Expected	Measured	Expected	Measured
State 1	-31.6A	-28.8A	27.3	27.2A	0V	-16V
State 2	-26.0A	-28.8A	27.3	27.2A	968V	1110V
State 3	22.8A	16.8A	22.3A	22.8A	968V	972V
State 4	-31.6A	28.8A	22.3A	22.4A	0V	-16V

Table 5.5: Comparison of measured and theoretical initial conditions for $i_{Lv}(t)$ and $v_{Cv}(t)$.

2. Measured and Theoretical values differ for the duration of State 1, τ_1 , as shown in Table 5.4
3. Resonant Capacitor Voltage, $v_{Cv}(t)$, overshoots \bar{V}_{out} as apparent in Figure 5.9 and 5.10

The discrepancy between the measured and expected value of $i_{Lv}(t)$ at the beginning of State 3 is discussed first. In Figure 5.10, the waveforms of the converter should transition from State 2 to State 3 when $i_{Lv}(t)$ intersects with the input current, $i_{in}(t)$. When measured, the two waveforms are 6A apart. The main reason is due to the tracking error of the current sensors. With a bandwidth of 100kHz, the expected output of the sensor when tracking the ramp rate of $i_{Lv}(t)$ during State 2 is $i_{Lv}(t) - 3.2A$. At the same time, $i_{in}(t)$ is decreasing at a constant rate, and the sensor would output the signal $i_{in}(t) + 0.3A$. The resulting difference between the actual currents should be at maximum 2.5A, and is attributed to dc offsets in the sensors.

The second issue is that the duration of τ_1 does not match the theoretical value. τ_1 is elongated in the experiment due to the fall time of the IGBT, which is given as $0.18\mu s$ from its datasheet. The length of the fall time is over one third the theoretical duration of State 1, which is $0.41 \mu s$. As a consequence, ZVS is not achieved for the full duration of the IGBT's turn “off”.

Part of the IGBT's turn “off” still occurs under ZVS. Two intervals exist during the IGBT turn “off” transition, the turn “off” delay and the fall time. The turn “off” delay is the time it takes for the collector current of the IGBT to reach 90% of its on state

current after the gate signal is removed. During this period, the majority of the IGBT current does not change. The fall time is defined as the time it takes for the current of the IGBT to fall from 90% to 10%.

For the proposed converter, ZVS is not achieved for the complete turn “off” of the IGBT. However, between the turn “off” delay and fall time, the fall time is the dominant source of switching losses of the two turn “off” intervals. During the turn “off” delay the current conducted by the IGBT does not change much during the delay, and the converter continues to operate as if it is in State 4 or 8. Thus, most of this period of the IGBT turn “off” still achieves ZVS. During the fall time, the current conducted by the IGBT begins to decrease, and $i_{Lv}(t)$ is redirected into C_v . Thereby initiating State 1 or State 5 while the IGBT is still turning “off”, and resulting in switching losses.

The third concern is that the resonant capacitor voltage, $v_{Cv}(t)$, overshoots \bar{V}_{out} . This was previously discussed in Section 2.3, and is expected. $v_{Cv}(t)$ overshoots \bar{V}_{out} because of the forward recovery of the rectifying diode, D_{rect} . Thus, the diode has a hard turn “on”, and causes minor ringing in the circuit.

5.3.2 Efficiency

The efficiency curves of the experimental converter are presented in this section. Shown in Figure 5.11 and 5.12 are the efficiency curves for different conversion ratios. The first figure plots the efficiency against the input current since losses are assumed to be dominated by conduction loss. The second figure plots the efficiency against output current to compare the efficiency curves at equal output power. For these curves, \bar{V}_{out} was set to 1kV, and none of the passive components were changed from curve to curve. As a result, components like the input inductor, L_{in} , and resonant inductor, L_v , are overrated, and the conduction loss is somewhat lower than a properly rated inductor, but core loss is higher. As expected, lower conversion ratios allow for higher efficiency, and the efficiency for this prototype typically peaks around an \bar{I}_{in} of 30A.

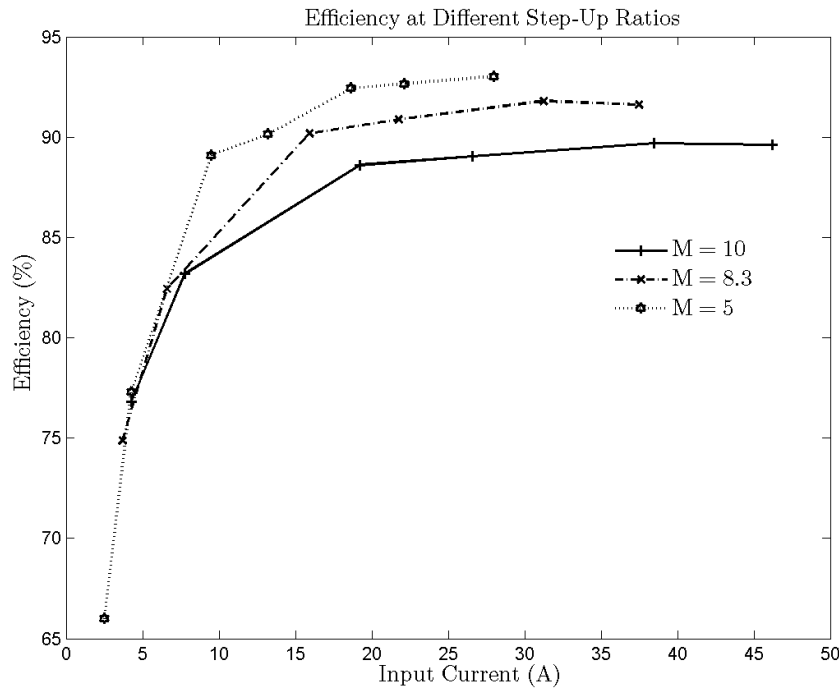


Figure 5.11: Efficiency curves for step-up ratios of 5, 8.3 and 10 plotted against input current.

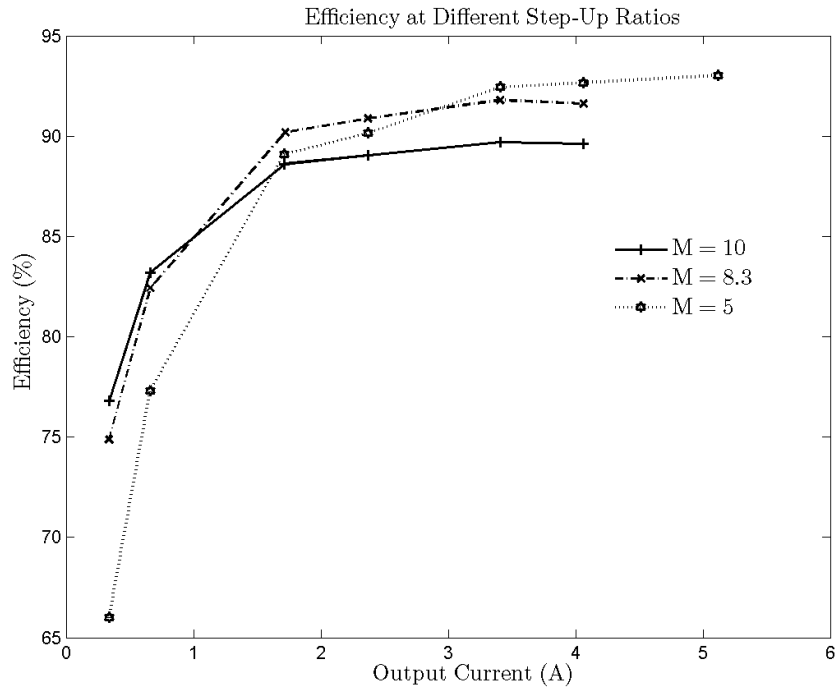


Figure 5.12: Efficiency curves for step-up ratios of 5, 8.3 and 10 plotted against output current.

To compare the theoretical efficiency to the measured efficiency, the converter was operated with an input voltage of 100V at a 1:10 step up ratio using the components of Table 5.2. Figure 5.13 shows resulting theoretical and measured efficiency curves. A difference of 3.5% or greater was measured between the theoretical and experimental curves.

To investigate the losses, the converter was set to deliver 2.37kW with two different parameter sets listed in Table 5.6. The major difference is that parameter set 1 uses a C_v of 25nF and parameter set 2 uses a C_v of 100nF.

Converter Property	Value	
	Parameter Set 1	Parameter Set 2
V_{in}	100V	100V
V_{out}	1kV	1kV
f_{sw}	1.7kHz	1.4kHz
P_{out}	2.37kW	2.37kW
L_{in}	5 mH	5mH
L_v	500 μ H	500 μ H
C_v	25 nF	100 nF

Table 5.6: Converter operating point used to investigate efficiency.

In the theoretical efficiency calculation, the only losses that have been accounted for are conduction losses. The two most plausible sources of loss are core losses in the magnetics, and switching losses. Regarding switching losses, Section 5.3.1 highlighted that the turn “off” of the IGBT would produce loss. Another source of switching loss is the turn “on” sequence for the rectifying diode, D_{rect} .

IGBT Switching Loss

In Section 5.3.1, it was deduced that the IGBT turn “off” caused losses due to the short duration of State 1 compared to the fall time for the IGBT. The current in each IGBT could not be measured to estimate turn “off” loss. Therefore, the duration of State 1 was extended by increasing the resonant capacitor, C_v . The theoretical duration of State 1

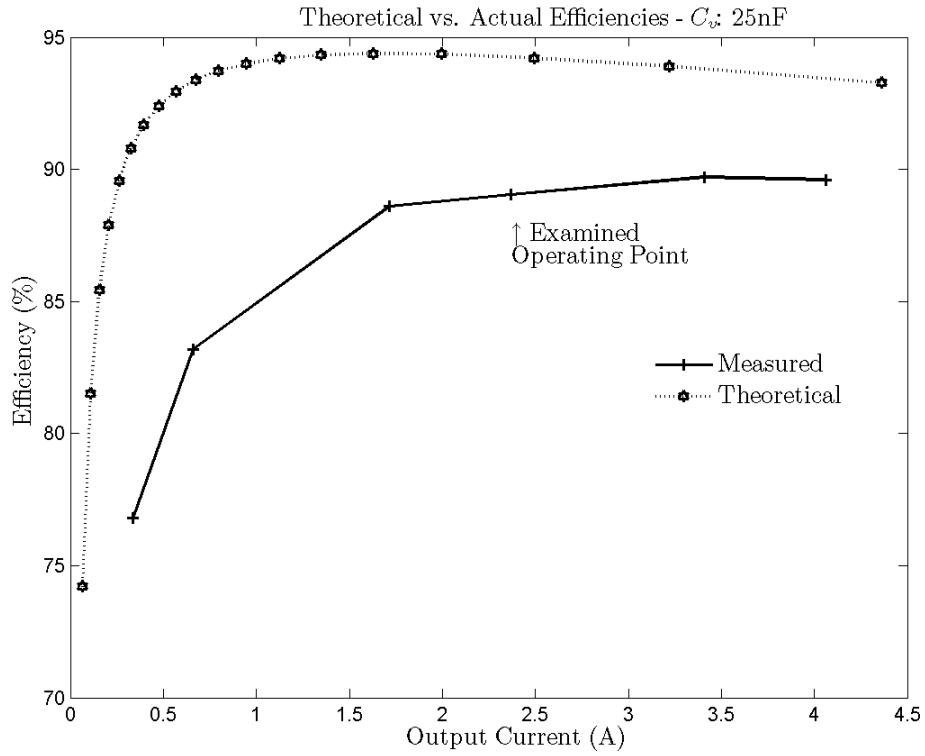


Figure 5.13: Theoretical and Actual Efficiency Curves at a step-up ratio of 10:1.

was lengthened by $1.1\mu\text{s}$ increasing the expected τ_1 from $0.4 \mu\text{s}$ to $1.5 \mu\text{s}$ by changing C_v from 25nF to 100nF .

When tested, the measured duration of State 1 increased from $1.1\mu\text{s}$ to $2.2\mu\text{s}$. The duration still does not match the theoretical value, but it did increase by $1.1\mu\text{s}$, which matches the expected change in τ_1 . Efficiency was found to increase despite increased resonant inductor conduction losses that resulted from the change in C_v . Figure 5.14 shows the experimental efficiency for the two values of C_v .

The efficiency of the operating point under analysis is shown to improve by nearly a percent, even though its expected efficiency has been reduced, as can be seen by comparing Figure 5.15 and 5.13. Figure 5.15 also shows better agreement between the theoretical and experimental efficiency curves than Figure 5.13.

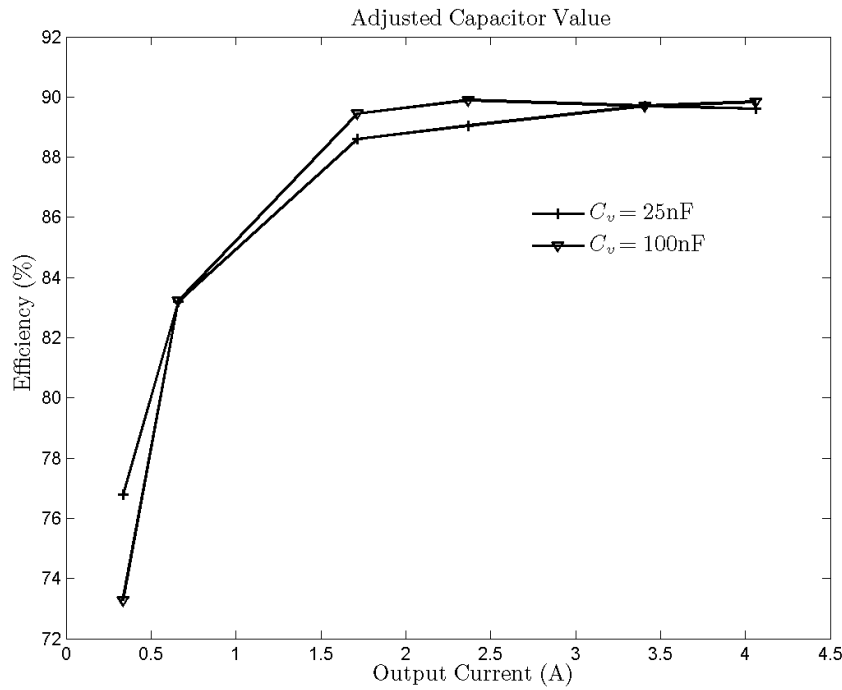


Figure 5.14: These curves compare the two different efficiencies achieved with a C_v of 25nF and 100nF

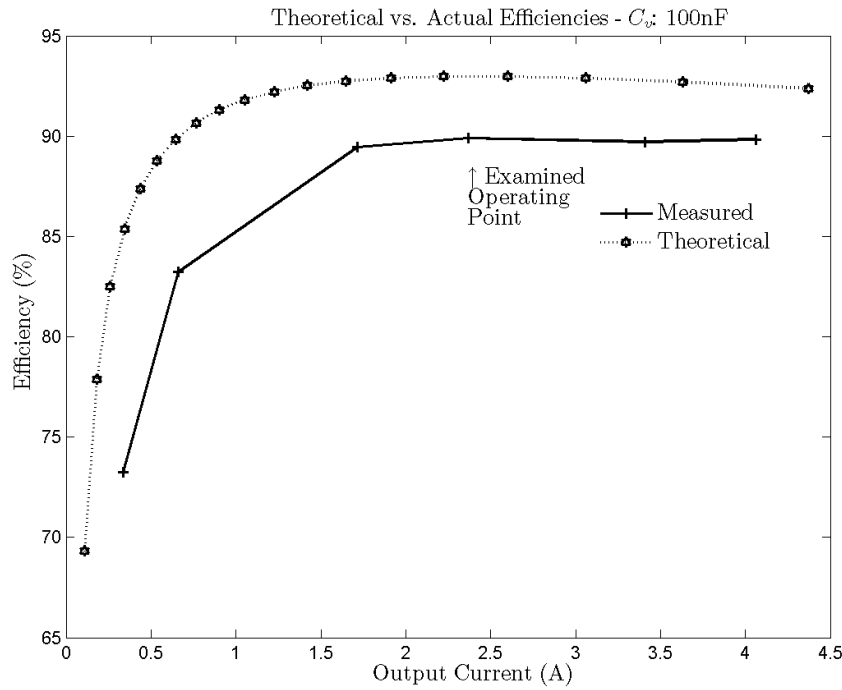


Figure 5.15: Theoretical and Actual Efficiency Curves for $C_v = 100nF$ with a step-up ratio of 1:10.

Diode Switching Loss

The rectifying turn “on” loss is not unique to this converter, thus the calculation method has been placed in Appendix C. The rectifying diode turn “on” loss was found by assuming the diode was fully conducting by the peak of the voltage overshoot. The calculated loss of the rectifying diode turn on was 3.4W for the converter with C_v of 100nF. This represents only 0.1% loss at the investigated operating point.

Magnetic Loss

The magnetic loss had to be found experimentally due to lack of information. Loss was found by recording temperature rise and is detailed in Appendix B. The resonant inductor’s loss was not significant enough to measure, but the input inductor’s core loss is estimated to be 40.9W and represents a loss of 1.6% for the converter with C_v of 100nF.

Power Loss Summary

A summary of power loss is presented in Table 5.7. This breakdown is for the converter operating with a C_v of 100nF as specified in Table 5.6.

	Power (W)	Percentage of P_{in}
P_{out}	2366.8 W	89.92%
IGBT Conduction Loss	116.8 W	4.44%
IGBT - Diode Conduction Loss	19.9 W	0.76%
Rectifying Diode Turn-on Loss	4.9 W	0.13%
Rectifying Diode Conduction Loss	7.4 W	0.28%
C_v Conduction Loss	0.1 W	Negligible
C_{out} Conduction Loss	5.8 W	0.22 %
L_{in} Conduction Loss	13.0 W	0.49%
L_v Conduction Loss	22.0 W	0.84%
L_{in} Core Loss	40.9 W	1.56%
Unaccounted Loss	34.4 W	1.37%

Table 5.7: Breakdown of Power for Operating Point indicated in Figure 5.15 for P_{in} of 2632.0 W.

Unaccounted losses could be attributed to many different sources like the core losses

from L_v , unaccounted core loss from L_{in} , inductive heating of metal surrounding the converter, and unaccounted switching losses, which were reduced but not eliminated by increasing C_v .

5.4 Summary and Comparison

From the experimental setup, the analysis has been verified and efficiency curves have been measured. For a step up ratio of 1:10, a peak efficiency of 89.9% is achieved. From the experimental setup, an additional constraint on the length of State 1 is required to reduce switching losses at the IGBT turn “off”, which roughly proportional to C_v .

5.4.1 Boost Comparison

The current-based resonant converter can be compared to an equivalent medium voltage boost converter using 6.5kV IGBTs from Infineon. The converters are to operate at an input voltage of 360V at a 1 to 10 step-up, and maximum input current of 625A. Switching losses of the boost converter are included in the efficiency estimate, with a relatively low switching frequency of 1kHz selected to constrain switching losses [9]. The inductor is sized for 20% ripple and the sizing of the parasitic resistance for the inductor is based on the $\frac{L}{R}$ ratio of the input inductor used in the experimental setup.

The current-based resonant converter was assumed to operate without switching loss, and τ_1 was chosen to be approximately 5x larger than the IGBT fall time when the converter is operated at full load to satisfy this assumption. This constraint is based on the experimental sizing of C_v in Section 5.3.2.

For the current-based resonant converter. The ripple on the input current is set by the relative size of L_{in} and L_v . Since a minimum ratio of 10:1 between L_{in} and L_v is required, an input ripple from average to peak of approximately 10% results. The parasitic resistances of the inductors are based on the $\frac{L}{R}$ ratios of the inductors used in

the experimental setup.

Component sizes, and details on the efficiency calculation can be found in Appendix D. The efficiency curve comparison between the boost converter and current-based resonant converter is shown in Figure 5.16

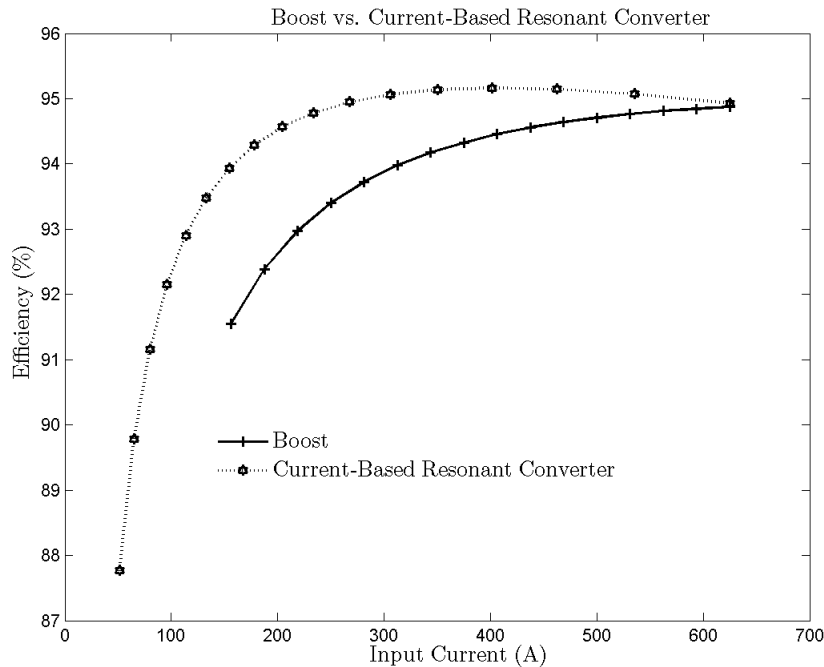


Figure 5.16: Comparison of Theoretical Efficiency between Boost Converter and Current-Based Resonant Converter

Figure 5.16 shows the proposed converter is able to outperform a standard boost topology. However, magnetic and switching losses of the current based resonant converter have not been included due to the lack of core material information and access to individual switches. Magnetic losses of the proposed converter would also apply to the boost converter. Switching loss for the IGBT fall time are not included, but switching losses for the boost converter are also a conservative estimate based upon a switch temperature of $25^{\circ}C$. Therefore, the current-based resonant converter is expected to outperform an equivalent boost converter.

5.4.2 Voltage-Based Resonant Converter Comparison

The comparison between the current-based resonant converter and the voltage-based resonant converter of [1] should also be performed. The experimental system specifications used in [1] are presented in Table 5.8, and specifications for the current-based resonant converter used for comparison are presented in Table 5.9. Figure 5.17 shows the comparison of the efficiency curves of the two converter types. The efficiency curves show that the voltage-based resonant converter has a more consistent efficiency across the load range, while the current-based resonant converter is able to achieve higher efficiencies at higher loads.

V_{in}	115V
V_{out}	620V
L_{res}	500 μ H
C_{res}	10 μ F
Input Power	5kW

Table 5.8: Converter Specifications from [1]

V_{in}	200V
V_{out}	1000V
L_{in}	5mH
L_v	500 μ H
C_v	25nF

Table 5.9: Current-Based Resonant Converter Component Values and Operating Point for Comparison to [1]

The efficiency of the voltage-based resonant converter is limited by its switching component. It requires voltage bidirectional two-quadrant switches, where an IGBT and diode are used in series. Thyristors can be used for the voltage-based resonant converter, however the maximum switching frequency will be limited by the thyristor turn “off” time, and larger resonant components would be required. In contrast, the current-based resonant converter is able to better utilize the V-I characteristics of IGBTs. The current-

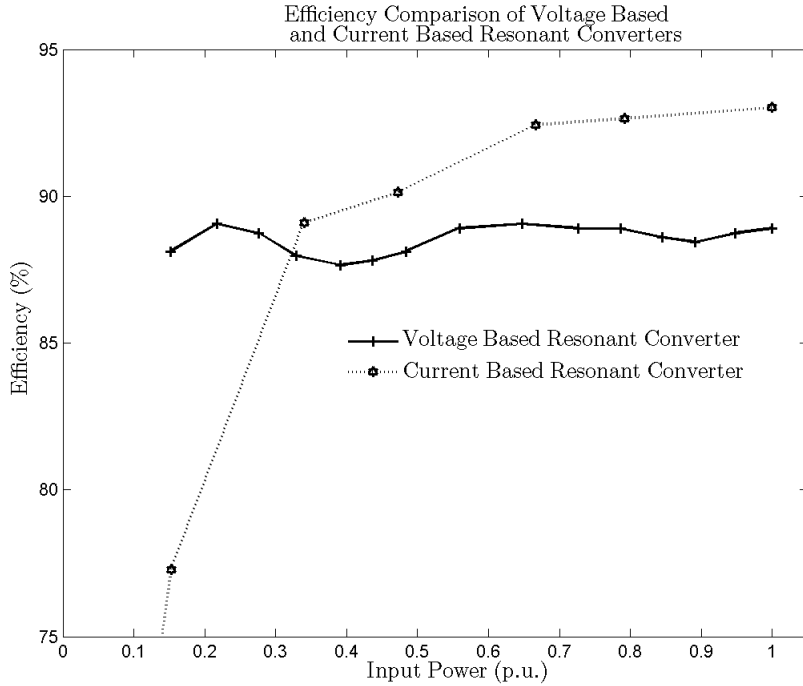


Figure 5.17: Comparison of Theoretical Efficiency between Voltage-Based and Current-Based Resonant Converter

based resonant converter also utilizes smaller component sizes, but requires an additional input inductor. However, this input inductor is only required to handle DC currents allowing its cost and size to be optimized.

An important quality of [1] is that it is potentially a modular converter. Voltage capabilities can be increased by simply adding additional switching modules, and [1] shows that static voltage sharing is possible. However, during the switching instances, the transient voltage across each module may exceed the switch's rating, and further research is required.

For the current-based resonant converter, additional switching modules could be added, but the parasitic inductance between the modules and the rectifying diode would increase.

Using two switching modules in series allows a limited increase in the parasitic inductance. Simulation shows equal voltage balancing is achievable with ideal components.

Component mismatch, parasitic capacitance of IGBTs, and switching signal delays cause oscillations in the voltage across the modules, but the oscillations appear to be bounded for a two module converter. Appendix E details the preliminary simulations. The multi-module version of the current-based resonant converter shows promise in sharing voltage between modules without the need for active voltage balancing techniques, however preliminary analysis shows that parasitic inductance will severely limit the number of series modules.

The switching module of the voltage-based resonant converter was developed into a family of converters in [1]. Considering the waveforms and preliminary investigations of the current-based resonant converter, an equivalent step-down topology equivalent to a buck converter can be developed, and it is presumed that an equivalent current-based family of converters exists.

5.4.3 Limitations

The current-based resonant converter is a topology that can utilize IGBT technology, allowing for faster switching frequencies and smaller tank components. From the comparisons, and experimental setup, additional design constraints can be added to those developed in Section 4.5. These additional constraints are based on the assumption that inductor resistance scales with inductor size. All the constraints or limitations are listed as follows:

1. The ratio of the resonant inductor, L_v , to input inductor, L_{in} , is used to satisfy input ripple constraint and maintain the constant input current assumption.
2. IGBT turn “off” losses can be reduced by choosing an appropriate duration, τ_1 , for State 1. τ_1 can be set using the resonant capacitor, C_v , which is roughly proportional to τ_1 . However, a larger C_v would also result in higher conduction losses.

3. The ratio of C_v to L_v is used to minimize conduction loss by reducing the resonant current, I_{res} . However, increasing L_v and L_{in} may reduce efficiency by increasing parasitic resistance.
4. The size of L_v is used to either set the frequency of operation or to set I_{res} for a given C_v .
5. C_v is limited by $\frac{dv}{dt}$ rating and not the RMS current rating.

Chapter 6

Conclusion

This research identified a need for efficient high voltage high step-up converters to interconnect DC power systems. To address this problem, a transformerless high step-up DC/DC converter was presented in this work. The proposed converter is based on [1], and was referred to as a current-based resonant converter within this work.

The steady state and dynamic models for the proposed converter were presented and verified against a PSCAD/EMTDC simulation. The analytic models were shown to well approximate the simulation. From the dynamic model, a method of control was developed to manage the nonlinear aspects of the model, and simulation was used for verification.

A refinement to the analytic model was made to improve upon the solution found through energy balance and was shown to better capture the actual current stresses of the components. The proposed system was realized as a 100V:1kV/4kW experimental setup. The experimental waveforms and losses were analyzed to better understand the limitations of the converter.

In comparison to [1], the proposed converter was found to better utilize the V-I characteristics of IGBT technology, and would be able to operate at higher switching frequencies and reduce component size. The current-based resonant converter was shown

to outperform the voltage-based resonant converter in efficiency at higher loads. The proposed converter was also compared to a boost converter and was shown to provide higher efficiency over the operating range. Based on these comparisons, the current-based resonant converter shows promise to operate at high voltage and high gain as a DC interconnect.

6.1 Future Work

Future work is focused on expanding the capabilities of the proposed converter, and assessing it for use as a DC interconnect.

1. Verify control methodology with a lab setup.
2. Investigate the two module extension of this topology. Preliminary simulations show voltage sharing is possible, even with non-idealities.
3. Reference [1] developed a family of converters. The same idea can be applied to the current-based resonant converter to develop step-down and bidirectional converters.
4. Investigate fault propagation with the family of converters, and its operation as a node of a DC system.

Appendices

Appendix A

Compensator and Current Filter Design

In this appendix, the design of the current filter and compensator used in Section 3.2 is detailed. The current filter is used to filter the ripple of $i_{in}(t)$ for feedback, and a first order low-pass filter is used. The pole of the filter was selected to filter the ripple at the lowest operating frequency. For a converter with the properties of Table 3.2 and maximum \bar{I}_{in} of 50A, the minimum operating frequency is 876Hz. While the minimum switching frequency is 876Hz, the ripple has a frequency that is two times larger because power is delivered twice during a single switching period. As a result, the pole of the filter is chosen as 400Hz to filter a ripple of approximately 1.8kHz.

The compensator design was performed with the analytic model. The converter parameters of Table 3.2 were used with the current filter's pole was placed at 400Hz as discussed. A PI controller was chosen for use with gains K_p and K_i to achieve a phase margin of 70° . The compensator values of K_p , and K_i were chosen to be -1.5 and -94.25 respectively. These values are negative because the plant contains a negative itself, and negative feedback requires the gains be negative. The resulting bode plot of the Loop gain is shown in Figure A.1.

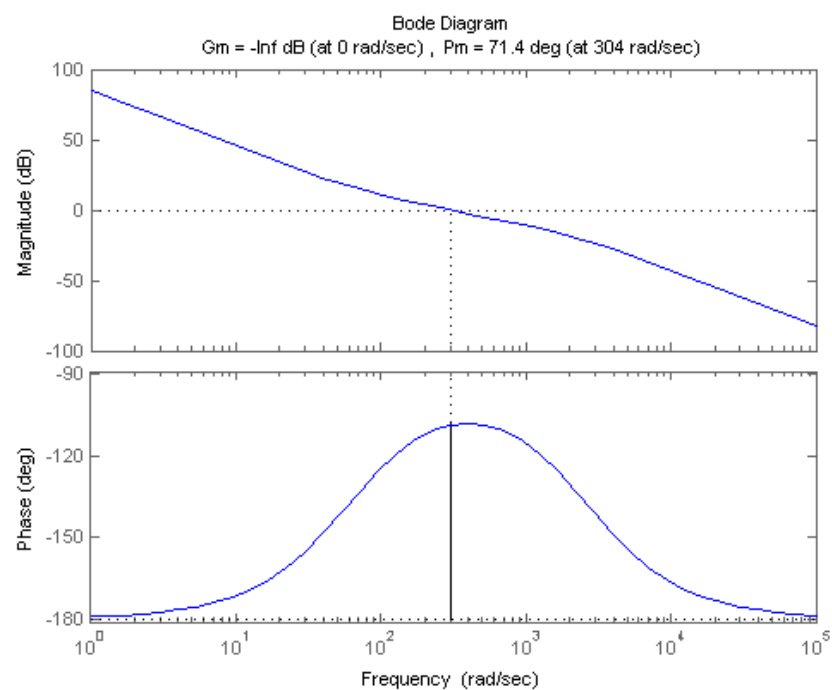


Figure A.1: Bode Plot of Loop

Appendix B

Magnetic Loss Measurement

Magnetic losses for the two inductors were found by recording temperature rise at various points on the inductors as indicated in Figure B. Specifications for both inductors are shown in Table B.1. The temperature values were measured in 15 minute intervals after the first hour and are given in Table B.2.

At the start of the test, it was suspected that L_v would be the main source of loss, and the starting temperature was not recorded for L_{in} . It was then assumed that L_{in} started at ambient, similar to the rest of the system.

Inductor	Value	I_{rated}	Manufacturer / Part Number	Type	Weight
L_{in}	5000 μ H	75A	Hammond 195G75	DC	45.4kg
L_v	500 μ H	100A _{rms}	Custom - In Lab	High Freq.	27.2kg

Table B.1: Inductor Specifications

Time (min.)	L_v ($^{\circ}C$)						L_{in}	Ambient
	Loc. 1	Loc. 2	Loc. 3	Loc. 4	Loc. 5	Loc. 6		
0	28.2	28.3	28.3	28.1	27.9			27.9
60	37.6	37.8	33.9	33.0	31.6	39.1	37	28.5
75	39.6	40.2	34.6	33.6	32.0	38.4	38.4	28.8
90	40.2	41.0	35.1	34.5	32.3	39.1	40.1	28.9

Table B.2: Temperature of various points on both inductors.

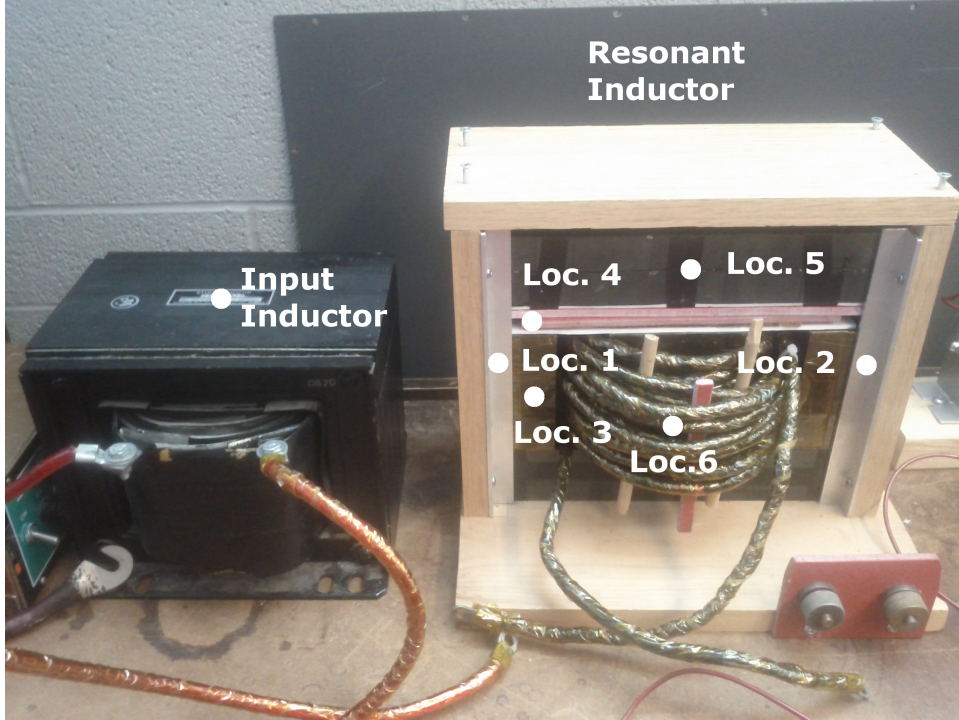


Figure B.1: The different temperature measurement locations for the inductors are indicated here.

From the data it is apparent that core loss in L_v is not significant enough to noticeably heat the inductor. Comparing the temperature of Location 5 to the other measurements on L_v , it is possible that the wiring, Location 6, is heating the surrounding area. Therefore, the measured rise in temperature is likely not caused by core loss in L_v . Of the points measured on L_v , the aluminium bars, Location 1 and 2, rose in temperature by approximately $11.7^\circ C$ in comparison to the final ambient temperature. However, this heating only results in 0.92W of loss through the aluminium.

The temperature of L_{in} increases almost regularly, and rises in temperature by $11.2^\circ C$ compared to the final ambient temperature at the end of the test. The rise in temperature results in 40.9W of loss from the loss of the input inductor. Several approximations were used to calculate the loss. The inductor's weight used in calculation includes the wiring and any other mounting brackets, and the specific heat capacity of the inductor's core material is unknown. The inductor is most likely made from electrical steel, but a specific

heat capacity could not be found.

Using [21] as reference, the specific heat capacity for various types of steel range from 434 $\frac{J}{kgK}$ to 480 $\frac{J}{kgK}$. Thus, a specific heat capacity of 434 $\frac{J}{kgK}$ was used to estimate the core loss.

Appendix C

Rectifying Diode Loss

The rectifying diode turn “on” loss can be measured by using the voltage across the rectifying diode, which is shown in Figure C.1. Figure C.1 is the diode voltage for operating parameter set 1 of Table C.1. The figure also shows the assumed current that passes through the rectifying diode for this loss calculation.

The duration of the voltage overshoot is measured as 440ns, and the diode voltage reaches a peak value of 112V from the zero crossing in 160ns. Using a theoretical value for the current at the beginning of State 2, it was assumed that the diode current reaches a maximum of 59.8A at turn “on”, calculated by using Equation 4.2.9. For the diode turn “on” loss calculation, the current is assumed to stay constant once the diode is fully turned “on”, as indicated in Figure C.1. From these assumptions, the diode turn “on” loss for operating parameter set 1 is calculated to be 4.4W.

The rectifying diode loss can also be calculated for operating parameter set 2 assuming that the overshoot duration does not change. The overshoot voltage is measured to be 96V, and peak diode current is calculated with Equation 4.2.9 to be 65.4A. From this information, the rectifying diode loss for operating parameter set 2 is estimated to be 3.4W.

Converter Property	Value	
	Operating Parameter Set 1	Operating Parameter Set 2
V_{in}	100V	100V
V_{out}	1kV	1kV
f_{sw}	1.7kHz	1.4kHz
\bar{I}_{in}	26.6A	26.4A
P_{out}	2.37kW	2.37kW
L_{in}	5 mH	5mH
L_v	500 μ H	500 μ H
C_v	0.025 μ F	0.100 μ F

Table C.1: Converter operating point used to investigate efficiency.

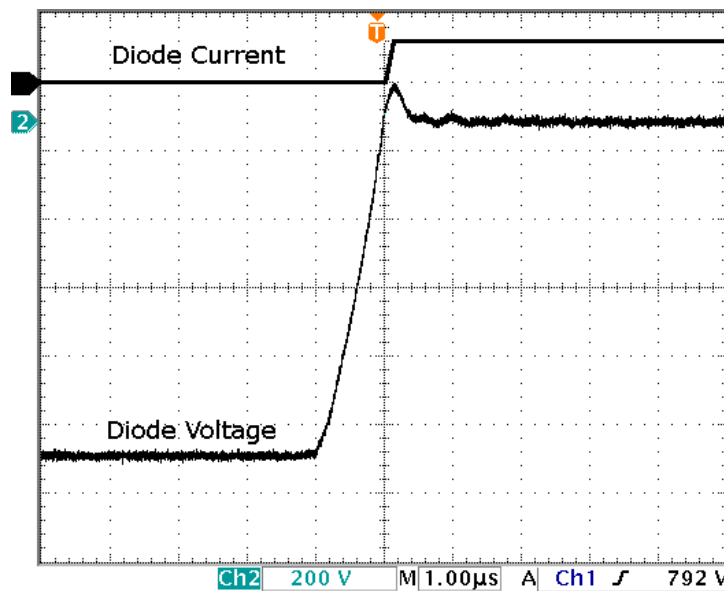


Figure C.1: Voltage across the rectifying diode with the assumed current in the diode.

Appendix D

Boost & Current-Based Resonant Converter Efficiency

This appendix covers the efficiency calculation, and presents the component choices for the current-based resonant converter and the boost converter comparison. Design of the current-based resonant converter is covered first, and is followed by the boost converter design. Both converters have an input and output voltage of 360V and 3.6kV respectively. 3.6kV was chosen such that the calculated values for energy loss per switching instance could be used from the datasheet. Both converters use the same IGBT data, which is displayed in Table D.1. Parasitic resistances of passive components were estimated by maintaining $\frac{L}{R}$ and $\frac{1}{CR}$ ratios from the experimental setup. The components used in the experiment are repeated in Table D.2 for convenience.

Switch	Manufacturer Number	Voltage Rating	Current Rating	Properties
Rectifier Active Switch	DD750S65K3T	6500V	750A	$V_{Ftyp} = 3V$ at $25^{\circ}C$
Active Switch Diode	FZ750R65KE3	6500V	750A	$V_{Ftyp} = 3V$ at $25^{\circ}C$
	FZ750R65KE3	6500V	750A	$V_{Ftyp} = 3V$ at $25^{\circ}C$

Table D.1: Switching components used in comparison of Boost and Current-Based Resonant Converter.

Converter Component	Value	Parasitic Resistance	$\frac{X}{R}$ at 60 Hz
L_v	500 μH	$R_{Lv} = 13.37\text{m}\Omega$	14
C_v	0.025 μF	$R_{Cesr} = 37.6\text{m}\Omega$	2.8e6
L_{in}	5mH	$R_{Lin} = 18.6\text{m}\Omega$	101

Table D.2: Experimental Component Properties

D.1 Current-Based Resonant Converter

The loss calculation for the resonant converter is calculated with the method described in Section 4.4, and only accounts for conduction losses. Components were chosen iteratively, with the input inductor, L_{in} , constrained to be 10x larger than the resonant inductor, L_v . L_v was used to set the resonant current, I_{res} such that S1 and S2 would conduct the switch's rated current during the input inductor charging states, State 4 and State 8.

To achieve low switching losses, the resonant capacitor, C_v , was used to constrain the duration , τ_1 , of State 1. τ_1 was set to be 5x larger than the fall time of the IGBT when the converter is operating at rated input current. Therefore, τ_1 is restricted to be at least $2\mu\text{s}$ in duration for the selected IGBTs. The resulting component values are shown in Table D.3

Converter Quantity	Value
I_{in}	625A
$\Delta i_{in_{avg-pk}}$	66.6 A
I_{res}	250A
L_{in}	1.7mH
L_v	170 μH
C_v	0.82 μF
R_{Lin}	4.5 m Ω
R_{Lv}	4.5 m Ω
R_{Cesr}	1.1 m Ω
τ_1	$2.0\mu\text{s}$
f_{sw} Min.	655 Hz
η_{Res} at $I_{in_{rated}}$	94.9%

Table D.3: Current-Based Resonant Converter Component Properties and Operating Point

D.2 Boost Converter

The efficiency of the boost converter was calculated by including conduction and switching losses. For conduction losses, the efficiency can be calculated with

$$\eta_{Conduction} = \left(1 - \frac{V_f}{V_{in}}\right) \left(\frac{1}{1 + \frac{R_L}{R_{Load}(1-D)^2}} \right) \quad (\text{D.2.1})$$

Switch conduction loss is accounted for in the first term where V_f is the voltage drop due to the IGBT and diode since they have identical V_f and one is conducting at all times. The second term is due to the conduction losses of the inductor parasitic resistance.

Switching losses from the IGBT and output diode were both included in efficiency calculations. IGBT turn “on” and turn “off” losses were calculated using Equation D.2.2, and D.2.3 respectively. The IGBT switching losses were assumed to scale with the input current. Thus, the maximum switch current, \bar{I}_{swMAX} , is used to normalize the turn “on” and turn “off” energy. The input current ripple also affects the amount of current the IGBT conducts during switch transitions, therefore the ripple, ΔI_{in} is included in the switching loss estimate. The diode reverse recovery loss was included by using Equation D.2.4.

The energy lost during the turn “on”, $E_{IGBTturn-on}$, and turn “off”, $E_{IGBTturn-off}$, transitions were found from the IGBT’s datasheet, and is provided in Table D.4. The reverse recovery charge, Q_{rr} , of the diode is also included in Table D.4.

Switching Losses	Value
$E_{IGBTturn-on}$	4.2J at 25°C and V_{CE} of 3.6kV
$E_{IGBTturn-off}$	3.6J at 25°C and V_{CE} of 3.6kV
Q_{rr}	850 μ C at 25°C

Table D.4: Switching losses for switches used in comparison.

$$P_{LossTurn^{on}} = f_{sw} \frac{E_{IGBTturn-on}}{\bar{I}_{swMAX}} (\bar{I}_{in} - \Delta \bar{I}_{in}) \quad (D.2.2)$$

$$P_{LossTurn^{off}} = f_{sw} \frac{E_{IGBTturn-off}}{\bar{I}_{swMAX}} (\bar{I}_{in} + \Delta \bar{I}_{in}) \quad (D.2.3)$$

$$P_{LossQ_{rr}} = f_{sw} Q_{rr} \bar{V}_{out} \quad (D.2.4)$$

The component parameters and the operating point at rated output power is summarized in Table D.5.

Converter Quantity	value
$I_{in_{rated}}$	625 A
ΔI_{in}	125 A
L_{Boost}	1.3 mH
R_{LBoost}	4.8 mΩ
D	0.9
f	1 kHz
η_{Boost} at $I_{in_{rated}}$	94.9%

Table D.5: Boost Converter Component Properties and Operating Point

Appendix E

Current-Based Resonant Converter: Voltage Sharing

This appendix details the preliminary investigation for the two module current-based resonant converter. The circuit diagram of the two module converter is shown in Figure E.1. For this investigation, the converter was simulated with the operating point and components listed in Table E.1.

Two cases were simulated for the converter. One simulation compares the voltage sharing of the modules due to mismatch in resonant inductors, and the second simulation added parasitic capacitance of the switches, and delayed gating signals in addition to the mismatch in resonant inductors. For an output voltage of 2kV, V_{m1} and V_{m2} should ideally have a maximum value of 1kV.

Results of first simulation case with the mismatch between L_{v1} and L_{v2} are shown in Figure E.2. The two modules are shown to provide a mismatch in voltage sharing, but does not differ significantly from the expected value.

The result of the second simulation case is presented in Figure E.3. This simulation adds parasitic capacitances of 0.5 nF across each IGBT, and a gate delay of 0.4 μ s between switching module 1 and switching module 2. This means that S1 of switching module 1

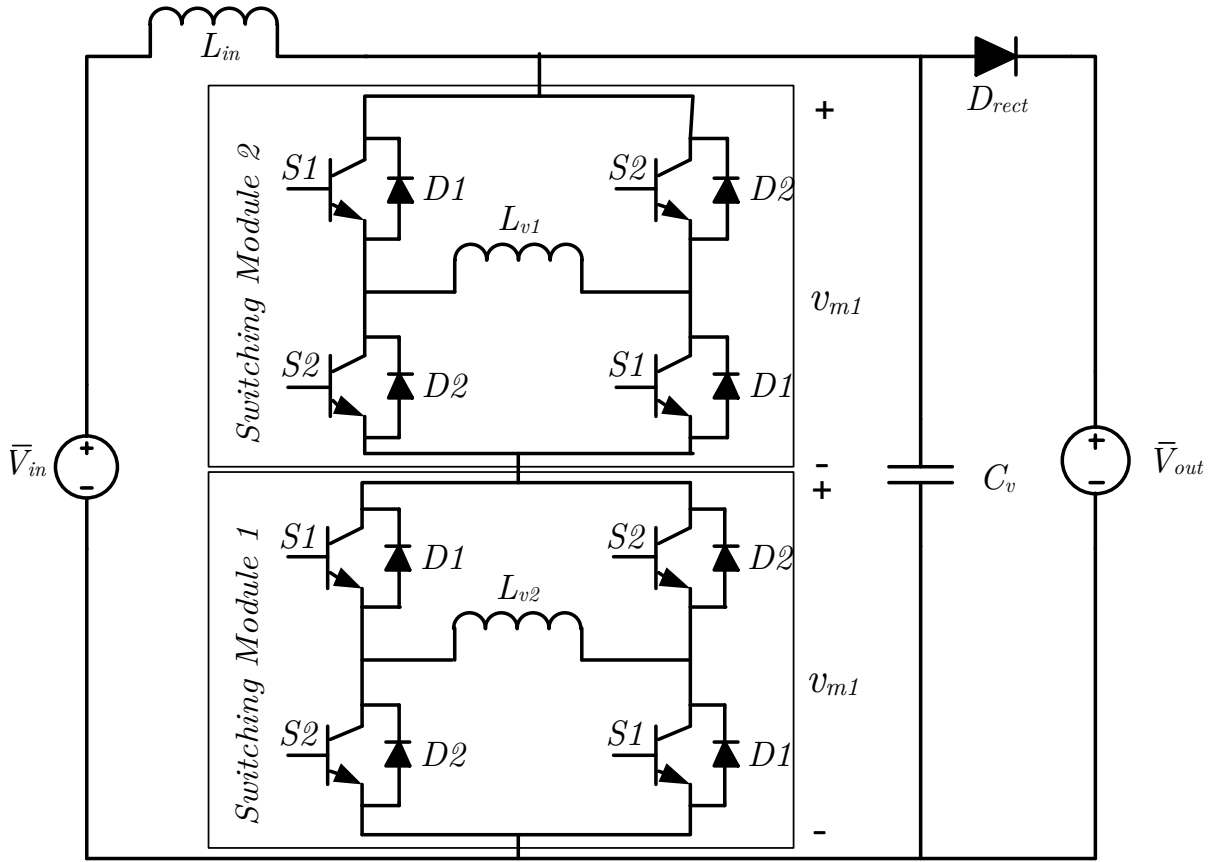


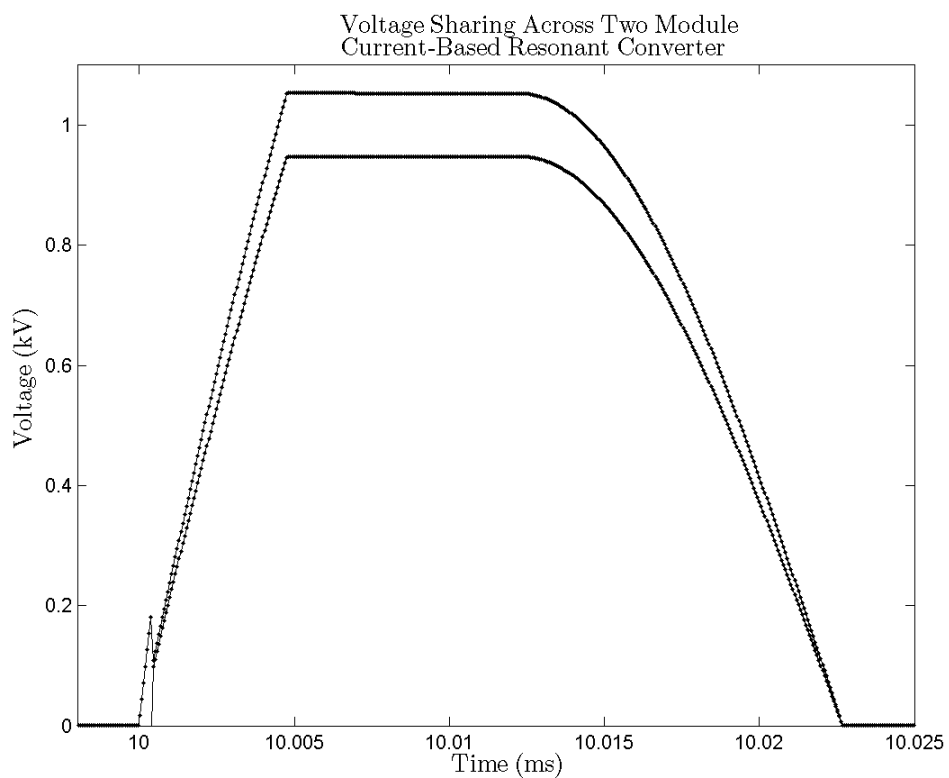
Figure E.1: Two module version of the Current-Based Resonant Converter

is gated $0.4\mu\text{s}$ later than $S1$ of switching module 2.

The addition of both non-idealities results in oscillations superimposed on the voltage waveforms of Figure E.2. These oscillations are caused by the resonant inductors oscillating with the parasitic capacitance of the switches, and appear to be bounded. Therefore, the oscillations would not prevent the operation of the two module current-based resonant converter. Further investigation is required, and verification of the simulation must be performed with experimental work.

Converter Quantity	value
V_{in}	200V
\bar{V}_{out}	2kV
f_{sw}	3.5kHz
L_{in}	5mH
L_{v1}	225 μ H
L_{v2}	250 μ H
C_v	0.1 μ F

Table E.1: Components of the two module Current-Based Resonant Converter

Figure E.2: Voltage sharing between modules of Two Module Current-Based Resonant Converter with mismatch between L_v components.

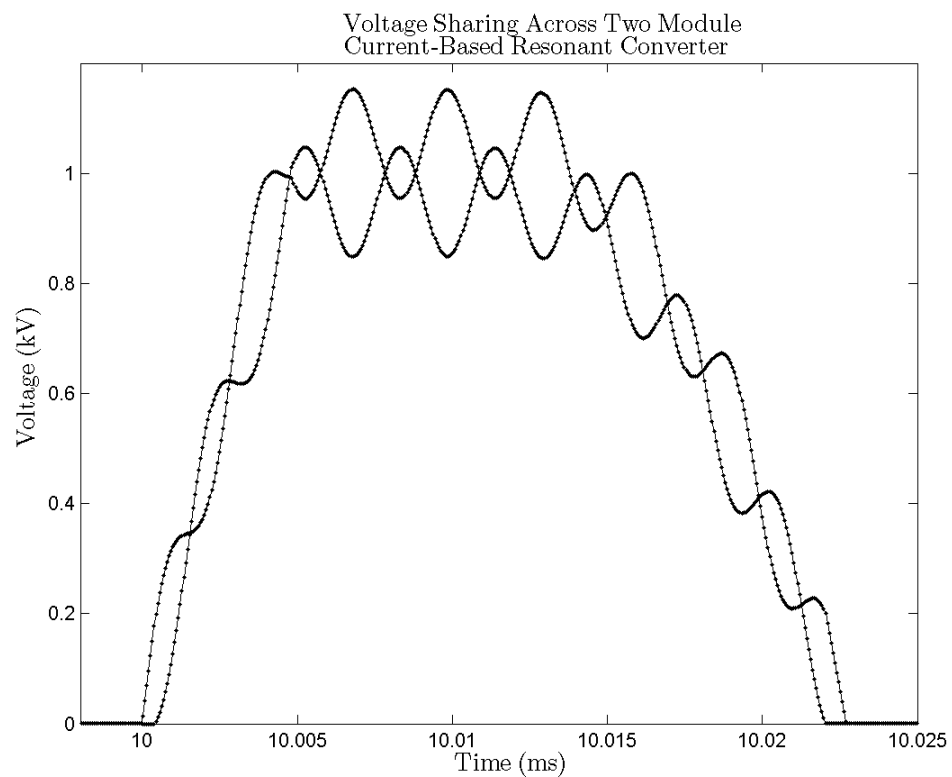


Figure E.3: Voltage sharing between modules of Two Module Current-Based Resonant Converter. The following non-idealities have been added: mismatch between L_v components, delay in gating signals, and parasitic capacitance.

Bibliography

- [1] A. Hagar, “A new family of transformerless modular dc-dc converters for high power applications,” Ph.D. dissertation, University of Toronto, 2010.
- [2] D. Jovcic, “Step-up dc-dc converter for megawatt size applications,” *Power Electronics, IET*, vol. 2, no. 6, pp. 675 –685, 2009.
- [3] J. Ciezki and R. Ashton, “Selection and stability issues associated with a navy shipboard dc zonal electric distribution system,” *Power Delivery, IEEE Transactions on*, vol. 15, no. 2, pp. 665 –669, apr 2000.
- [4] K. Mizuguchi, S. Muroyama, Y. Kuwata, and Y. Ohashi, “A new decentralized dc power system for telecommunications systems,” in *Telecommunications Energy Conference, 1990. INTELEC '90., 12th International*, oct 1990, pp. 55 –62.
- [5] C. Kim, V. Sood, G. Jang, S. Lim, and S. Lee, *HVDC transmission: power conversion applications in power systems*. John Wiley & Sons, 2009.
- [6] D. Nilsson and A. Sannino, “Efficiency analysis of low- and medium- voltage dc distribution systems,” in *Power Engineering Society General Meeting, 2004. IEEE*, june 2004, pp. 2315 –2321 Vol.2.
- [7] M. Saeedifard, M. Graovac, R. Dias, and R. Iravani, “Dc power systems: Challenges and opportunities,” in *Power and Energy Society General Meeting, 2010 IEEE*, july 2010, pp. 1 –7.

- [8] D. Jovicic and B. Ooi, "Developing dc transmission networks using dc transformers," *Power Delivery, IEEE Transactions on*, vol. 25, no. 4, pp. 2535 –2543, oct. 2010.
- [9] N. Denniston, A. Massoud, S. Ahmed, and P. Enjeti, "Multiple module high gain high voltage dc-dc transformers for offshore wind energy systems," *Industrial Electronics, IEEE Transactions on*, 2010.
- [10] D. Jovicic and B. T. Ooi, "Tapping on hvdc lines using dc transformers," *Electric Power Systems Research*, vol. 81, no. 2, pp. 561 – 569, 2011. [Online]. Available: <http://www.sciencedirect.com/science/article/pii/S0378779610002609>
- [11] W. Li, Y. Zhao, Y. Deng, and X. He, "Interleaved converter with voltage multiplier cell for high step-up and high-efficiency conversion," *Power Electronics, IEEE Transactions on*, vol. 25, no. 9, pp. 2397 –2408, 2010.
- [12] K. Tseng and T. Liang, "Novel high-efficiency step-up converter," *Electric Power Applications, IEE Proceedings -*, vol. 151, no. 2, pp. 182 – 190, Mar. 2004.
- [13] J.-M. Kwon and B.-H. Kwon, "High step-up active-clamp converter with input-current doubler and output-voltage doubler for fuel cell power systems," *Power Electronics, IEEE Transactions on*, vol. 24, no. 1, pp. 108 –115, 2009.
- [14] D. Vinnikov, J. Laugis, and I. Galkin, "Middle-frequency isolation transformer design issues for the high-voltage dc/dc converter," in *Power Electronics Specialists Conference, 2008. PESC 2008. IEEE*, 2008, pp. 1930 –1936.
- [15] J. Liu, L. Sheng, J. Shi, Z. Zhang, and X. He, "Design of high voltage, high power and high frequency transformer in lcc resonant converter," in *Applied Power Electronics Conference and Exposition, 2009. APEC 2009. Twenty-Fourth Annual IEEE*, 2009, pp. 1034 –1038.

- [16] M. Perez, C. Blanco, M. Rico, and F. Linera, "A new topology for high voltage, high frequency transformers," in *Applied Power Electronics Conference and Exposition, 1995. APEC '95. Conference Proceedings 1995., Tenth Annual*, no. 0, Mar. 1995, pp. 554 –559 vol.2.
- [17] D. M. Robert W. Erickson, *Fundamentals of Power Electronics, Second Edition*. New York : Kluwar Academic, 2004.
- [18] R. Withanage, W. Crookes, and N. Shammas, "Novel voltage balancing technique for series connection of igbts," in *Power Electronics and Applications, 2007 European Conference on*, sept. 2007, pp. 1 –10.
- [19] B. Baha and M. O. Tokhi, "Dynamic modelling and control of resonant switch mode converters," *Control Engineering Practice*, vol. 5, no. 11, pp. 1533 – 1542, 1997. [Online]. Available: <http://www.sciencedirect.com/science/article/pii/S0967066197100077>
- [20] C. Hahn, "Modeling and control design for high power resonant dc-dc converter topologies," Department of Electrical and Computer Engineering, University of Toronto and Institute of Electrical Power Systems of the University of Erlangen-Nuremberg, Tech. Rep., 2011, studienarbeit.
- [21] F. Incropera and D. DeWitt, *Fundamentals of heat and mass transfer*. John Wiley, 2007.